Characterization of a Permanent Magnet Quadrupoles Focus of Laser-accelerated Protons

Thomas Rösch

München 2022

Characterization of a Permanent Magnet Quadrupoles Focus of Laser-accelerated Protons

DISSERTATION

an der Fakultät für Physik der

Ludwig-Maximilians-Universität München

vorgelegt von

Thomas Federico Rösch

geboren in Heidelberg

München, den 11. Februar 2022

Erstgutachter: Prof. Dr. Jörg Schreiber
Zweitgutachter: Prof. Dr. Ulrich Schramm
Tag der mündlichen Prüfung: 25.04.2022

Zusammenfassung

Viele Anwendungen von laserbeschleunigten Protonen benötigen diese an einem von der Quelle entfernten Ort. Für das Laser-driven ION (LION) Experiment am Centre for Advanced Laser Applications (CALA) werden Permanentmagnet-Quadrupole verwendet, um die Protonen zu sammeln und sie auf eine Anwendungsplattform an Luft zu transportieren. Da Anwendungsexperimente mit höchstmöglicher Teilchenfluenz angestebt werden, zielt der Aufbau darauf ab, so viele Teilchen wie möglich zu sammeln und sie auf eine möglichst kleine Fläche zu fokussieren. Diese Optimierung erfordert zwei Quadrupol-Paare, von denen eines in der Nähe der Quelle positioniert ist, um eine große Anzahl von Protonen zu sammeln, und das zweite den parallelen Strahl neu fokussiert, idealerweise bis zu seiner Emittanzgrenze. Aufgrund der typischerweise großen Energiebreite von laserbeschleunigten Protonen und des energieselektiven Verhaltens der Quadrupole ergeben sich unregelmäßige Fokusformen. Endliche Positionsgenauigkeit und unbekannte Feldfehler der Elemente erschweren die theoretischen Vorhersagen zusätzlich.

Die vorliegende Arbeit stellt die Ergebnisse umfangreicher Experimente vor, die sich insbesondere auf die Optimierung des mit dem ersten Dublett erzeugten Protonenfokus konzentrierten und die Basis für einen späteren Betrieb als Quadruplett darstellen. Auf der Grundlage eines großen Datensatzes war es möglich, den Einfluss konkreter Parameter wie relative Verdrehung, Längs- und Querposition experimentell zu ermitteln und zu verstehen. Dieses Unterfangen stützte sich auf sorgfältige Verfahren zur Vorabcharakterisierung und Vorjustage. Mit einem einzelnen Quadrupoldublett wurde ein leicht elliptischer Fokus mit einer Halbwertsbreite von (0.7 ± 0.3) mm in horizontaler Richtung und (1.4 ± 0.5) mm in vertikaler Richtung für mittlere kinetische Energien zwischen 12 MeV und 22 MeV erreicht. Simulationswerkzeuge zur Vorhersage der räumlichen und energetischen Verteilung der Protonen in der Fokusebene werden entwickelt und eingesetzt, um die große Anzahl von Parametern mit potentiell entscheidendem Einfluss aufzuschlüsseln. Begleitend zu diesem Prozess wurde ein einfaches analytisches Modell entwickelt, das beschreibt, wie sich die breite Energieverteilung in der räumlichen Verteilung manifestiert. Obwohl es auf einigen starken Näherungen beruht, erweist es sich als effizient und genau für die Beschreibung der experimentell beobachteten Fluenzbreite und -gradienten entlang von 1D-Lineouts. Darüber hinaus wurden Effekte, welche die Qualität des Protonenspots beeinträchtigen, wie z. B. Streuung im Vakuumaustrittsfenster, mit Monte-Carlo-Simulationen quantitativ bewertet. Auf der Grundlage dieses wesentlich verbesserten Modells und eines großen Datensatzes konnte die Größe der virtuellen Protonenquelle für 400 nm bis 600 nm dünne

Folientargets auf $(34 \pm 18)\,\mu m$ in horizontaler und $(11 \pm 7)\,\mu m$ in vertikaler Dimension und innerhalb der Unsicherheit von der Teilchenenergie unabhängig bestimmt werden. Dieses Ergebnis steht in starkem Kontrast zu der Energieabhängigkeit, die für die Protonenbeschleunigung von Mikrometer-Targetfolien gemessen wurde.

Zusätzlich zu diesem wissenschaftlichen Ergebnis werden in dieser Arbeit Faktoren des derzeitigen Aufbaus identifiziert, die die Fluenz und die Fokusgröße begrenzen. Sie liefert daher Anhaltspunkte für die weitere Optimierung den Protonentransportaufbau an LION und ermöglicht einen verbesserten täglichen Betrieb als Grundlage für Anwendungsexperimente. Die entwickelte Methodik und das Verständnis ermöglichen nun eine gezielte Optimierung des zweiten Quadrupoldubletts, das bereits vorbereitet, charakterisiert, implementiert und für erste Tests genutzt wurde. Die Ergebnisse zeigen eine räumlich und energetisch getrennte Doppelfokusstruktur, wobei beide Spots eine Größe von ca. 0.5 mm haben, was auf die Notwendigkeit einer anschließenden Untersuchung der Quadruplettausrichtung und des Verhaltens hinweist, da kleinere Größen erwartbar sind.

Abstract

Many applications of laser-accelerated protons demand them at a remote location from the source. For the Laser-driven ION (LION) experiment at the Centre for Advanced Laser Applications permanent magnet quadrupoles are used to collect and focus them to an application platform on air. As the setup envisions application experiments with highest possible particle fluence, it aims at collecting as many particles as possible and focus them on the smallest possible area. This optimization requires two quadrupole doublets, one positioned close to the source to collect a large number of protons and the second to refocus the parallel beam, ideally to its emittance limit. Due to the typically broad energy spread in the laser-accelerated proton bunch and the energy selective behavior of the quadrupoles, irregular focus shapes arise. Finite position accuracy and unknown field errors of elements further complicate theoretical predictions.

The work at hand presents the results of extensive experiments that particularly concentrated on optimizing the proton focus produced with the first doublet and represents the base for a later operation as quadruplet. Based on a large data set it was possible to identify and understand the influence of concrete parameters such as relative rotation, longitudinal and transverse position experimentally. This endeavor relied on careful pre-characterization and pre-alignment procedures. With a single quadrupole doublet a slightly elliptical focal spot with a full-width at half maximum of (0.7 ± 0.3) mm in horizontal direction and (1.4 ± 0.5) mm in vertical direction for setup design energies between 12 MeV and 22 MeV was achieved. Simulation tools for predicting the spatial and energy distribution of the protons in the focal plane were developed and employed to disentangle the large number of parameters with potentially decisive influence. Accompanying this process, a simple analytical model was developed to describe how the broad energy distribution manifests in the spatial distribution. While it does rely on some strong approximations, it proofs efficient and accurate for describing the experimentally observed fluence extents and gradients along 1D lineouts. In addition, effects that impair the proton spot quality such as scattering in the vacuum exit window were quantitatively assessed with Monte-Carlo simulations. On the basis of this substantially improved model and a large data set, the protons virtual source size for 400 nm to 600 nm thin foil targets could be estimated to be (34 ± 18) µm in horizontal and (11 ± 7) µm in vertical dimension and, within the uncertainty, independent of the particle energy. This result is in strong contrast to the energy dependence measured for proton acceleration from micrometer thick target foils.

In addition to this scientific result, this thesis work identifies factors of the current setup that limit fluence and proton spot size. It therefore provides guidance for further optimizing the proton transport beamline at LION and facilitates improved daily operation as a basis for application experiments. The developed methodology and understanding now enables targeted optimization of the second quadrupole doublet, which has already been prepared, characterized, implemented and used in first tests. The results show a spatially and energetically separated double focus structure with both spots having a size of around 0.5 mm indicating the necessity of a subsequent investigation of the quadruplet alignment and behavior, as smaller sizes can be expected.

Contents

List of Figures xi

List of Tables xv

Abbreviations xvii

1. Introduction 1

2. Laser-Driven Ion Acceleration in Plasmas 7
- 2.1. High Intensity Lasers and Plasmas . . . 8
- 2.2. Proton Acceleration Mechanisms . . . 11
  - 2.2.1. Target Normal Sheath Acceleration . . . 11
  - 2.2.2. Radiation Pressure Acceleration . . . 16

3. Theory for Polychromatic Particle Transport 17
- 3.1. Bunch Description . . . 17
  - 3.1.1. Frenet-Serret-Coordinates . . . 18
  - 3.1.2. Statistical Bunch Description . . . 19
- 3.2. Transverse Linear Beam Dynamics . . . 22
  - 3.2.1. Equation of Motion . . . 22
  - 3.2.2. Solution of EQM and Matrix Formalism . . . 26
  - 3.2.3. Bunch Transport . . . 27
  - 3.2.4. Transverse Offsets . . . 28
  - 3.2.5. Geometric Optics . . . 30
- 3.3. Imaging with a Doublet . . . 35
- 3.4. Fluence Distribution and Spectrum in a Quadrupole Doublet Focus with a Polychromatic Ion Bunch . . . 36

4. The Laser-Ion Beamline at the Centre for Advanced Laser Applications 49
- 4.1. Permanent Magnet Quadrupoles . . . 50
- 4.2. Doublet Setup and Free Parameters . . . 51
- 4.3. Acceptance and Radiation Shielding . . . 53

4.4. Laser Light Shielding . . . 58
4.5. Detection . . . 60
4.5.1. Scintillator . . . 63
4.5.2. Radiochromic Films . . . 64
4.5.3. Image Plates . . . 64
4.5.4. Wide Angle Spectrometer . . . 65
4.6. Doublet Focus Shape Calculation . . . 65
4.7. Doublet Spectrum Calculation . . . 80

5. Experimental Results **83**
5.1. Transverse Offsets . . . 84
5.2. Rotation . . . 88
5.3. Drift Lengths . . . 89
5.4. Best Proton Focus . . . 91
5.5. Reproducibility . . . 92
5.6. Source Size Estimation . . . 93
5.7. Dose Distribution in Focus . . . 99
5.8. Transverse Steering . . . 100

6. The LION Quadruplet **105**
6.1. Imaging with a Quadruplet . . . 105
6.2. Quadruplet Setup . . . 106
6.3. Quadruplet Focus . . . 109

7. Discussion **113**

8. Conclusions and Outlook **121**

Appendices **127**

A. Analytic Solution of the Fluence Distribution with No Detuning and Minimum Spot Size **127**

Publications and Conference Contributions **131**

Bibliography **135**

Acknowledgments **147**

List of Figures

2.1. Schematic drawing of the target normal sheath acceleration (TNSA) process 13
2.2. Proton spectrum measured by Snavely et al. 13
2.3. Sketch of energy dependence of divergence angle in the TNSA process . . 14

3.1. Coordinate system in laboratory frame of reference 18
3.2. Example beam profile with Gaussian distribution 20
3.3. Sketch of an arbitrary example particle distribution projected onto (x, x') space 21
3.4. Sketch of a quadrupole field and the effect of the Lorentz force 25
3.5. Example trajectories in a quadrupole doublet calculated with the matrix formalism 28
3.6. Thin lens approximation of a quadrupole 31
3.7. Thick Lens 32
3.8. Quadrupole doublet with thin lenses 33
3.9. Example trajectories through a permanent magnet quadrupole (PMQ) doublet with different energies 36
3.10. Estimation of the $\sigma(p)$ functions 39
3.11. Example for the correction of the indefinite integral function 43
3.12. Influence of a variation of σ'_{x0} and σ'_{y0} on the focus shape 46
3.13. Focus shape for different values of δ' 46
3.14. Contribution of different spectral parts to the focus shape 47

4.1. The Halbach design PMQs of the laser-driven ion (LION) experiment in Centre for Advanced Laser Applications (CALA) 50
4.2. Drifts and lengths for the doublet setup 51
4.3. Focusing setup in the LION vacuum chamber 52
4.4. Calculated maximum acceptance angles x'_{max} and y'_{max} 53
4.5. Aluminum shielding with elliptical aperture mounted in front of PMQ 1 . 55
4.6. Calculated trajectories of 12 MeV and 22 MeV design particles through the doublet 56
4.7. Transmitted bunch divergence as a function of design energy 57

4.8. Glass cone with aluminum shielding mounted in front of PMQ 1 59
4.9. Glass shielding for laser light guidance and back reflex protection 59
4.10. Positioning system of the laser shielding 60
4.11. Scheme of the doublet focusing setup in CALA LION 61
4.12. Results from Fluka simulations of the vacuum exit window 62
4.13. Fits to the results from Fluka simulations of the vacuum exit window . . 63
4.14. Scintillator setups for proton focus imaging 64
4.15. Differential wide angle spectrometer (WASP) spectrum from Shot 5 on May 12, 2021 66
4.16. Bunch size as function of proton energy 68
4.17. Calculation of fluence profile in the focal plane for different source distributions 69
4.18. Estimation of the fluence distribution from the numerically integrated Gaussian distribution 71
4.19. V_x and V_y as function of energy for a 12 MeV design energy setup 72
4.20. Results of particle tracking through a 12 MeV and 22 MeV design energy setup 73
4.21. Comparison of the numerically integrated distribution to the analytical model 74
4.22. Bunch sizes in the focal plane compared to analytical model for different source sizes 75
4.23. Bunch sizes in the focal plane compared to fitted analytical model for different source sizes 76
4.24. Scaling factors $a_{x/y}$ obtained from fits for different source size 77
4.25. Fit of the analytical model to the numerically calculated lienouts 78
4.26. Calculated spectra in focus of different radii 81
4.27. Bragg curves reconstructed from the calculated spectra 81

5.1. Observation of Steering in x direction by intentional changes for 16 MeV design energy 84
5.2. Calculation of steering due to lateral shift 85
5.3. Example of beam profiles for different relative offsets for a 16 MeV design energy setup 87
5.4. Measured bunch profiles for different rotation angles 88
5.5. Bunch profile measurements for different offsets Δd_1 and Δd_2 90
5.6. Bunch profile measurement for 12 MeV design energy 91

5.7. Position of the peak in the fluence distribution for 45 consecutive shots . 92
5.8. Sum of images of 45 consecutive shots. 93
5.9. Source size estimation for optimized foci of different design energies . . . 94
5.10. Proton focus size for different design energy settings 96
5.11. Retrieved source size for different design energy settings 97
5.12. Source size analysis of 31 of the 45 shots used for Fig. 5.7 98
5.13. Dose distribution in the radiochromic film (RCF) stack for 18 MeV design energy and three accumulated bunches 99
5.14. Depth dose curves measured and reconstructed from the calculated spectra 100
5.15. Observation of steering as a function of design energy 101
5.16. Results from steering measurement and analysis 102

6.1. Example trajectories through a PMQ quadruplet for different energies . . 105
6.2. Scheme of the quadruplet focusing setup in CALA LION 106
6.3. Second pair of PMQs installed in the back of the LION vacuum chamber 107
6.4. Calculated bunch size as function of proton energy 108
6.5. Calculated bunch profile for the 13 MeV design energy setup 109
6.6. Images of the quadruplet focus for different design energies 110
6.7. Comparison of the focus from the doublet and the quadruplet setup . . . 112

7.1. Influence of the bunch spectrum on the resulting fluence distributions . . 114

A.1. Results of the analytic calulation of a 2D fluence distribution 128

List of Tables

4.1. Gradients of the LION doublet 51

5.1. Measurement of steering with shots from April 30, 2021 101

6.1. Gradients of the LION quadruplet 106
6.2. Measured focus sizes from the shots with the PMQ quadruplet on Fig. 6.6 111

7.1. Overview of literature values for virtual and real source diameters as function of proton energy 116

Abbreviations

BOA break-out afterburner

CALA Centre for Advanced Laser Applications

CE coulomb explosion

CPA chirped pulse amplification

CSA collisionless shock acceleration

DLA direct laser acceleration

DOFO defocusing optic focusing optic

EM electromagnetic

EMP electro magnetic pulse

FODO focusing optic defocusing optic

FWHM full-width at half-maximum

IP image plate

LION laser-driven ion

OAP off-axis parabolic

PMQ permanent magnet quadrupole

RCF radiochromic film

RF radio frequency

rms root-mean-square

RPA radiation pressure acceleration

RT relativistic transparency

TFD target-focus-distance

TNSA target normal sheath acceleration

WASP wide angle spectrometer

1. Introduction

Laser-driven particle acceleration is a promising technology that is slowly yet surely developing into an applicable tool. Continuously increasing laser peak powers, expanded the frontier of reachable maximum kinetic energies of various kinds of particles. New record kinetic energies have been shown recently for both electron and ion acceleration. Electrons of up to 8 GeV could be measured from laser wakefield acceleration [1] and the acceleration of laser-driven protons with maximum kinetic energies of above 94 MeV was demonstrated [2]. Also heavier particles like gold ions could be accelerated to energies above 5 MeV/u [3]. With this development, laser-driven particle sources are getting closer to becoming a valuable basis for both the development of next generation particle accelerators [4] and new applications that exploit the specific properties of the particle bunches that these novel sources provide [5].

The most disseminated way to realize laser-driven particle acceleration is via the interaction of high intensity lasers with plasmas. Here, it depends mainly on the plasma density whether predominately electrons or both electrons and ions are accelerated. In the case of laser-driven proton acceleration, a high intensity laser interacts with a micrometer thin solid density foil, ignites a plasma and through the interaction of the laser field and the electrons accelerates protons. This new kind of source exhibits a variety of interesting features that are distinct in the field of particle accelerators and differ strongly from the properties of conventionally accelerated bunches. Conventional particle accelerators usually deliver continuous or bunched low divergence beams with a narrow spread in particle energy. Proton bunches produced during laser-plasma interaction have typically a broad energy spectrum with 100% energy spread, a large divergence and a very short bunch duration that is on the order of the laser pulse duration of picoseconds. In the context of an accelerator, laser-ion acceleration today can be viewed merely as a source; in particular as a back-illuminated photo anode. The number of particles per bunch that this source provides is so high that the peak current exceeds the one of conventional radio frequency (RF) accelerators by far. Due to the nature of the acceleration process, alongside with the high energy protons a lot of byproducts are produced such as relativistic electrons and electromagnetic radiation ranging from radio frequencies up to the x-ray and MeV region.

These different properties pose a series of new challenges to the development from the mere acceleration process towards a reliable and stable integrated laser-driven ion accelerator system [6]. Low laser repetition rates, only slowly replaceable targets, i.e. sources and large shot-to-shot fluctuations in particle numbers and energies impose so far limitations on the usability of laser-driven proton accelerators. To overcome these limits, new approaches are required that expand on known laser and accelerator technology and that address all elements from source to application, grouped in laser, targetry, bunch transport and instrumentation. The aim of these efforts is to enable the control and transport of the source properties paving the way towards new applications that are not accessible for conventionally accelerated particles. For example, a method of bimodal imaging has been demonstrated that exploits both proton and x-ray radiation that originates simultaneously from the same laser-driven source [7]. Due to the extremely small size of the source it is possible to combine phase contrast imaging with proton radiography. This means that with only one laser pulse one can obtain information about a sample from two radiation modalities.

Typically, most applications require however controlled and reproducible proton bunches that are free of contamination from other kinds of radiation. Because of the extreme environment close to the laser plasma interaction caused by ultra-high light intensity and secondary radiation, providing these conditions close to the source is difficult. Further, given their broad energy spectrum and large divergence, the free propagation of the protons over a large distance leads to a large spread of the bunch over time and space. Hence, it is desirable to implement a bunch transport line, that maintains or recovers the source properties of the bunch at a significant distance enabling clean and controlled experiment conditions.

Transporting as well as improving or tailoring the bunch properties from the source to the desired delivery point is the basic task of every charged particle beamline and key component of any particle accelerator. Many years of accelerator research have been dedicated to the study of particle trajectories in electromagnetic fields and to the design of beamline elements satisfying the needs created by extremely high particle energies, ultimately resulting in the construction of impressive machines such as the Large Hardron Collider (LHC) [8] at the *European Organization for Nuclear Research* (CERN). In laser-driven ion acceleration research the development of dedicated beam transport systems that consider the special properties of these kind of bunches is still in the early stages [9–15]. Suitable methods ideally preserve the compactness of the accelerator and consider the source properties like the intrinsically pulsed nature of the

acceleration process or the secondary radiation.

One major property that is key for many applications is the high particle fluence that is achievable with laser-driven acceleration. Therefore, an optimization goal could be to transport as many particles as possible from the source and focus them at a remote location to a spot as small as possible. To tackle this challenge many different approaches have been pursued. Innovative efforts tried to reduce the initial bunch divergence already at the target level, for instance by using a concave target surface causing an ion focus only micrometer away from the source which was applied to isochoric heating of a secondary target [16]. Similarly sophisticated is an approach in which a millimeter long coil is attached to the rear side of the target [17, 18]. After particle acceleration the charge neutralization current returning into the plasma is guided through the coil causing a moving electric field inside of the coil that travels along with the accelerated protons. The dynamic field distribution causes both accelerating and focusing field components that lead to a proton focus at some centimeters behind the target. This promising technique, that could be staged multiple times, is a good example of a bunch guidance tailored to the properties of laser-driven acceleration.

Currently more common are methods that use dedicated, typically non-laser based transport devices downstream of the target. An intensely investigated way that regained new attention is the plasma lens. The strong electric fields that can be produced in a plasma are able to steer charged particles of very high energies. Focusing in particular can be achieved by strong radial fields in a cylindrical plasma. This can be created either by igniting a solid density cylinder by a laser [19] or by a discharge in a gas filled glass capillary [1, 20]. This technique fulfills the requirements of compactness and can be easily synchronized to the pulsed particle acceleration since the plasma lens can be driven optically, ideally by a fraction of the laser which accelerates the particles. Another pulsed approach that is well adapted to large acceptance angle are pulse power solenoids. The strong fields with 10s of Tesla allow collecting a large fraction of the highly diverging laser-accelerated bunch [21]. A strong current pulse is driven through a conducting coil creating a magnetic field inside. In this field the radial velocity components of the particles force them onto helical trajectories. When exiting the field the fringe fields cancel the azimuthal component of the helical motion leaving the radially focusing velocity component [22]. However, the solenoid focusing is only a second order effect. Therefore extremely high currents in the kilo-ampere range are required to achieve sufficiently strong focusing, which for high repetition rates raises the challenge of cooling in vacuum [23].

The workhorse for transport and focusing are quadrupole magnets, arranged after the principle of strong focusing with alternating gradients [24]. Typically implemented as warm or superconducting electromagnets they appear in any beam transport line of a linear or circular accelerator. Quadrupoles can be built from permanent magnets and are commonly used inside drift tube linear accelerators in Alvarez structures. A permanent magnet quadrupole (PMQ) can be built very compact, has a strong field gradient and does not require power supplies. This makes these kind of magnets also attractive for the use with laser-accelerated particle bunches as neither cooling nor synchronicity add challenges in operation. Over the years there were different examples where this technique has been applied to laser-driven protons [25–29]. These studies revealed a series of new challenges that are for example due to the broad energy distribution of particles. Strong focusing is usually achieved only for particles of one particular energy, which in the scope of this work will be called design energy. Only particles of this energy follow the trajectories through the magnets that belong to the optimized bunch transport geometry. Particles of different energies will be transported forming different transverse bunch profiles per energy slice. This effect causes an irregular shape to arise in the fluence distribution of a focused laser-accelerated proton bunch. As there is no possibility to tune the magnetic field like in the case of electromagnets and PMQs are fixed in length, the only parameters to adjust the beamline for a desired transport behavior are the geometric positions of the magnets along the beamline. The influence of positioning inaccuracies were subject to some previous investigations [30, 31] and need to be considered when designing a focusing setup. Further, the influence of the individual parameters need to be assessed in order to optimize the shape of the focal spot. Furthermore, as the magnetic fields of the magnets cannot be easily adapted, a precise knowledge of the fields is required, which demands also a detailed consideration of field errors [26, 28].

The laser-driven ion (LION) experiment at the Centre for Advanced Laser Applications (CALA) in Garching near Munich relies on PMQs for focusing of laser-accelerated protons. The setup of the experiment aims at providing highest possible particle fluences to an application platform at approximately 1.8 m distance to the laser-driven proton source. The particle bunches are intended to be used for experimental investigations of ion-matter interaction on (sub)- nanosecond and microscopic scales. For the highest fluence it is required to collect as many particles from the source as possible and focus them on the smallest possible area. In order to achieve this two pairs of PMQs are foreseen, one close to the source to collect the particles and a second to refocus the parallel beam.

The theoretical limit for the minimum size of a bunch of charged particles is given

by its emittance, which relates size and momentum of the bunch and will be explained later in more detail. The smaller the emittance, the more the bunch can be compressed. For an ion focusing system the minimum focus size is determined by the emittance of the injected ion bunch. In the LION setup this is determined directly by the particle source, i.e. by the area where the particles are emitted, their divergence angle and the correlation between those quantities.

The source emittance of laser-accelerated protons from micrometer thin metal foils has been subject to investigations [32–36], which came to the conclusion, that despite their large overall divergence, laser-driven proton bunches have a extremely small emittance due to the small source size and high laminarity in the bunch. In the case of the LION source with its laser and target parameters the emittance is yet unknown. Compared to previous studies [32–36] the LION experiment utilizes plastic foils with few hundred nanometer thickness and operates at a different laser wavelength (800 nm instead of 1054 nm) which are both parameters that influence the acceleration mechanism and therefore possibly source size and divergence. Established methods (like the pepper-pot method [37]) for determining the emittance are difficult to implement, because thin target foils become transparent during the laser-plasma interaction. But even if known, it would not ensure that a common setup yields the smallest proton focus, as it could be dominated by alignment and field uncertainties of the PMQs. The identification of the best focus, therefore, can only rely on experimental investigation of the available parameter space of the focusing system. Thereby, the setup configuration that minimizes the focus size corresponds to an imaging of the virtual source for the design energy protons, which is not necessarily the real source from where the protons are emitted [35, 38]. For this reason and because the magnetic transport is linear, a reproduction of the experimentally achieved best focus with numerical or analytical models can allow to retrieve the virtual source size for a energy interval around the design energy. But as the PMQs have only a limited acceptance the full divergence and therefore the real emittance of the bunch energy slice remains unknown.

This work is dedicated to investigate and optimize the focusing setup of the LION beamline. Therefore, extensive experiments were performed that concentrated on optimizing and understanding the focus of the first pair of PMQs. A significant data set was collected with the goal of identifying the influence of concrete parameters such as relative rotation, longitudinal and transverse positions experimentally. This endeavor was based on careful pre-characterization and pre-alignment procedures that will be summarized. Simulation tools for predicting the spatial and energy distribution of the protons in the

focal plane are developed and employed to disentangle the large number of parameters with decisive influence. In addition, effects that impair the proton spot quality such as scattering in the vacuum exit window were quantitatively assessed with Monte Carlo simulations. Accompanying this process, a novel analytical model was developed to describe how the broad energy distribution manifests in the spatial distribution in the image plane. The application of this model to measurement results yielded an estimation for the energy dependent source size previously not investigated for nanometer scale target foil thickness. To conclude this work a second pair of PMQs was characterized and implemented in a first test experiment.

This thesis starts with an introduction into laser-driven ion acceleration in chapter 2 which is followed by the theory of ion optics required for the understanding of the developed calculation tools. Both are explained in chapter 3. Chapter 4 will introduce the LION setup in CALA and the simulations of the expected fluence distribution. The experimental results achieved with the PMQ doublet are presented and analyzed in chapter 5, leading to estimates of achievable focus size, reproducibility and retrieved energy dependent virtual proton source size. Results from experiments with the two pairs of PMQs will be shown in chapter 6 and the work will be discussed and summarized in chapters 7 and 8.

2. Laser-Driven Ion Acceleration in Plasmas

There are several approaches to realize laser-driven ion acceleration. According to the Lawson-Woodward theorem [39–41] direct free space acceleration of charged particles is not possible with any kind of oscillating electromagnetic field if ponderomotive effects due to intensity gradients are negligible. One way to realize a net energy transfer from the field to the charged particle is by implementing boundary conditions for the fields. In conventional RF accelerators this happens in the acceleration gaps or cavities. Scaling this method down to optical frequencies is the approach pursued by direct laser acceleration (DLA) [42–44]. Laser-driven ion acceleration as described here is based on the interaction of a high intensity laser with a plasma from a thin solid density target. In a nutshell, the plasma as medium enables the energy transfer from the laser field to electrons and subsequently to ions. So, in the context of laser plasma accelerators direct energy transfer from the laser field to the ions is typically not considered. Instead electrons act as mediators that absorb laser energy and transfer this energy to the ions via a variety of different possible mechanisms (all based on electromagnetic interactions).

The proton can be accelerated most effectively due to the highest charge to mass ratio of all ions, which is why in the following we will limit the explanations to proton acceleration. The basic realization of laser-driven proton acceleration from plasmas is to irradiate a solid density target, typically a micrometer to nanometer thin metallic or plastic foil, with a very short femtosecond high energy laser pulse focused to a micrometer spot. The repetition rate of the proton production depends on the laser system. It extends from kHz with ultra-short pulse durations (40 fs, Ti:Sapphire) [45] to one pulse every 90 min for long pulse laser systems (500 fs, glass) [46]. The acceleration of other ion species like carbon or gold is also possible but typically benefits from a suppression of the energetically favored proton acceleration [3, 47, 48]. Good overviews about the topic of laser ion acceleration are given in review papers such as [49] and [50].

2.1. High Intensity Lasers and Plasmas

High intensity laser pulses are generated via chirped pulse amplification (CPA) [51]. For laser pulses we define the cycle averaged peak intensity I is defined as

$$I = \frac{W_L}{A_L \cdot \tau_L} \tag{2.1}$$

where W_L is the laser pulse energy, A_L the area of the transverse laser profile and τ_L the laser pulse duration. In CPA an initial laser pulse, e.g. coming from an oscillator, is stretched in time, then energy amplified and in the end recompressed back to a short pulse duration. To keep the intensity below the damage threshold of the laser optics during this process A_L is increased by expanding the laser profile. As a last step the laser is then focused onto a desired target to obtain the highest possible intensity. Currently, typical orders of magnitude for intensities used for particle acceleration are 10^{19} to $10^{21}\,\mathrm{W/cm^2}$, many orders of magnitude beyond the maximum ionization threshold of any material around 10^{12} to $10^{14}\,\mathrm{W/cm^2}$. Hence, on the target, the initial intensity rise is already sufficient to ionize the target atoms and ignite a plasma which the rest of the pulse interacts with. Ionization happens first via *multiphoton ionization* [52] and *tunneling ionization* [53,54] and later with highest intensities via *barrier-suppression ionization* [55].

For pulsed lasers an important measure for the temporal evolution of the intensity is the temporal laser contrast. It is defined as the intensity ratio between the peak intensity and an intensity level at a determined time before the peak. Typical reference times to indicate a laser contrast are either few nanoseconds before the peak, which determines the intensity rise with respect to the pedestal caused for example by amplified spontaneous emission, or some picoseconds before the peak, as this time scale is important for the laser acceleration dynamics in the plasma. Frequently achieved picosecond laser contrasts for high power lasers range between 10^{-6} and 10^{-10}.

According to Chen [56] we define plasma as:

> *A plasma is a quasineutral gas of charged and neutral particles which exhibits collective behavior.*

The meaning of "collective behavior" refers to particle motions in the plasma. Due to the long range of the Coulomb force, these motions are influenced not only by local conditions but also by plasma conditions at larger distances. If these long-ranged electromagnetic forces are much larger than the forces due to local collisions between particles, the plasma is called "collisionless". A characteristic quantity to describe the collective effect

of external electric fields in the plasma is the plasma frequency ω_{pl} that describes the oscillation frequency of plasma electrons that follow the external field. It is given by

$$\omega_{pl} = \sqrt{\frac{n_e e^2}{m_e \varepsilon_0}} \tag{2.2}$$

where n_e is the electron density in the plasma, e and m_e are electron charge and mass respectively and ε_0 is the vacuum permittivity [56]. The term "quasineutrality" in the definition of a plasma comes from the balance between positive and negative charge densities in the plasma. A plasma has the ability to shield electric potentials that are introduced from outside, which is called Debye shielding. If for example a positive electric potential is applied to the plasma, negative charges would arrange in a cloud around it in such way that at a certain distance the positive potential is completely shielded. This distance will depend on the kinetic energy of electrons T as it determines the distance to the potential maximum where electrons can escape the potential. So, if a potential is on the order of T/e, it can leak into the plasma and finite electric fields can exist. In this case the shielding is not complete. A measure for this shielding distance is the so-called Debye radius [56]

$$r_D = \sqrt{\frac{\varepsilon_0 T}{e^2 n_e}}. \tag{2.3}$$

Assume a plasma of dimension $L >> r_D$ where the Debye shielding happens at a distance much smaller than L such that the bulk of the plasma can be considered free of large electric potentials or fields. Then a plasma can be called "quasineutral" since one can assume the density of ions n_i and electrons n_e is approximately the same. This common density n is called the plasma density. It has a fundamental meaning for the interaction of the plasma with electromagnetic fields such as the laser, since it determines the refractive index of the plasma. Therefore, whether the plasma is reflective or transmissive for the laser depends on both the plasma density and the wavelength of the laser. The nonlinear, relativistic refractive index n is given as [57, 58]

$$\mathrm{n} = \sqrt{1 - \frac{n_e}{\gamma n_c}} = \sqrt{1 - \frac{\omega_{pl}^2}{\gamma \omega^2}} \tag{2.4}$$

with

$$n_c = \frac{m_e \varepsilon_0 \omega^2}{e^2} \tag{2.5}$$

and the Lorentz factor

$$\gamma = \frac{1}{\sqrt{1-\beta^2}} \tag{2.6}$$

where $\beta = v/c$ with v being the average electron velocity. n_c is the so called non-relativistic critical density. It depends on the laser frequency and the refractive index can be given as function of plasma frequency and laser frequency ω. c is the vacuum speed of light and ε_0 the vacuum permittivity. For ion acceleration the laser interacts with plasmas from solid targets where in the bulk the electron density exceeds the n_c by orders of magnitude. In this case of an "over-dense" plasma the refractive index is imaginary and the plasma is reflective for the laser light. However, usually at the surface the plasma starts to expand immediately reducing the electron density on the surface layers. If $n_e < \gamma n_c$ the plasma becomes transparent. This allows the laser to penetrate into this less dense areas and interact with the plasma.

The electric and magnetic fields of the laser interact mainly with the plasma electrons, since they are lighter than the ions. The process of transfer of laser energy to the plasma electrons is called electron heating. There have been identified several heating models to explain the energy transfer, such as resonance absorption [58], vacuum or "Brunel" heating [59] and "$\mathbf{J} \times \mathbf{B}$" heating [60]. Which mechanism dominates the energy transfer process depends on many parameters as for example laser incidence angle and polarization and contrast. The exact energy transfer mechanisms are not relevant for this work and hence will not be treated further. Typically, electrons are referred to as "hot" if they are relativistic, i.e. they have a kinetic energy greater than their rest mass energy 511 keV. In this case their total energy is given by

$$W = \gamma m_e c^2. \tag{2.7}$$

It is difficult to describe exactly the hot electron energy and density distribution given that heating is a stochastic process. Typically, it is assumed that the hot electron density follows a Boltzman distribution with a mean kinetic energy T [61]. Simulations suggest it to be on the order of the cycle-averaged oscillation energy in the electric field of the laser in vacuum coming from the so called ponderomotive scaling of the absorption $\gamma = \sqrt{1 + \frac{a_0^2}{2}}$ [62]

$$\begin{aligned} T &= W - m_e c^2 \\ &= m_e c^2(\gamma - 1) \\ &= m_e c^2(\sqrt{1 + a_0^2/2} - 1). \end{aligned} \tag{2.8}$$

In general the complete hot electron energy distribution can be assumed to be exponentially decaying [63]. The normalized vector potential amplitude a_0 is calculated from the vector potential amplitude A by $a_0 = \frac{eA}{m_e c^2}$. It relates to the laser intensity (given in W/cm^2) and wavelength λ (given in µm) via

$$a_0 = 0.85\sqrt{\frac{I\lambda^2}{10^{18}\mathrm{W\,cm^{-2}\,\mu m^2}}}. \tag{2.9}$$

2.2. Proton Acceleration Mechanisms

As mentioned above the effective acceleration mechanism for protons is due to the energy transfer from hot electrons. As the coupling of the laser to the plasma electrons depends on the penetration depth, the process is a complex interlink between laser contrast, intensity and duration as well as target thickness and density. Common to all parameter regimes is that a current of hot electrons is generated that creates the acceleration field for the protons. In a wider sense this can be seen as rectification of the oscillating electric field of the laser. The dynamics of the electron current and the accelerating field though can vary strongly.

Many different schemes in very different laser and target parameter regimes have been proposed and demonstrated to describe the acceleration. Most commonly known are target normal sheath acceleration (TNSA) [64,65], radiation pressure acceleration (RPA) [66,67], break-out afterburner (BOA) [68], collisionless shock acceleration (CSA) [69], coulomb explosion (CE) [70] and magnetic vortex acceleration [71, 72]. This section will focus on the basic laser plasma interaction and only describe the schemes of relevance for understanding of this work and its results.

2.2.1. Target Normal Sheath Acceleration

The best understood and consequently most commonly used mechanism to model the acceleration of protons by lasers is target normal sheath acceleration (TNSA). It was introduced by Wilks et al. [64] to explain the experimental results obtained by Snavely et al. [73] and others (e.g. [65]). They had observed mutli-MeV particles emerging from the rear side of about 100 µm thick foil targets. This mechanism is suited to explain the easiest accessible laser and target parameter space for laser-driven ion acceleration as it requires the lowest laser intensities and rather thick targets. When the increasing laser intensity ionizes the foil at the front side it produces a solid density plasma with a steep

density gradient. Immediately the front surface pre-plasma starts expanding and the density at its front reduces. When the laser pulse reaches its peak intensity, the laser fields can penetrate this low density region up to the critical density front. The laser penetrates enough into the plasma to heat electrons to an energy sufficiently high to overcome the potential wall that builds up around the critical density. Those electrons then propagate through the target and exit at the rear (non-laser irradiated) side. As the laser is reflected at the critical density surface it does not penetrate the bulk of the target which stays intact until it is subsequently ionized through collisions of heated electrons. The leaving electrons induce a positive charge at the target rear surface causing the build up of a charge separation field and a confining potential. This means that the electrons will propagate in vacuum only until a certain distance before being retracted back into the plasma, forming a negatively charged sheath behind the target (see Fig. 2.1). Only the highest energetic electrons are able to overcome this potential and escape into vacuum. As long as the laser field is present in the plasma, hot electrons are continuously driven out of the plasma and pulled back into it. During this equilibrium state an electron sheath is formed at the target rear side, giving this acceleration mechanism its name. The thickness of the sheath is on the order of the Debye length of hot electrons (Eq. 2.3) and depends on their energy and hence on laser and target properties [63]. Due to this equilibrium the electric field that builds up between the sheath and the target back side can be regarded in first approximation as quasi-static for the duration of the laser pulse. It is not only strong enough to hold back the sheath electrons but also ionizes the atoms at the rear surface, which contain a large fraction of hydrogen due to water contamination layers [47, 74]. The field is on the order of TV/m [49, 50] and acts on the protons on the target rear side accelerating them in target normal direction. Together with the micrometer extend of the sheath [49] this leads to typical maximum proton energies in the MeV range. Heavier ions with higher charge to mass ratio have higher inertia and provide the positive charge to maintain the space-charge field with the sheath electrons. Evidence for the acceleration happening at the target rear side was found by Mackinnon et al. [75] and others [32, 47, 76].

As in reality the TNSA process is more complex and dynamic than an electrostatic acceleration, the bunch of accelerated protons is not monoenergetic but exhibits an exponential energy spectrum with a sharp cutoff at the maximum proton energy. A spectrum measured by Snavly et al. [73] can be seen in Fig. 2.2. It can be approximated by a quasi-thermal distribution adding the cutoff. There is still no suiting analytical model that explains the formation of the spectrum, but models for the maximum energy and

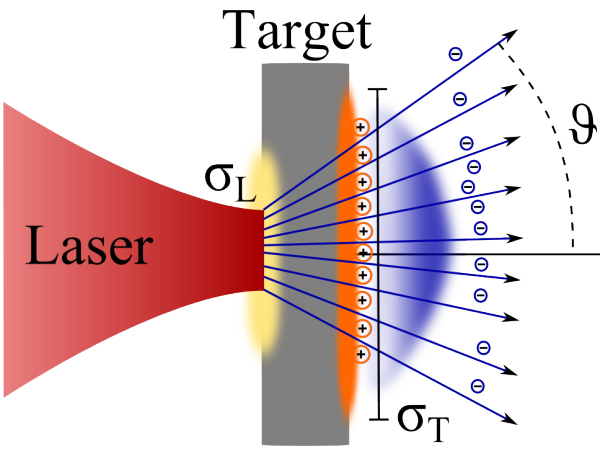

Figure 2.1.: Schematic drawing of the TNSA process. Electrons (blue) are heated on the target front side plasma (yellow), transverse the target bulk and form a sheath on the target rear side. Protons (orange) are accelerated by the field formed between sheath electrons and ionized atoms on the target back side. The proton source size σ_T exceeds the laser focus diameter σ_L due to broadening of the hot electron bunch. ϑ represents the divergence angle of the accelerated bunch.

the energy conversion efficiency have been deduced from a fluid model by Mora [61] and experimentally verified by Fuchs et al. [77]. They found the maximum energy to depend on target thickness (see also [78]), intensity and laser pulse duration. Also Schreiber et al. [63] modeled the connection between maximum energy and pulse duration based on a simple ansatz of a charged target back side and showed that there is an optimal laser pulse duration to maximize the cutoff energy. Combining these studies one can conclude that maximum cutoff energies will be achieved for that target thickness where

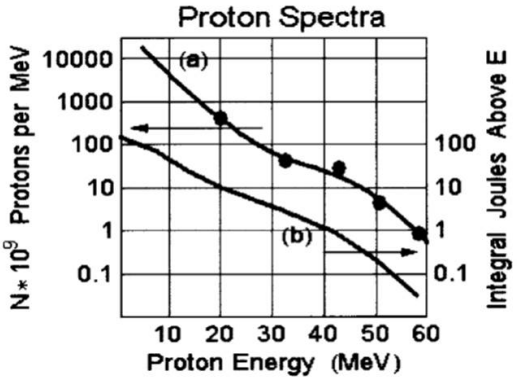

Figure 2.2.: Proton spectrum measured by Snavely et al. in 2000. Reprinted with permission from [73]. Copyright 2000 by the American Physical Society.

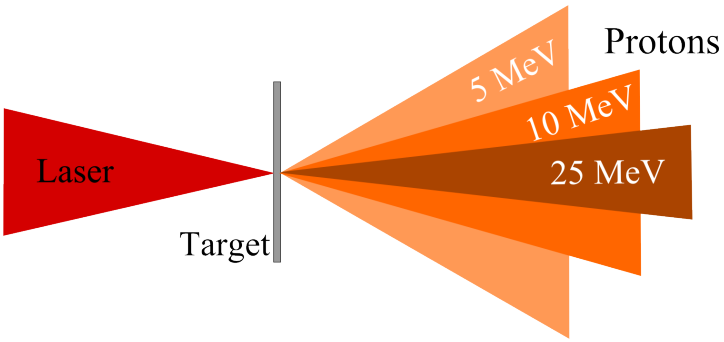

Figure 2.3.: Sketch of energy dependence of divergence angle in the TNSA process.

both the divergence of hot electrons through the plasma and the plasma pre-expansion are minimized. Therefore, an important parameter to tune the cutoff energy is the laser contrast. There have been numerous experimental investigations of the relation between target thickness and proton cutoff energies for different laser parameters with some showing, that with sharp contrast of 10^{10} no optimum target thickness is found even down to extremely thin targets $< 10\,\mathrm{nm}$, which indicates transitions to other acceleration regimes [79].

A consequence of the broad spectrum is the longitudinal energy sorting happening in a bunch upon free propagation. As the protons are typically non-relativistic, higher energy, i.e. faster protons lead in front and slower ones follow behind. This introduces an intrinsic energy chirp on the bunch and causes the bunch duration, which is initially only picoseconds to increase to nanoseconds over meters of propagation. An attempt to narrow the broad spectrum to a more monoenergetic one by using microstructured targets was made by Schwoerer et al. [80]. Unfortunately, the particle yield within the reduced energy band remained small.

Another property of the TNSA regime is that protons have large energy-dependent divergence angles as artistically illustrated in Fig. 2.3. Lower energetic protons exhibit larger divergence angles than higher energetic ones. It is believed that this results from the bell shaped form of the electron sheath at the target rear side [81]. The half opening angle ϑ of the bunch is for flat foil targets usually around 15° [32] but can be smaller for very thin foils [82] or larger for other kind of solid density targets, e.g. spheres [83]. For foils it can be influenced by adapting the rear surface shape to the wanted emission direction [19, 32] or by using additional laser pulses that cause transcendent changes of the rear surface of the target [84].

An important feature of a laser-accelerated ion bunch is its small source size. As the laser focus is the driver for the acceleration process, its transverse dimension gives

the lower limit for the ion source size. However, in the transport process through the target, the hot electron beam is scattered and broadened such that the sheath field on the target rear side has a larger transverse extent than the laser focus [63]. There are various examples of measurements of the proton source size for the TNSA process [32, 33, 35, 38, 85–88], which show that the source size decreases with increasing proton energy and varies between 500 µm for 6.2 MeV and 24 µm for 13.5 MeV.

In summary proton energy, source size and divergence are correlated in TNSA such that the lowest energy particles have the largest source size and divergence. Therefore, laser-accelerated proton bunches exhibit a very low transverse emittance, which is the quantity that measures this correlation and will be derived more rigorously when treating transverse bunch dynamics. High quality ion beams exhibit a low transverse emittance and are called highly laminar beams. Given the short duration of the process and the small source size the TNSA process produces bunches of extremely low emittance. Values for proton bunches of less than $0.1\,\pi$ mm mrad have been measured [34, 38] and values up to 0.004 mm mrad are estimated [32]. This would be 100-fold smaller than thermal proton sources that feed conventional RF accelerators. This low transverse emittance, i.e. high laminarity, can in principle enable tight focusing of particle bunches in space.

As mentioned above, regarding required laser and target parameters TNSA is the easiest accessible acceleration regime. Relatively thick, very simple foil targets from 100s of nanometer to several micrometer and comparatively low laser intensities above $10^{18}\,\mathrm{W/cm^2}$ suffice to accelerate protons to some MeV. However, by choosing a specific combination of target thickness, laser pulse duration and intensity, higher maximum energies by different acceleration mechanisms can be achieved. The key for the transition to other ways of acceleration is the interplay between the plasma density and laser intensity and contrast. The expansion of the plasma can lead to reduced electron density n_e and lead to transparency of the plasma. But also the increase of electron mass due to relativistic effects when they reach near-light speed can cause the refraction index Eq. 2.4 to become real and the plasma transparent. This effect, called self-induced transparency or relativistic transparency (RT) [49], has been observed with ultrafast temporal resolution [89] and it can lead to increased electron heating and stronger accelerating fields. For this mechanism the name break-out afterburner (BOA) was proposed by Yin et al [68].

2.2.2. Radiation Pressure Acceleration

In contrast to TNSA, RPA is an acceleration mechanism that happens at the front surface of the plasma. The interest in an acceleration mechanism using the momentum of electromagnetic (EM) waves to accelerate particles arose with simulations of thin-foil accelerations by Esirkepov et al. [66]. RPA happens in two steps. First, during the so called hole boring regime the light pressure pushes the surface of the over-dense plasma inwards. The radiation pressure acts mostly on the electrons and creates a charge separation field that drags the positive ions behind. If the target is thin enough a complete hole boring can occur and the whole plasma bulk is accelerated. This is where the light sail regime starts. It is only possible with very thin (nm) targets. In the light sail regime ions are not screened by the plasma anymore because the electrons are pushed to form a thin layer of low mass behind the ions. The radiation pressure is able to boost and further accelerate them and the ions are dragged along. So, the bunch spectrum becomes quasi-monoenergetic and further collimated in normal direction and the transverse bunch size similar to the laser focus size. However, in order to be able to follow the electrons, protons have to become relativistic very quickly. Hence, a requirement for this mechanism to become dominant is that the ions must ideally become relativistic within one laser cycle which requires an intensity above $10^{23}\,\mathrm{W/cm^2}$ [66]. The constraint on the intensity can be lowered by using circular polarized light which suppresses energy dissipation into unwanted electron heating [90]. Also, since this process happens at the front surface of the plasma it is necessary that the plasma surface is still dense and experiences little pre-expansion. Therefore, a very fast and clean intensity increase is required, i.e. a high laser contrast, that is a challenge for many laser systems. One effect that limits RPA is relativistic transparency as the laser then penetrates the plasma and the effect of the light pressure ceases.

Compared to TNSA, RPA is a more efficient process. One experimental demonstration of the feasibility of RPA was presented by Henig et al. in 2009 [67]. However, the high intensity remains a challenge for ongoing laser developments. TNSA and light sail RPA represent two extremes of the overlapping target and laser parameter regimes in which laser-driven proton acceleration takes place. They show how the interplay between target thickness, plasma density profile and laser contrast and intensity are crucial to determine the actual dynamics of the laser plasma interaction. Because of this complexity, especially for targets thicknesses $< 1\,\mu\mathrm{m}$ it is not always possible to discriminate sharply between acceleration processes, since they may happen successively or simultaneously [79, 91].

3. Theory for Polychromatic Particle Transport

Bunches of laser-accelerated protons exhibit a series of interesting properties and many applications require transport of these properties to a remote location. As free bunch propagation will decrease the fluence and increase the bunch duration, a transport system is required that manipulates the trajectory of the bunch particles. A comprehensive description of particle beam dynamics can be found in a series of particle accelerator physics textbooks [92–94]. Here, only the most important steps for understanding the mathematical formalism will be given. We will start by describing the dynamics of individual particles and extent the formalism then to sets of particles, i.e. bunches.

3.1. Bunch Description

In a very general way a particle moving in space can be described by its position (center of mass) and momentum in a 6 dimensional phase space

$$\vec{r} = \begin{pmatrix} x \\ p_x \\ y \\ p_y \\ z \\ p_z \end{pmatrix}.$$

x, y and z indicate the positions and p_x, p_y and p_z the respective momentum components. For a high energy particle typically the velocity in one dimension is much larger than in the two others. Without loss of generality we will assume from now on that this component is in the beginning along the z direction. The trajectory in space of such a particle can be influenced by magnetic and electric fields produced by elements that form a particle guiding structure. The ideal particle trajectory through this sequence of elements is called the particle orbit and it can have any desired form, for example a ring

in synchrotron accelerators, a spiral in cyclotrons or a straight line in linear accelerators. Since this orbit is fixed in space and time it makes sense to describe any particle traveling in the guiding structure with respect to a particle traveling on the ideal orbit with the ideal velocity, the so called synchronous particle.

3.1.1. Frenet-Serret-Coordinates

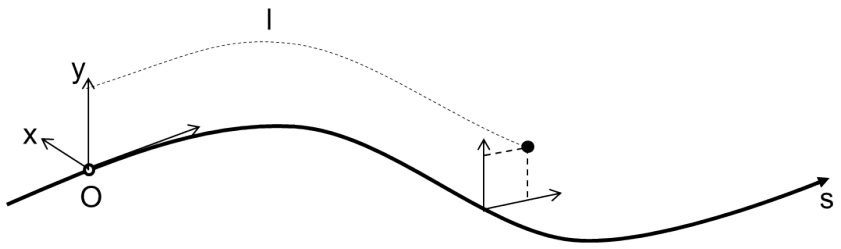

Figure 3.1.: Coordinate system in laboratory frame of reference

Describing a particle with respect to the synchronous particle equals the change of the coordinate system from laboratory frame to a co-propagating curvilinear coordinate system. This kind of coordinate system is justified by the fact that the transverse particle beam dimension is usually very small compared to the guiding structure dimension causing the deviations from the orbit to be very small in this coordinate system. The position s of the synchronous particle on the orbit defines the origin of the new coordinate system and replaces the z coordinate. It moves with the velocity of the synchronous particle along the orbit. The transverse position of a particle with respect to the orbit is described by the normal plane (x, y). The third axis s indicating the direction is defined to being tangential to the orbit. The x axis typically lies in the magnetic mid-plane whereas the y axis is normal to the magnetic mid-plane and s. For a particle with the design velocity, i.e. the velocity of the synchronous particle, the overall position is given by its position s along the orbit and the transverse position deviations $x(s)$ and $y(s)$. To describe the direction of motion of the particle instead of the momentum this coordinate system uses the deviation of direction or divergence of the particle with respect to the orbit

$$x'(s) = \frac{\mathrm{d}x}{\mathrm{d}s},\ y'(s) = \frac{\mathrm{d}y}{\mathrm{d}s}. \tag{3.1}$$

If additionally a particle has a different velocity than the synchronous particle, also a relative description in longitudinal direction is required. We use the longitudinal deviation in space l and the relative momentum deviation δ

$$l = -v_0(t - t_0),\ \delta = \frac{p - p_0}{p_0} \tag{3.2}$$

with v_0, p_0 being velocity and momentum of the synchronous particle and $t - t_0$ the differences between times when the particle and the synchronous particle are at position s. l is positive if the particle arrives earlier than the synchronous particle and negative if it arrives later. It is important to notice that even though the coordinate system (x, y, s) is co-propagating for the indication of the coordinates (l, δ) the synchronous particle is regarded as fix in space. This means that l and δ are also relative to the synchronous particle.

The coordinates relative to a ideal synchronous particle can be summarized in a 6D vector

$$\vec{r}(s) = \begin{pmatrix} x \\ x' \\ y \\ y' \\ l \\ \delta \end{pmatrix} = \begin{pmatrix} \text{radial position deviation} \\ \text{radial directional deviation} \\ \text{axial position deviation} \\ \text{axial directional deviation} \\ \text{longitudinal position deviation} \\ \text{relative momentum deviation} \end{pmatrix}. \tag{3.3}$$

The space of these vectors is called the trace space, in contrast to the phase space where position and momentum are used to describe the particle.

3.1.2. Statistical Bunch Description

A beam or bunch of particles consists of a large set of individual particles. For the cases treated in this thesis any kind of collective or space charge effects are neglected. Therefore, the bunch can be described as statistical set of independent particles in phase space or trace space that can have any arbitrary distribution $\rho\,(x, x', y, y', l, \delta)$. From a statistical point of view the size and divergence of a bunch then can be measured by the variance (root-mean-square (rms) spread) σ of this phase/trace space projections on the

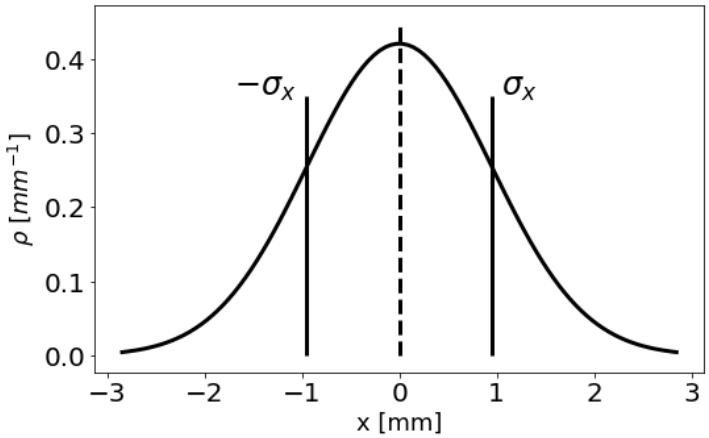

Figure 3.2.: Example beam profile with Gaussian distribution. The normalized particle density ρ as function of space x. A characteristic measure for the beam size is the variance σ_x which is 0.9 in this case.

respective coordinates (Fig. 3.2), for example for the (x, x') subspace

$$\sigma_x^2 = \left\langle x^2 \right\rangle = \int_{-\infty}^{\infty} \int_{-\infty}^{\infty} x^2 \rho_x \left(x, x'\right) dx\, dx', \tag{3.4}$$

$$\sigma_{x'}^2 = \left\langle x'^2 \right\rangle = \int_{-\infty}^{\infty} \int_{-\infty}^{\infty} x'^2 \rho_x \left(x, x'\right) dx\, dx', \tag{3.5}$$

$$\sigma_{xx'} = \left\langle xx' \right\rangle = \int_{-\infty}^{\infty} \int_{-\infty}^{\infty} xx' \rho_x \left(x, x'\right) dx\, dx'. \tag{3.6}$$

In the following we will use these variances $\sigma_{x/y/l}$ and $\sigma_{x'/y'/\delta}$ as measures for the bunch size and the divergence respectively. $\sigma_{xx'/yy'/l\delta}$ represents the correlation between divergence and position. We will here representatively treat the transverse x dimension, but the arguments can be extended to all coordinates.

Every particle density distribution ρ can usually be enclosed by an ellipse with the extent of the variances, which is called the phase ellipse (Fig. 3.3). It can be represented by the symmetric matrix

$$\sigma = \begin{pmatrix} \sigma_x^2 & \sigma_{xx'} \\ \sigma_{xx'} & \sigma_{x'}^2 \end{pmatrix} = \begin{pmatrix} \langle x^2 \rangle & \langle xx' \rangle \\ \langle xx' \rangle & \langle x'^2 \rangle \end{pmatrix} \tag{3.7}$$

and the corresponding ellipse equation

$$\left(x, x'\right) \cdot \sigma^{-1} \cdot \begin{pmatrix} x \\ x' \end{pmatrix} = 1 \tag{3.8}$$

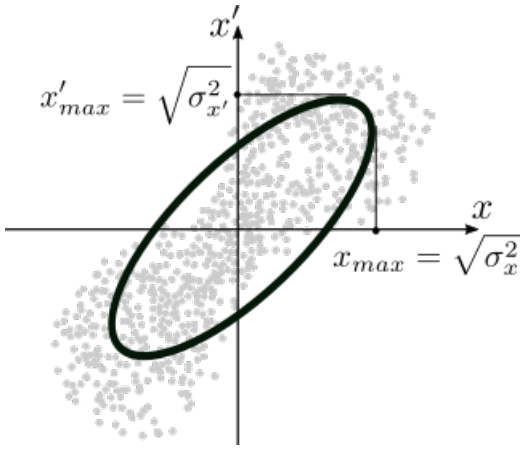

Figure 3.3.: Sketch of an arbitrary example particle distribution projected onto (x, x') space (gray) with the enclosing ellipse and the variances.

with the inverse matrix

$$\sigma^{-1} = \frac{1}{\det(\sigma)} \begin{pmatrix} \sigma^2_{x'} & -\sigma_{xx'} \\ -\sigma_{xx'} & \sigma^2_x \end{pmatrix} . \tag{3.9}$$

Resolving Eq. 3.8 yields

$$\sigma^2_{x'} x^2 - 2\sigma_{xx'} x x' + \sigma^2_x x'^2 = \det(\sigma) = \varepsilon^2_x \ . \tag{3.10}$$

ε_x is called *transverse emittance* and it is given by

$$\varepsilon_x = \det(\sigma) = \sqrt{\sigma^2_x \sigma^2_{x'} - \sigma^2_{xx'}} \ . \tag{3.11}$$

It has the unit of 1 mm·mrad and relates to the trace space area enclosed by the phase ellipse A via

$$A = \pi \varepsilon_x \ . \tag{3.12}$$

The beam or bunch matrix σ is a compact representation of the bunch envelop and suited to describe not individual particles but the behavior of the complete ensemble in the bunch. It is also possible to formulate the bunch matrix by means of the so called *Twiss parameters* but the resulting formalism is similar and will not be explained here, since it is not of relevance for this work. Interested readers may refer to standard particle accelerator physics textbooks [92, 94]. The emittance defined by the σ-matrix via Eq. 3.11 has a fundamental meaning in accelerator physics since it represents the correlation of bunch divergence and size. It is a measure for the bunch quality in terms of

focusability and laminarity because according to Liouville's theorem [94] it is a conserved quantity for linear transformations of the bunch phase or trace space. This means that any manipulation of the bunch that conserves particle numbers must conserve emittance and the associated trace space area. Therefore they represent a limit for a possible minimum spot size. The conservation of trace space is basis for calculations of the bunch transport through magnetic fields.

3.2. Transverse Linear Beam Dynamics

The trace space was introduced to describe the dynamics in a bunch of particles in a meaningful way. As only charged particles are treated here these dynamics can be best influenced by external electromagnetic forces. To understand how they act on the bunch it is useful to first calculate the action on an individual particle and extend this later to the bunch. An important measure of a bunch is the fluence $F(x, y) = \mathrm{dN}(x, y)/\mathrm{dA}$, i.e. the number of particles per area. This quantity is the time integrated particle flux. For an efficient transport of particle fluence, the active manipulation of the transverse trace space is important. To achieve highest or stable fluence the particle divergence can be tuned, reducing the bunch cross section and increasing the number of particles per area. For this reason, in the scope of this thesis, only the transverse beam dynamics are relevant and will be treated. However, it will be assumed that the longitudinal momentum p_z is always much larger than p_x and p_y, i.e. that is the particles are beam-like.

3.2.1. Equation of Motion

To calculate the effect of electromagnetic forces on charged particles it is necessary to solve the equation of motion. A particle of charge q, mass m and velocity $\vec{v}$ in an electromagnetic field ($\vec{E}$ and $\vec{B}$) experiences the Lorentz force

$$\vec{F}_L = q\left(\vec{E} + \vec{v} \times \vec{B}\right) = \dot{\vec{p}} \tag{3.13}$$

with $\vec{p} = \gamma m \vec{v}$. One can see that the effect of magnetic fields depends on the particles velocity, i.e. for swift particles magnetic fields have stronger influence than electric field components. Furthermore, in technical practice it is easier to produce large magnetic fields on the order of one Tesla. For relativistic particles the equivalent effect would be caused by electric fields of $\approx 3 \cdot 10^8\,\mathrm{V/m}$ which are far more challenging to generate. Thus, magnetic fields are the first choice when it comes to bending particle trajectories.

There are specific applications where electric fields are also used for transverse trace space manipulation. Examples are certain injection or extraction devices for circular accelerators or for non-relativistic ions. However, they are irrelevant for basic ion transport. Therefore, only magnetic component of the Lorentz force remains in the equation of motion. It reduces to

$$\frac{d\vec{p}}{dt} = q\left(\vec{v} \times \vec{B}\right). \tag{3.14}$$

As mentioned above this equation is made time independent by using the trace space coordinates $(x(s), y(s), s)$ and it is assumed that $p_z \gg p_x,\ p_y$. This assumption means that $x' = \frac{\mathrm{dx}}{\mathrm{ds}} = \frac{p_x}{p_z}$ is small and that the bunch has a small divergence with respect to the orbit. The same argument holds for the y dimension. It allows to make a linear (first-order) approximation of the magnetic field neglecting quadratic and higher order components.

Now, we consider the case of a field with only transverse components of the kind $\vec{B} = (B_x, B_y, 0)$ with a particle moving only in s-direction $\vec{v} = (0, 0, v_s)$. In this case in the horizontal plane the Lorentz force $F_{L,x} = -ev_sB_y$ and centrifugal force $F_f = \gamma m v_s^2/R$ are in equilibrium and

$$\frac{1}{R(x,y,s)} = \frac{q}{p}B_y(x,y,s) \tag{3.15}$$

with $R(x,y,s)$ being the spatially dependent radius of curvature of the deflection. Again, an analogous expression can be found for the vertical plane. A Taylor expansion of the magnetic field in Eq. 3.15 yields the contribution of the different magnetic field components to the trajectories.

$$\begin{aligned}
\frac{q}{p}B_y(x) &= \frac{q}{p}B_{y0} + \frac{q}{p}\frac{dB_y}{dx}x + \frac{q}{p}\frac{1}{2!}\frac{d^2B_y}{dx^2}x^2 + \dots \\
&= \frac{1}{R} + kx + \frac{1}{2!}mx^2 + \dots \\
&= \text{dipole} + \text{quadrupole} + \text{sextupole} + \dots
\end{aligned} \tag{3.16}$$

As we consider only linear dynamics, terms of order x^2 and higher are neglected, and only the dipole and quadrupole components are kept. Calculations including second-order terms of the Taylor expansion can describe chromatic effects and the interested reader can find them in the literature mentioned at the beginning of the chapter.

The first term of Eq. 3.16 represents the dipole component of the field. It is a

homogenous constant contribution that causes a constant steering of the trajectory. The second magnetic moment is the quadrupole component. It can be imagined as the combination of two opposing north poles and two opposing south poles with an angle of 90° with respect to each other. It has a radially increasing B-field gradient and is characterized by the quadrupole strength

$$k_x = \frac{q}{p}\frac{dB_y}{dx} \ . \tag{3.17}$$

If one analogously includes the orthogonal dimension with $k_y = \frac{q}{p}\frac{dB_x}{dy}$ from Fig. 3.4 it becomes evident that the action of the Lorentz force in a quadrupole field is such that it creates two distinct planes in which deflection is caused in opposite directions. In one plane particles are bend towards the central axis and in the other plane they are deflected away from the axis. Due to the axially and radially increasing gradients these planes have respectively a focusing and a defocusing effect on extended particle bunches. According to a common convention the sign of quadrupole strength k is chosen such, that $k < 0$ for a *focusing* effect and $k > 0$ for a *defocusing* effect. The case $k = 0$ represents an area without field, i.e. a free drift space. Duo to this simultaneous focusing and defocusing of the quadrupole field, it is necessary to use a minimum of two quadrupoles to achieve net focusing or defocusing in both planes. For example for a combination of two quadrupoles, their focusing planes need to be rotated against each other by 90°. As this gives in one plane a combination of focusing optic (FO) and defocusing optic (DO) this double quadrupole structure is called either doublet or a focusing optic defocusing optic (FODO)-structure. It is also possible to construct sequences of three (triplet), four (quadruplet) or more quadrupoles to achieve net focusing.

The assumption of small angles and the limitation to linear terms in B are only two of the approximations made to transform the equation of motion Eq. 3.14 to a time independent set of linear equations. The complete derivation is lengthy and will be skipped for the sake of simplicity. The approximations that are made in the process include (for completeness of the list the above mentioned approximations are repeated):

- The applied **magnetic field has only transverse components** $\vec{B} = (B_x, B_y, 0)$. This means that the equation of motions decouple for the x and y dimension and can be treated independently.
- The **transverse beam dimensions are small** compared to the transverse dimension of the quadrupole. In other words, the magnetic field is well represented by the truncated taylor expansion up to the quadrupole term.

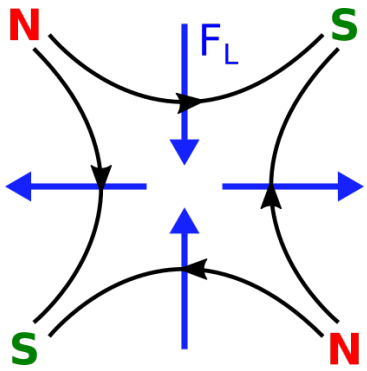

Figure 3.4.: Sketch of a quadrupole field and the effect of the Lorentz force F_L. The direction of the field lines (black) cause a focusing effect in the y plane and a defocusing effect in the x plane (blue arrows) on positive charged particles

- The particle has an exactly **defined momentum** $p = p_0 + \Delta p$ with Δp being small compared to p_0. This approximation corresponds to a defined particle energy $\mathcal{E} = \frac{p^2}{2m} + m_0 c^2$.

- As only **single particles** are regarded, space charge effects are not considered.

- Particles travel with **relativistic velocities**. Influence of the magnetic field on the longitudinal velocity is negligible.

- **Dipole** fields have steering effects in one dimension. For the derivation of the equation of motion we chose the **horizontal dimension** x to represent dipole steering.

- All terms containing squares or products of x,y, and $\Delta p/p$ are neglected. This is justified because $x \ll R$, $y \ll R$ and $\Delta p/p \ll 1$

With this approximations the equation of motion 3.14 can be transformed into two decoupled linear equations of motions for the trajectory of a particle in a magnetic structure of an accelerator describing the independent motion of a particle for both transverse planes

$$\boxed{\begin{aligned} x''(s) + \left(\frac{1}{R^2(s)} - k(s)\right) x(s) &= \frac{1}{R(s)} \frac{\Delta p}{p} \\ y''(s) + k(s)\, y(s) &= 0 \ . \end{aligned}} \tag{3.18}$$

3.2.2. Solution of EQM and Matrix Formalism

Beamline elements consist mostly of pure dipoles and pure quadrupoles. For each case the equations of motion 3.18 reduce to simpler cases. As there is no coupling between the horizontal and vertical planes but their treatment is analogous, in the following only the horizontal x plane is described. For a perfect quadrupole where there is no dipole component in the field one can assume $\frac{1}{R} \approx 0$ and a constant quadrupole strength $k = \text{const}$. This reduces the first equation in Eq. 3.18 to

$$x''(s) - kx(s) = 0 \ . \tag{3.19}$$

This linear and homogeneous differential equation is similar to the harmonic oscillator and easy to solve. For example in the case of a defocusing magnet with $k > 0$ the solution is

$$x(s) = x_0 \cosh\sqrt{k}s + \frac{x_0'}{\sqrt{k}} \sinh\sqrt{k}s \tag{3.20}$$

$$x'(s) = x_0\sqrt{k} \sinh\sqrt{k}s + x_0' \cosh\sqrt{k}s \ . \tag{3.21}$$

For convenience both equations can be combined in a single operation by using matrix notation

$$\begin{pmatrix} x(s) \\ x'(s) \end{pmatrix} = \begin{pmatrix} \cosh(\Omega) & \frac{1}{\sqrt{k}} \sinh(\Omega) \\ \sqrt{k} \sinh(\Omega) & \cosh(\Omega) \end{pmatrix} \begin{pmatrix} x_0 \\ x_0' \end{pmatrix} \qquad \text{with} \quad \Omega = \sqrt{k}s \ . \tag{3.22}$$

With this notation the solutions of Eq. 3.19 for the different possible values of k are

$$\begin{pmatrix} \cos(\Omega) & \frac{1}{\sqrt{k}} \sin(\Omega) \\ -\sqrt{k} \sin(\Omega) & \cos(\Omega) \end{pmatrix}, \qquad \text{for } k > 0 \text{ (focus)} \tag{3.23}$$

$$\begin{pmatrix} 1 & s \\ 0 & 1 \end{pmatrix}, \qquad \text{for } k = 0 \text{ (drift)} \tag{3.24}$$

$$\begin{pmatrix} \cosh(\Omega) & \frac{1}{\sqrt{|k|}} \sinh(\Omega) \\ \sqrt{|k|} \sinh(\Omega) & \cosh(\Omega) \end{pmatrix}, \qquad \text{for } k < 0 \text{ (defocus)} \tag{3.25}$$

with now $\Omega = \sqrt{|k|}s$. The solution of the equation for y in Eq. 3.18 is identical but with k having always the opposite sign. Hence, the solutions reflect the property of quadrupoles

of focusing in one and defocusing in the other transverse plane. Therefore, both planes can be described simultaneously by simply combining the 2D matrices into 4D matrices

$$\mathbf{M_{FO}} := \begin{pmatrix} \cos(\Omega) & \frac{1}{\sqrt{k}}\sin(\Omega) & 0 & 0 \\ -\sqrt{k}\sin(\Omega) & \cos(\Omega) & 0 & 0 \\ 0 & 0 & \cosh(\Omega) & \frac{1}{\sqrt{k}}\sinh(\Omega) \\ 0 & 0 & \sqrt{k}\sinh(\Omega) & \cosh(\Omega) \end{pmatrix}, \qquad \text{for } k > 0 \text{ (focus)} \tag{3.26}$$

$$\mathbf{M_D} := \begin{pmatrix} 1 & s & 0 & 0 \\ 0 & 1 & 0 & 0 \\ 0 & 0 & 1 & s \\ 0 & 0 & 0 & 1 \end{pmatrix}, \qquad \text{for } k = 0 \text{ (drift)} \tag{3.27}$$

$$\mathbf{M_{DO}} := \begin{pmatrix} \cosh(\Omega) & \frac{1}{\sqrt{|k|}}\sinh(\Omega) & 0 & 0 \\ \sqrt{|k|}\sinh(\Omega) & \cosh(\Omega) & 0 & 0 \\ 0 & 0 & \cos(\Omega) & \frac{1}{\sqrt{|k|}}\sin(\Omega) \\ 0 & 0 & -\sqrt{|k|}\sin(\Omega) & \cos(\Omega) \end{pmatrix}, \quad \text{for } k < 0 \text{ (defocus).} \tag{3.28}$$

The block diagonal form of the matrices reflect the property that there is no coupling between the two planes. The multiplication of these matrices with the 4D transverse trace space vector of a particle

$$\vec{r} = \begin{pmatrix} x \\ x' \\ y \\ y' \end{pmatrix}$$

transforms the trace space according to the effect of a quadrupole field of length s and strength k or a free space drift section of length s.

3.2.3. Bunch Transport

The advantage of the matrix formalism is that the transformation of the trace space, i.e. a complete particle trajectory, through a sequence of ion optical devices can be modeled by simple matrix multiplications. For example one particle trajectory through focusing

Figure 3.5.: Plot of example trajectories in a quadrupole (QP) doublet calculated with the matrix formalism. The top image half shows the trajectory for the focusing-defocusing part. The bottom half shows the defocusing-focusing part.

FODO-structure as seen in Fig. 3.5 can be written as

$$\vec{r} = \mathbf{M_D}\left(d_3\right) \cdot \mathbf{M_{DO}}\left(k_{QP2}, L_{QP2}\right) \cdot \mathbf{M_D}\left(d_2\right) \cdot \mathbf{M_{FO}}\left(k_{QP1}, L_{QP1}\right) \cdot \mathbf{M_D}\left(d_1\right) \cdot \vec{r}_0 \ . \quad (3.29)$$

$d1$, $d2$ and $d3$ are the lengths of the free drift spaces, $k_{QP1/2}$ is the respective quadrupole strength and $L_{QP1/2}$ the respective quadrupole length. Executing all the matrix multiplications leads in the end to a single system matrix $\mathbf{M_{sys}}$ that represents the entire system. This reduces the effect of the system on a particle to a single matrix-vector multiplication

$$\vec{r} = \mathbf{M_{sys}} \cdot \vec{r}_0 \ . \quad (3.30)$$

So far this formalism describes the motion of an individual particle. However, the matrices can be also used to calculate the evolution of a bunch of particles through a guiding structure of magnets. To do so, it is necessary to use the above defined beam matrix or σ-matrix from Eq. 3.7. For a linear system, the transformation of the σ-matrix as a function of s by a guiding structure with the system (or transfer) matrix $\mathbf{M_{sys}}$ is given by

$$\sigma(s) = \mathbf{M_{sys}}(s)\sigma(0)\mathbf{M_{sys}^T}(s) \ . \quad (3.31)$$

This equation results from the conservation of trace space and the constant emittance before and after the beamline. For a rigorous derivation see [94, pp. 218–224].

3.2.4. Transverse Offsets

Due to limited positioning precision a real transport system can suffer from geometrical misalignments in different dimensions. Along the orbit of a quadrupole doublet this can be modeled by using different drift lengths. Transverse offsets of the magnetic

axis from orbit break the symmetry of the FODO structure and thereby introduce an additional net dipole moment that causes an overall transverse steering of the bunch in the laboratory system. However, a dipole causes a bending of the orbit along which the coordinate system moves. Therefore, it is not possible to calculate the difference between the unperturbed and the shifted orbit with the 4x4 matrices. It is necessary to introduce two more dimensions in order to be able to obtain transformations of the coordinate vector like

$$\begin{pmatrix} x - \Delta x \\ x' \\ 1 \\ y - \Delta y \\ y' \\ 1 \end{pmatrix} = \mathbf{M_{Trans}} \begin{pmatrix} x \\ x' \\ 1 \\ y \\ y' \\ 1 \end{pmatrix}$$

using the translation matrix

$$\mathbf{M_{Trans}}\left(\Delta x, \Delta y\right) = \begin{pmatrix} 1 & 0 & -\Delta x & 0 & 0 & 0 \\ 0 & 1 & 0 & 0 & 0 & 0 \\ 0 & 0 & 1 & 0 & 0 & 0 \\ 0 & 0 & 0 & 1 & 0 & -\Delta y \\ 0 & 0 & 0 & 0 & 1 & 0 \\ 0 & 0 & 0 & 0 & 0 & 1 \end{pmatrix}. \tag{3.32}$$

With this matrix one can represent transverse offsets Δx and Δy of any beamline element by multiplication of the element first with the $\mathbf{M_{Trans}}\left(\Delta x, \Delta y\right)$ and the result then with $\mathbf{M_{Trans}}\left(-\Delta x, -\Delta y\right)$. It represents the transformation of the coordinate system into the system of the misaligned beamline element. The propagation through the element is calculated and then the particle coordinates are shifted back into the original system.

Modeling this kind of alignment errors requires the expansion of all other 4×4 matrices to 6×6 matrices through zero padding and setting $M_{33} = M_{66} = 1$. With this extension of the formalism one can obtain the coordinates of a particle with respect to the original orbit. For a quadrupole, this way one avoids calculation of the additional dipole moment in the laboratory frame. The steering effect is included as the magnification effect of the positions $x - \Delta x$ and $y - \Delta y$ in the frame of the quadrupole. However, this calculation works only for individual particles and not for the beam envelope represented by the σ-matrix according to Eq. 3.31. The σ-matrix contains no information about the absolute position of the bunch in the laboratory frame but gives only its width around the orbit.

Transforming σ according to

$$\sigma = \mathbf{M_{Trans}} \sigma_0 \mathbf{M_{Trans}^T}$$

causes an unphysical broadening $\sigma_x^2 = \sigma_{0x}^2 + \Delta x^2$ of the bunch independent of the sign of Δx. That is why this matrix is only suited to determine the shift of the center of mass of the bunch caused by misalignment of the quadrupoles by calculation of the steering experienced by a orbit particle. In more formal terms, the conservation of phase space requires the transport matrices to represent bijective linear functions. One requirement for this is that the transport matrices are orthogonal, i.e. for any quadratic transfer matrix M it holds $M^T M = 1$ and $\det(M) = 1$. It is obvious that M_{Trans} does not fulfill this condition meaning that it is not suited to describe the bunch transport in terms of the σ-Matrix.

3.2.5. Geometric Optics

It is helpful for developing a better understanding of ion optics to introduce some analogies to geometric light optics. The first and very important element is the *thin lens*. For this approximation one assumes that the lens introduces an instantaneous change of angle $\Delta x'$ that depends linearly on the distance to the axis x_0

$$\Delta x' = -\frac{1}{f} x_0 \ . \tag{3.33}$$

f is called the focal length. For a focusing lens f is positive and for a defocusing lens it is negative. In matrix notation this can be written as

$$\begin{pmatrix} x \\ x' \end{pmatrix} = \begin{pmatrix} 1 & 0 \\ -\frac{1}{f} & 1 \end{pmatrix} \begin{pmatrix} x_0 \\ x_0' \end{pmatrix}, \quad \mathbf{M} = \begin{pmatrix} 1 & 0 \\ -\frac{1}{f} & 1 \end{pmatrix}. \tag{3.34}$$

With this formalism one can express the common lens equation that is valid for a point-to-point imaging with distance to object g and distance to image b

$$\frac{1}{g} + \frac{1}{b} = \frac{1}{f} \tag{3.35}$$

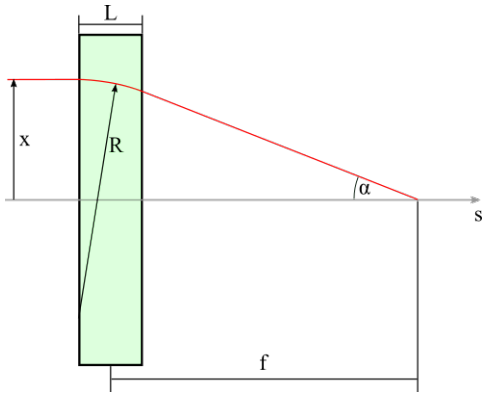

Figure 3.6.: Thin lens approximation of a quadrupole.

with a matrix equation

$$\mathbf{M} = \begin{pmatrix} 1 & b \\ 0 & 1 \end{pmatrix} \begin{pmatrix} 1 & 0 \\ -\frac{1}{f} & 1 \end{pmatrix} \begin{pmatrix} 1 & g \\ 0 & 1 \end{pmatrix} = \begin{pmatrix} -\frac{b}{g} & 0 \\ -\frac{1}{f} & -\frac{g}{b} \end{pmatrix} . \tag{3.36}$$

The demand of a point-to-point image is represented by the condition $M_{12} = 0$. The matrix element M_{11} indicates the magnification

$$V = \frac{b}{g} = -M_{11} \ . \tag{3.37}$$

For a *thin* quadrupole that introduces a small and instantaneous change of angle one can derive from Fig. 3.6 that

$$\begin{aligned} \tan\alpha &= \frac{x}{f} \\ \tan\alpha &= \frac{L}{R} = L \cdot \frac{q}{p} B_y = \frac{q}{p} \cdot \frac{dB_y}{dx} \cdot xL = kxL \\ &\rightarrow \frac{1}{f} = k \cdot L \ . \end{aligned} \tag{3.38}$$

This gives a better understanding for the quadrupole strength and shows that the two important parameters that determine the focal length of a quadrupole are the length and the gradient. Also, the sign of f is determined by the sign of k.

For the case of strongly focusing magnets where the assumption of a instantaneous change of angle is not valid, it is possible to treat a quadrupole as *thick lens*. In geometric optics a *thick lens* is characterized by focal planes F_1 and F_2 and two main planes H_1 and H_2 as seen in Fig. 3.7. In this case the focal length is defined as the distance between

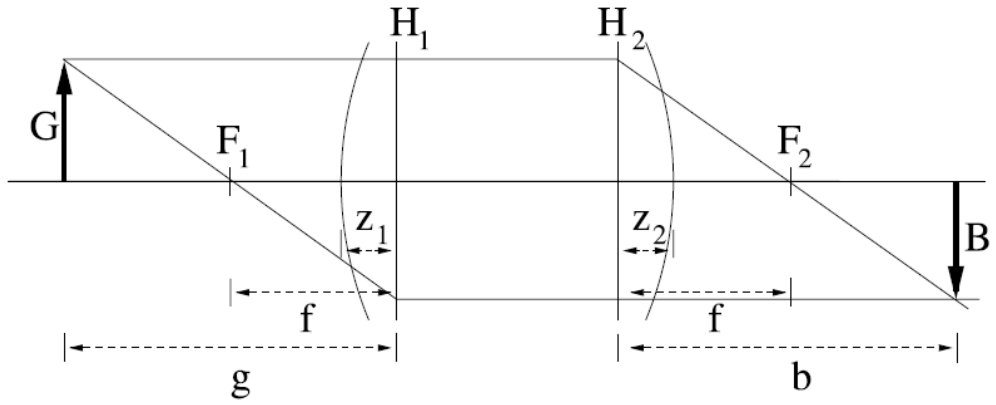

Figure 3.7.: Thick Lens. Image taken from [93]

the focal plane and the main plane and z_1, z_2 are the distances from the main planes to the front/back of the lens which depend on the total thickness of the lens L. In matrix representation the thick lens can be represented by the product

$$\mathbf{M} = \begin{pmatrix} 1 & z_2 \\ 0 & 1 \end{pmatrix} \begin{pmatrix} 1 & 0 \\ -\frac{1}{f} & 1 \end{pmatrix} \begin{pmatrix} 1 & z_1 \\ 0 & 1 \end{pmatrix} = \begin{pmatrix} 1 - \frac{z_2}{f} & z_1 + z_2 - \frac{z_1 z_2}{f} \\ -\frac{1}{f} & 1 - \frac{z_1}{f} \end{pmatrix}. \tag{3.39}$$

This representation is basically a combination of a thin lens and drifts. It takes into account that the trajectory between the main plains can be ignores because it is parallel and merges both planes into one with the effect of a thin lens. By inverting this equation it is possible to determine the focal length f

$$\begin{pmatrix} 1 & 0 \\ -\frac{1}{f} & 1 \end{pmatrix} = \begin{pmatrix} 1 & z_2 \\ 0 & 1 \end{pmatrix}^{-1} \begin{pmatrix} M_{11} & M_{12} \\ M_{21} & M_{22} \end{pmatrix} \begin{pmatrix} 1 & z_1 \\ 0 & 1 \end{pmatrix}^{-1} \tag{3.40}$$

yielding that

$$\frac{1}{f} = -M_{21}, \tag{3.41}$$

$$z_1 = \frac{M_{22} - 1}{M_{21}}, \tag{3.42}$$

$$z_2 = \frac{M_{11} - 1}{M_{21}}. \tag{3.43}$$

Inserting the elements of $\mathbf{M_{FO}}$ (Eq. 3.23) for a focusing quadrupole ($k > 0$) of length L

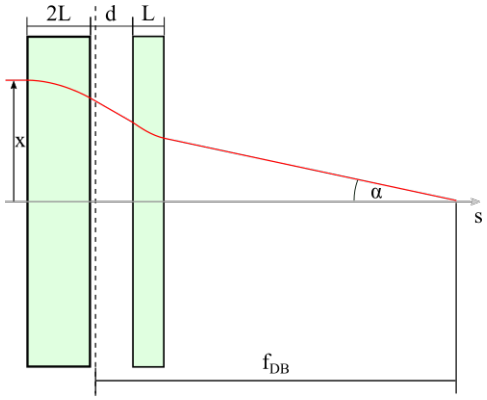

Figure 3.8.: Quadrupole doublet with thin lenses.

we obtain

$$\frac{1}{f} = \sqrt{k}\sin\left(\sqrt{k}L\right), \tag{3.44}$$

$$z_1 = \frac{\cos\left(\sqrt{k}L\right) - 1}{-\sqrt{k}\sin\left(\sqrt{k}L\right)}, \tag{3.45}$$

$$z_1 = z_2 \ . \tag{3.46}$$

This is consistent with the previous calculations since for small $\sqrt{k}L$ we recover the thin lens approximation $\frac{1}{f} = kL$ and $z_1 = z_2 = 0$. The calculation shows that every focusing or defocusing element can be represented by a combination of thin lenses and drift sections. When designing ion optical systems one can replace thick lenses with corresponding thin lenses. However, it is important to consider that the actual system is longer by $L - (z_1 + z_2)$.

One can calculate the transport matrix of a pair of quadrupoles with a drift length d between them using the thin lens approximation

$$\begin{pmatrix} 1 & 0 \\ -\frac{1}{f_2} & 1 \end{pmatrix}\begin{pmatrix} 1 & d \\ 0 & 1 \end{pmatrix}\begin{pmatrix} 1 & 0 \\ -\frac{1}{f_1} & 1 \end{pmatrix} = \begin{pmatrix} 1 - d/f_1 & d \\ -\frac{1}{f_1} - \frac{1}{f_2} + \frac{d}{f_1 f_2} & 1 - d/f_2 \end{pmatrix}. \tag{3.47}$$

For a thick lens we have to consider the main planes and use $\tilde{d} = z_1 + d + z_2$ and by using the relations 3.41, 3.42 and 3.43 we can write the combined focal length and main

plain positions

$$\frac{1}{f_{DB}} = \frac{1}{f_1} + \frac{1}{f_2} - \frac{\tilde{d}}{f_1 f_2} = \frac{f_1 + f_2 - \tilde{d}}{f_1 f_2}, \tag{3.48}$$

$$z_{1DB} = \frac{\tilde{d} f_1}{f_1 + f_2 - \tilde{d}}, \tag{3.49}$$

$$z_{2DB} = \frac{\tilde{d} f_2}{f_1 + f_2 - \tilde{d}} \,. \tag{3.50}$$

Because the case is of special relevance later, we will further investigate a pair of quadrupoles with same strength k but with the first quadrupole being twice as long as the other $L_1 = 2L_2 = 2L$. From Eq. 3.41 we know that for the case $f_1 > 0$ and $f_2 < 0$

$$\frac{1}{f_1} = \sqrt{k} \sin\left(2\sqrt{k}L\right), \tag{3.51}$$

$$\frac{1}{f_2} = -\sqrt{|k|} \sinh\left(\sqrt{|k|}L\right). \tag{3.52}$$

In the orthogonal plane this is just the opposite with $\frac{1}{f_1}$ having the negative sign and sinh-function and $f_2 > 0$ with sin-function. We have seen, that for small changes of angles, i.e. a long image distance, one can make the approximations $\sin\left(\sqrt{k}2L\right) \approx \sqrt{k}2L$ and $\sinh\left(\sqrt{k}L\right) \approx \sqrt{k}L$. In this case $z_1 = z_2 = 0$ and $\tilde{d} = d$. If inserted into Eq. 3.48 and simplified the result

$$\frac{1}{f_{DB}} = 2dk^2L^2 \pm kL \tag{3.53}$$

is obtained, with the positive sign for $f_1 > 0$ and $f_2 < 0$ (focusing-defocusing) and the negative sign for $f_1 < 0$ and $f_2 > 0$ (defocusing-focusing). This means that for a complete FODO structure the overall focal length depends on $|k| = \frac{q}{p}|g|$ where g is the magnetic field gradient and with the relativistic momentum being

$$p = \beta\gamma m_0 c = m_0 c\sqrt{\gamma^2 + 1} = m_0 c\sqrt{\left(1 + \frac{\mathcal{E}_{kin}}{\mathcal{E}_0}\right)^2 + 1} \,. \tag{3.54}$$

Finally, the focal length as a function of particle momentum reads

$$\frac{1}{f_{DB}} = \frac{2dL^2q^2g^2}{p^2} \pm \frac{qgL}{p} \,. \tag{3.55}$$

The different signs for the second term are for the two transverse dimensions and mean that for a given geometry the quadrupole doublet has different focal lengths in these

planes. When using a doublet in an imaging configuration this fact leads to different magnifications in x and y dimension.

3.3. Imaging with a Doublet

A pair of quadrupoles can be used to focus a bunch down to a minimal spot size. In theory the limit of this focus size is given by the transverse bunch emittance. It is conserved during transport and hence the bunch occupies always the same area in trace space (Liouville's theorem [94]). If the focusing is done appropriately the imaging conditions can be met and it is possible to transport bunch waist to bunch waist with a certain magnification. Imaging means here that all particles coming from the same point in space are transported to the same point in the focal plane. This condition for point-to-point imaging is met when the $M_{sys,12}$ and $M_{sys,34}$ elements of the system matrix vanish. For a doublet of thin lenses the system matrix in one plane consists of the product

$$\mathbf{M_{sys}} = \begin{pmatrix} 1 & d_3 \\ 0 & 1 \end{pmatrix} \begin{pmatrix} 1 & 0 \\ -\frac{1}{f_2} & 1 \end{pmatrix} \begin{pmatrix} 1 & d_2 \\ 0 & 1 \end{pmatrix} \begin{pmatrix} 1 & 0 \\ -\frac{1}{f1} & 1 \end{pmatrix} \begin{pmatrix} 1 & d_1 \\ 0 & 1 \end{pmatrix}. \tag{3.56}$$

The resulting matrix is complex and has large terms and will not be explicitly formulated. The analogous matrix represents the other plane. For a fixed distance from source plane to focus plane and a given particle energy one has to determine the required focal lengths f_1 and f_2 and drift lengths d_1, d_2 and d_3 that solve the equations $M_{sys,12} = 0$ and $M_{sys,34} = 0$. In case of fixed gradients and lengths of the quadrupoles the only free parameters stay the drift lengths. For the case where the total distance D from object to image is known, one can replace $d_3 = D - d_2 - d_1 - L_1 - L_2$. This reduces the problem to a set of two equations with two unknowns.

One way to solve this set of equations is a numerical and iterative approach. The values of the gradients and lengths of the quadrupoles are known. One starts by assuming an arbitrary value for d_1 and d_2 and computes the last drift

$$d_3 = D - d_2 - d_1 - L_1 - L_2$$

keeping now d_3 and d_2 fixed, one solves the equation

$$M_{sys,12}\left(d_1\right) = 0$$

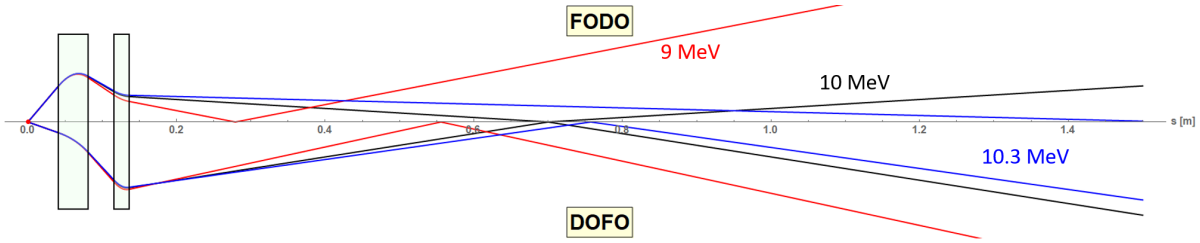

Figure 3.9.: Example trajectories through a PMQ doublet for protons with the design energy of 10 MeV and a higher and lower energy.

for d_1 and uses this updated value together with d_3 to solve

$$M_{sys,34}\left(d_2\right) = 0$$

for d_2. With these two new values for d_1 and d_2 one reenters the algorithm from the beginning, updating d_3 and solving the equations. After few iterations the values converge towards a solution, that solves the equations in both dimensions simultaneously and that correspond to the required drift lengths.

The corresponding picture for this approach is a common experimental lens alignment technique in optics. One iteratively reduces the focus size in one dimension with the first lens and in the second dimension with the second lens. Since this is a numerical solution, it is possible to calculate with the exact gradients and lengths.

3.4. Fluence Distribution and Spectrum in a Quadrupole Doublet Focus with a Polychromatic Ion Bunch

So far all calculations for the transverse phase space were done for a single particle or monoenergetic bunch. In the case of laser-accelerated particles the bunches exhibit a large energy spread. To a certain extend it is possible to include this energy spread in the matrix formalism. However, despite being a common approach in accelerator physics, this relies on the approximation that the energy spread is small. For laser-accelerated particles this is not valid and hence in the following we will pursue a different approach to model the effect of a quadrupole doublet on a polychromatic bunch of ions. This means one has to take into account the dependence of the quadrupole strength k on the particle momentum explicitly.

It has been shown above that for a fixed length and strength of the pair of quadrupoles, there exists one set of drift lengths that fulfill the imaging condition for a selected

particle energy at a desired distant focal plane. This energy is called the design energy. Nevertheless, in the case of a polyenergetic bunch, particles with energies different than the design energy enter the quadrupole field and are transported and focused in different planes before or behind the design focal plane as depicted for some example values in Fig. 3.9. As they are transported as well, these particles arrive in the design focal plane, too and contribute to the shape of the image in this plane. The distribution of these particles in the focal plane can be described by a function $N(x, y, p)$. From this distribution one can calculate two fundamental quantities that are of relevance, the number of particles per area called the *fluence* $F(x, y)$ and the momentum spectrum $S(p)$. The fluence is obtained via integration over the contributing particle momenta

$$\boxed{F(x,y) = \int N(x,y,p)\, dp} \tag{3.57}$$

and the spectrum via the spatial integration

$$\boxed{S(p) = \int\int N(x,y,p)\, dx\, dy.} \tag{3.58}$$

In order to reconstruct the shape of the bunch in the focal plane the contribution of every particle energy has to be summed for every point (x, y) in space, i.e. the fluence has to be calculated. There are different ways to make an ansatz for the particle distribution $N(x, y, p)$ in the focal plane. We have seen that the bunch width in both dimensions can be calculated for every energy at any position along the beamline like in Eq. 3.31 and that it is given by the diagonal elements of the σ-matrix 3.7. With the bunch size in both dimensions one can assume the bunch profile for every particle momentum to have a Gaussian distribution

$$N(x,y,p) = \frac{N(p)}{2\pi\sigma_x(p)\sigma_y(p)} \exp\left(-\frac{x^2}{2\sigma_x^2(p)} - \frac{y^2}{2\sigma_y^2(p)}\right). \tag{3.59}$$

The fluence and spectrum can be computed via numerical integration for a given absolute spectrum $N(p)$ by calculating the beam sizes $\sigma_x(p)$ and $\sigma_y(p)$ for discrete momenta. For example, the momentum spectrum is obtained from

$$S(p) = \int\int \frac{N(p)}{2\pi\sigma_x(p)\sigma_y(p)} \exp\left(-\frac{x^2}{2\sigma_x^2(p)} - \frac{y^2}{2\sigma_y^2(p)}\right) dx\, dy\ . \tag{3.60}$$

As general approach one can define a radius $r_f = \sqrt{x_{max}^2 + y_{max}^2}$ for the focus and due

to the symmetry of the problem it is sufficient to calculate the spectrum in the first quadrant, i.e. for $x \geq 0$ and $y \geq 0$.

Nevertheless, it is instructive and of some use to try to calculate the focal shape analytically. As a first simplification one can refrain from the Gaussian bunch profile and interpret the beam width in the focal plane $\sigma_{x/y}(p)$ to define ellipses according to

$$\frac{x^2}{\sigma_x^2(p)} + \frac{y^2}{\sigma_y^2(p)} = 1 \tag{3.61}$$

with the respective half axes and area

$$A(p) = \pi \sigma_x(p) \sigma_y(p). \tag{3.62}$$

One can assume that for all momenta the particles are uniformly distributed across the area of the respective ellipses yielding for the particle distribution

$$N(x, y, p) = \frac{N(p) \cdot \Theta(x, y)}{A(p)} = \frac{N(p) \cdot \Theta(x, y)}{\pi \sigma_x(p) \sigma_y(p)} \tag{3.63}$$

with

$$\Theta(x, y) \coloneqq \begin{cases} 1 & \text{if} \quad \frac{x^2}{\sigma_x^2(p)} + \frac{y^2}{\sigma_y^2(p)} \leq 1 \\ 0 & \text{else} \end{cases}. \tag{3.64}$$

The difference of this distribution model to the Gaussian case is expected to have a small influence on the resulting fluence distribution but it simplifies the integration in Eq. 3.57 and leaves to determine the functions $\sigma_x(p)$ and $\sigma_y(p)$ which at the same time determine the integration limits for x and y.

In the case relevant for this thesis the focal plane is far away from the quadrupole doublet and its length $L_{DB} = L_1 + d + L_2$ is much smaller than the focal length. Hence, we can assume a thin lens and use the lens equation 3.35. We further assume that the bunch diameter at the exit of the quadrupoles is approximately the same for every particle energy. Fig. 3.10 suggests that

$$\begin{aligned} \frac{x_{b_0}}{r_0} &= \frac{b(f) - b_0}{b(f)} \quad \text{for } f > f_0 \\ \frac{x_{b_0}}{r_0} &= \frac{b_0 - b(f)}{b(f)} \quad \text{for } f < f_0 \end{aligned} \tag{3.65}$$

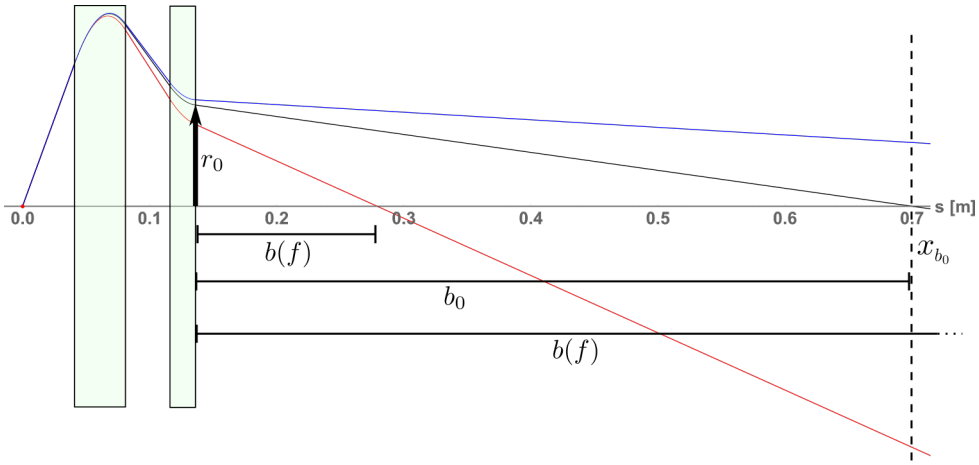

Figure 3.10.: Estimation of the $\sigma(p)$ functions.

further one can deduce from the lens equation that

$$\begin{aligned} & \frac{1}{g} = \frac{1}{f_0} - \frac{1}{b_0} = \frac{1}{f} - \frac{1}{b(f)} \\ \Leftrightarrow \quad & \frac{b_0}{f_0}\left(1 - \frac{f_0}{f}\right) = \frac{b(f) - b_0}{b(f)}. \end{aligned} \tag{3.66}$$

Combining both equations and considering both cases $f < f_0$ and $f > f_0$ we obtain

$$x_{b_0} = \frac{r_0 b_0}{f_0}\left|1 - \frac{f_0}{f}\right|. \tag{3.67}$$

If we now use the relation Eq. 3.55 between focal length for a doublet and momentum with $\frac{1}{f} = kL + 2dk^2L^2$, where $L = L_2 = L_1/2$ and $k = qg_x/p$, and identify x_{b_0} with $\sigma_x(p)$ we obtain a approximate description for the bunch size as a function of momentum in the focal plane

$$\sigma_x(p) = r_0 b_0 \left(\frac{2dL^2q^2g_x^2}{p_{0x}^2} + \frac{qg_xL}{p_{0x}}\right)\left|1 - \frac{p_{0x}^2}{p^2}\right| := a_x\left(p_{0x}\right)\left|1 - \frac{p_{0x}^2}{p^2}\right| \tag{3.68}$$

and in the y dimension

$$\sigma_y(p) = r_0 b_0 \left(\frac{2dL^2q^2g_y^2}{p_{0y}^2} + \frac{qg_yL}{p_{0y}}\right)\left|1 - \frac{p_{0y}^2}{p^2}\right| := a_y\left(p_{0y}\right)\left|1 - \frac{p_{0y}^2}{p^2}\right|. \tag{3.69}$$

This means that a_x and a_y are constants for one particular setup. To account for the minimal bunch size in the focal plane which is determined by the initial bunch size the

constants σ_{x0} and σ_{y0} are added.

$$\sigma_x(p) = a_x\left(p_{0x}\right)\left|1 - \frac{p_{0x}^2}{p^2}\right| + \sigma_{x0}, \quad \sigma_y(p) = a_y\left(p_{0y}\right)\left|1 - \frac{p_{0y}^2}{p^2}\right| + \sigma_{y0}\ . \tag{3.70}$$

For the case of ideal imaging p_{0x} and p_{0y} are the same. But in a general setting they can be slightly different for example due to inaccuracies of experimentally chosen drift lengths. Therefore, we introduce a common design momentum p_0 and the detuning $\delta \geq 0$ and define $p_{0x}^2 = p_0^2 - \delta^2$ and $p_{0y}^2 = p_0^2 + \delta^2$. Note that by this choice σ_x and σ_y depend only on the momentum squared and the design momentum. We can now define a new normalized quantities

$$p' \coloneqq \frac{p^2}{p_0^2} \quad \text{and} \quad \delta' \coloneqq \frac{\delta^2}{p_0^2} \tag{3.71}$$

to simplify the expressions of σ_x and σ_y and chose p' as new integration variable for the perspective integration of Eq. 3.57 for the calculation of the fluence. p' has no strict physical meaning except that for a non-relativistic consideration it represents the kinetic energy of an individual particle normalized to the design energy dictated by the choice of quadrupole settings. δ' is the normalized detuning between the x and y design energies, which is ideally zero. The explicit dependence of the momentum distribution $N(p)$ on the momentum is not necessarily well known. But because typically only particles with momentum close to $p' = 1$ contribute to the peak of the fluence distribution, a good first approximation can be expected for $N(p') \approx N(p' = 1) = N_0$ for a integration over p'. In this perspective it further makes sense to also normalize the quantities of space to common lengths $x' = x/a_x$, $\sigma_x' = \sigma_x/a_x$, $\sigma_{x0}' = \sigma_{x0}/a_x$ and the same for the y quantities. These normalizations now yield the expressions

$$\sigma_x'(p') = \frac{1}{p'}\left|p' - 1 + \delta'\right| + \sigma_{x0}', \quad \sigma_y'(p') = \frac{1}{p'}\left|p' - 1 - \delta'\right| + \sigma_{y0}'\ . \tag{3.72}$$

The product

$$\sigma_x'(p')\sigma_y'(p') = \frac{1}{p'^2}\left(\left|p' - 1 + \delta'\right| + \sigma_{x0}'p'\right)\left(\left|p' - 1 - \delta'\right| + \sigma_{y0}'p'\right)$$

represents the area to which particles with p' contribute to the fluence in the detection plane. Since both functions contain absolute magnitudes one has to distinguish different

cases that define the different sections of the integrand function:

$p' \geq 1 + \delta'$:

$$\begin{aligned}\sigma'_x(p')\sigma'_y(p') &= \frac{1}{p'^2}\left(p' - 1 + \delta' + \sigma'_{x0}p'\right)\left(p' - 1 - \delta' + \sigma'_{y0}p'\right) \\ &= \frac{1}{p'^2}\left(p'\left(\sigma'_{x0} + 1\right) + \delta' - 1\right)\left(p'\left(\sigma'_{y0} + 1\right) - \delta' - 1\right)\end{aligned}$$

$1 + \delta' > p' \geq 1 - \delta'$:

$$\begin{aligned}\sigma'_x(p')\sigma'_y(p') &= \frac{1}{p'^2}\left(p' - 1 + \delta' + \sigma'_{x0}p'\right)\left(-p' + 1 + \delta' + \sigma'_{y0}p'\right) \\ &= \frac{1}{p'^2}\left(p'\left(\sigma'_{x0} + 1\right) + \delta' - 1\right)\left(p'\left(\sigma'_{y0} - 1\right) + \delta' + 1\right)\end{aligned}$$

$p' < 1 - \delta'$:

$$\begin{aligned}\sigma'_x(p')\sigma'_y(p') &= \frac{1}{p'^2}\left(-p' + 1 - \delta' + \sigma'_{x0}p'\right)\left(-p' + 1 + \delta' + \sigma'_{y0}p'\right) \\ &= \frac{1}{p'^2}\left(p'\left(\sigma'_{x0} - 1\right) - \delta' + 1\right)\left(p'\left(\sigma'_{y0} - 1\right) + \delta' + 1\right).\end{aligned}$$

The three cases look very similar and differ only in certain signs. To combine the three cases to a single expression one can use the sign function

$$sgn(x) \coloneqq \begin{cases} -1 & \text{if} \quad x < 0 \\ 0 & \text{if} \quad x = 0 \\ 1 & \text{if} \quad x > 0 \end{cases} \tag{3.73}$$

and define the auxiliary functions $s_1 = sgn\left(p' - 1 + \delta'\right)$ and $s_2 = sgn\left(p' - 1 - \delta'\right)$. Now the expression is for the ellipse area

$$\frac{1}{p'^2}\left(p'\left(\sigma'_{x0} + s_1\right) + s_1\delta' - s_1\right)\left(p'\left(\sigma'_{y0} + s_2\right) - s_2\delta' - s_2\right).$$

We further substitute:

$$\begin{aligned}s_{x1} &= \sigma'_{x0} + s_1 \\ s_{x2} &= -s_1\left(1 - \delta'\right) \\ s_{y1} &= \sigma'_{y0} + s_2 \\ s_{y2} &= -s_2\left(1 + \delta'\right)\end{aligned}$$

and finally obtain the simplified expression for the product

$$\sigma'_x(p')\sigma'_y(p') = \frac{1}{p'^2}\left(p's_{x1} + s_{x2}\right)\left(p's_{y1} + s_{y2}\right). \tag{3.74}$$

With the introduced constant particle number N_0 and the assumed elliptical particle distribution (Eq. 3.63) it is possible to write the integration Eq. 3.57 as

$$F(x,y) = \int \frac{N_0}{\pi\sigma'_x(p')\sigma'_y(p')}\,dp' = \frac{N_0}{\pi}\int \frac{p'^2}{\left(p's_{x1} + s_{x2}\right)\left(p's_{y1} + s_{y2}\right)}\,dp'. \tag{3.75}$$

$\Theta(x,y)$ does not appear anymore in the integrand since it is considered in the $\sigma'_{x/y}$ and will be taken into account during the determination of the limits for the integration variable p'. Performing the integration yields the indefinite integral

$$\tilde{F}(p') = \frac{N_0}{\pi}\left[\frac{p'}{s_{x1}s_{y1}} + \frac{1}{s_{x1}s_{y2} - s_{x2}s_{y1}}\left(\frac{s_{x2}^2}{s_{x1}^2}\ln\left(s_{x1}p' + s_{x2}\right) - \frac{s_{y2}^2}{s_{y1}^2}\ln\left(s_{y1}p' + s_{y2}\right)\right) + C\right] \tag{3.76}$$

where the limits and integration constant C for the integration still need to be found and inserted. In order to do so we first observe the integrand of Eq. 3.75. This function has poles at

$$p' = -\frac{s_{x2}}{s_{x1}} = \frac{s_1\left(1-\delta'\right)}{s_1 + \sigma'_{x0}} \quad \text{and} \quad p' = -\frac{s_{y2}}{s_{y1}} = \frac{s_2\left(1+\delta'\right)}{s_2 + \sigma'_{y0}}\,.$$

This poles persist in the logarithmic functions in the indefinite integral but lie outside the definition interval of p' so no divergence is caused by these terms. A discontinuity happens at $p' = 1 \pm \delta'$ in the indefinite integral function due to the switch of the sign of sgn. It is a sectionwise monotonically increasing function that can become continuous by a suiting choice of C. If one investigates the behavior of Eq. 3.76 around the discontinuities, one can find that for the case $p' \to 1 - \delta'$ the constant needs to be

$$C_{1-\delta'} = \tilde{F}\left(p' = 1-\delta'\right)^- - \tilde{F}\left(p' = 1-\delta'\right)^+$$

and in the case $p' \to 1 + \delta'$

$$C_{1-\delta'} = \tilde{F}\left(p' = 1+\delta'\right)^- - \tilde{F}\left(p' = 1+\delta'\right)^+$$

where the superscript $+$ and $-$ indicate the sign of s_1 and s_2 in the respective cases. This shows that for the constant C one also needs to distinguish the three cases according to

the sections

$$C = \begin{cases} 0 & p' < 1 - \delta', \\ C_{1-\delta'} & 1 - \delta' \leq p' < 1 + \delta', \\ C_{1+\delta'} + C_{1-\delta'} & p' \geq 1 + \delta'. \end{cases} \tag{3.77}$$

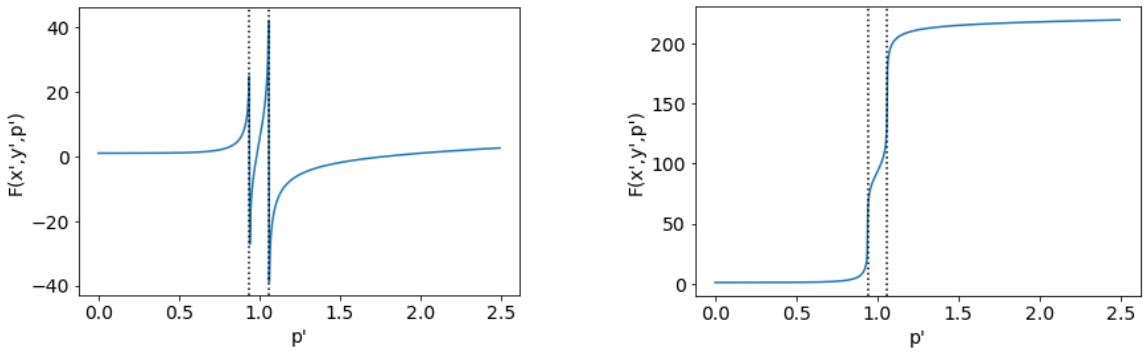

Figure 3.11.: Example for the correction of the indefinite integral function via the proper choice of integration constant for $\delta' = 0.06$. Dashed lines mark the positions of $p' = 1 - \delta$ and $p' = 1 + \delta$.

Further, $\tilde{F}(p')$ is not defined in the cases $s_{x1} = 0$, $s_{y1} = 0$ and $s_{x1}s_{y2} - s_{x2}s_{y1} = 0$. But as long as σ'_{x0}, $\sigma'_{y0} > 0$ and σ'_{x0}, $\sigma'_{y0} \neq 1$ holds, $s_{x1} \neq 0$ and $s_{y1} \neq 0$. This is generally the case. One can calculate that under these assumptions for

$$\delta' = \frac{s_1\sigma'_{y0} - s_2\sigma'_{x0}}{s_1\sigma'_{y0} + s_2\sigma'_{x0} + 2s_1s_2} \tag{3.78}$$

it results $s_{x1}s_{y2} - s_{x2}s_{y1} = 0$. One can imagine that there are different combinations of parameters that fulfill this equation but it has special meaning for the case $\delta' = 0$ where according to their definitions $s_1(p') = s_2(p') = s(p)$ and the two poles of $\tilde{F}(p')$ merge to a single pole at $p' = 1$. From Eq. 3.78 one can see that $s_{x1}s_{y2} - s_{x2}s_{y1} = 0$ for $s(\sigma'_{x0} - \sigma'_{y0}) = 0$ which persists for any choice of C. At $p' = 1$ the sign functions $s_1 = s_2 = 0$ lead then to the divergence of the integral. One can avoid this case by defining $s_1(0) = s_2(0) = 1$ that does not alter the previous definitions and calculations since the cases $p' \geq 1 + \delta'$ and $1 - \delta' \leq p' < 1 + \delta'$ yield the same results. Nevertheless, $s(\sigma'_{x0} - \sigma'_{y0})$ always gets 0 for $\sigma'_{x0} = \sigma'_{y0}$. This singularity of the integral function for $\delta' = 0$ cannot be resolved but is of no concern since the function stays continuous around

it[1]. The numerical computation of the function though works up to an arbitrarily small difference between σ'_{x0} and σ'_{y0}. This resolution is sufficient for all investigations in this work.

After having found and smoothed the definite integral, it remains to find the limits for the integration variable p'. These limits introduce the spatial dependency. Following the reasoning above, figuratively, one can imagine that at a certain point (x', y') in the focal plane contributions to the fluence only come from particles of energies with bunch ellipses that cover this point. In other words only the p' contribute to the fluence in this point where the ellipse equation

$$\frac{x'^2}{\sigma'^2_x(p')} + \frac{y'^2}{\sigma'^2_y(p')} \leq 1 \tag{3.79}$$

is fulfilled. Rearranging yields a 4^{th} order inequation in p' which is cumbersome to solve. In the following we will therefore limit the calculations to the case of lineouts along the $x' = 0$ and $y' = 0$ axis. Although it is not a complete description of the fluence in the focal plane, it is both a possibility to obtain a rather simple instructive analytic expression and simultaneously the most relevant case for a comparison with experimental data due to the symmetry axes of the system.

Because of the symmetry of the problem it is possible to limit to the case $x', y' \geq 0$. For the cases $x' \leq \sigma'_{x0}$ and $y' \leq \sigma'_{y0}$ particles of all momenta contribute to the fluence because it corresponds to the minimum size of the image of the incoming bunch. In this case one can integrate over the hole spectrum. We call the lowest momentum p_l (typically defined by foils through which the particles are passing before being registered at the detector) and the highest p_h (typically defined by the maximum ion energy in a spectrum). For the case that $x' > \sigma'_{x0}$ and $y' > \sigma'_{y0}$ the momenta close to the design momentum do not contribute to the fluence because their bunch ellipse is too small to cover this point. Hence one has to exclude these close to design energies from the integration by introducing additional integration limits p'^- and p'^+. We start by rearranging Eq. 3.79

[1] It can be shown by a short calculation that function assumes a form like $\ln(\xi)/(\xi-1)$ where $\xi = \sigma'_{x0}/\sigma'_{y0}$ and which behaves well and continuous around $\xi = 1$.

and inserting Eqs.3.72 and obtain

$$\text{for } x' = 0: \quad y' \leq \sigma'_y = \frac{1}{p'} \left| p' - 1 - \delta' \right| + \sigma'_{y0}$$

$$p' > 1 + \delta': \quad p' \geq \frac{1 + \delta'}{1 - \left(y' - \sigma'_{y0} \right)} = p'^{-}_y \tag{3.80}$$

$$p' < 1 + \delta': \quad p' \leq \frac{1 + \delta'}{1 + y' - \sigma'_{y0}} = p'^{+}_y \tag{3.81}$$

$$\text{for } y' = 0: \quad x' \leq \sigma'_x = \frac{1}{p'} \left| p' - 1 + \delta' \right| + \sigma'_{x0}$$

$$p' > 1 - \delta': \quad p' \geq \frac{1 - \delta'}{1 - (x' - \sigma'_{x0})} = p'^{-}_x \tag{3.82}$$

$$p' < 1 - \delta': \quad p' \leq \frac{1 - \delta'}{1 + x' - \sigma'_{x0}} = p'^{+}_x \ . \tag{3.83}$$

These limits can be calculated and inserted in the indefinite integral Eq. 3.76 and the lineout of the fluence along the axis.

This model allows to investigate the influence of different parameters on the expected focus shape. Fig. 3.12 shows the resulting lineouts in x and y for different choices of the minimum spot sizes σ'_{x0} and σ'_{y0}. The detuning δ' was set to a fixed value and the minimum and maximum contributing momenta were chosen as broad as expected for LION sources. $p'_l = 0.1$ and $p'_h = 2$ correspond respectively to 1.2 MeV and 23.9 MeV protons at a design energy of 12 MeV. On can observe, that a larger minimum spot size leads to a shallower spatial gradient of the fluence. Thereby due to the normalization to a_x and a_y the influence is equal for both dimensions. The overall size of the fluence peak depends strongly on the energy detuning δ'. The larger the detuning the larger the width of the fluence distribution lineout (Fig. 3.13).

Whereas the changes in the offsets were two orders of magnitude, a factor of two stronger detuning leads to a twice broader distribution. So even if $\sigma'_{x0} > 0$ and $\sigma'_{y0} > 0$ the smallest focus is achieved for $\delta' = 0$ and the detuning affects the spot size strongest. From this observation one can deduce that for the experimental configuration that yields the smallest spot size is $\delta' = 0$.

With regard to the spectrum, from Fig. 3.14 it is evident, that the main contribution to the fluence comes from particles close to the design momentum. Limiting the global extent of the spectrum by p'_l and p'_h has mainly an impact on the pedestal of the distribution. This reflects the fact that the closer the particle momenta are to the design momentum

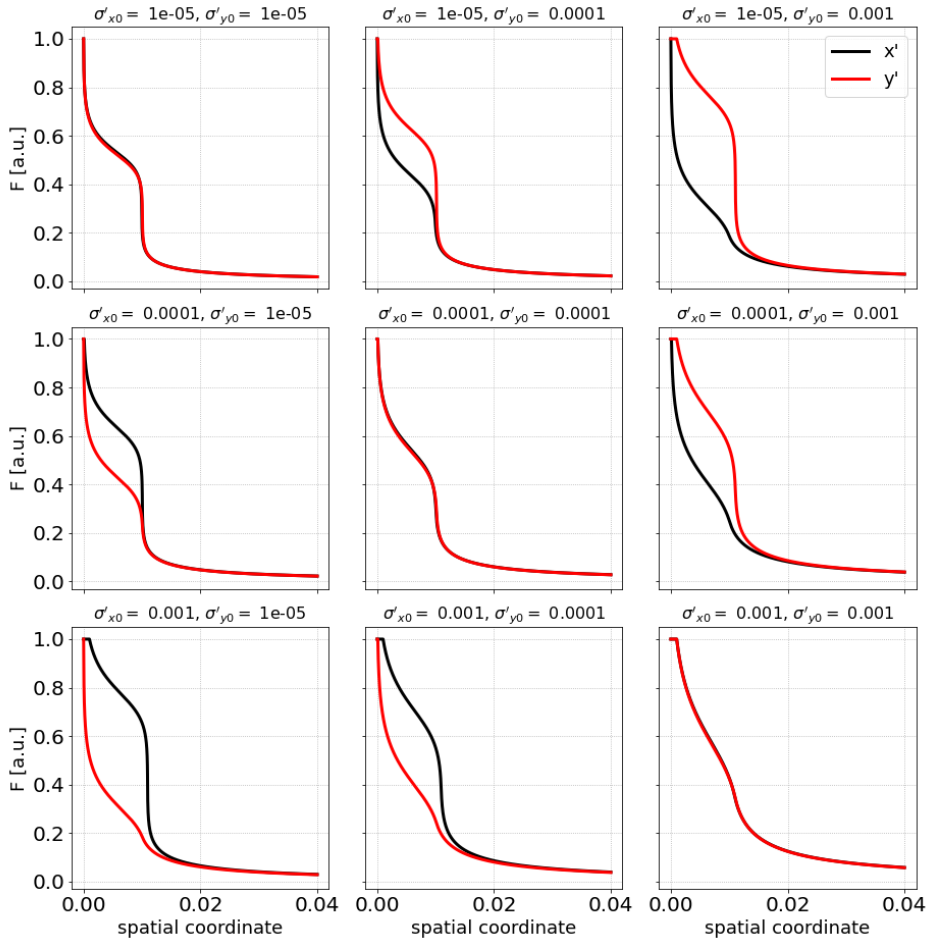

Figure 3.12.: Influence of a variation of σ'_{x0} and σ'_{y0} on the focus shape with fixed $p'_l = 0.1$, $p'_h = 2$ and $\delta' = 0.005$.

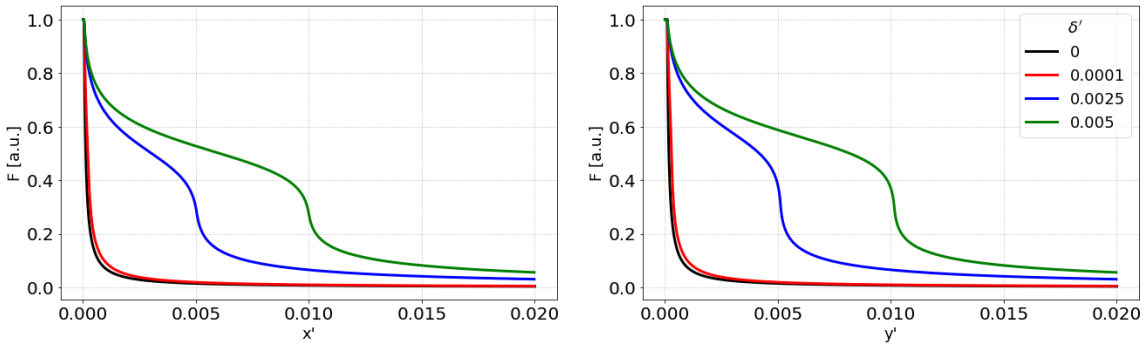

Figure 3.13.: Focus shape for different values of δ' and fixed values of $\sigma'_{x0} = 1 \cdot 10^{-4}$, $\sigma'_{y0} = 0.5 \cdot 10^{-4}$ and $p'_l = 0.1$, $p'_h = 2$.

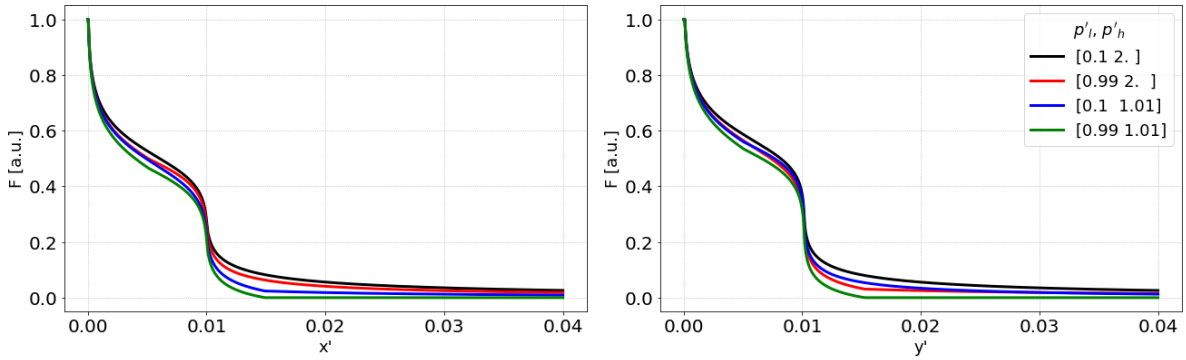

Figure 3.14.: Contribution of different spectral parts to the focus shape for fixed $\sigma'_{x0} = 1 \cdot 10^{-4}$, $\sigma'_{y0} = 0.5 \cdot 10^{-4}$ and $\delta' = 0.005$.

the better they are focused leaving the contributions at larger distance to the center to particles with momenta well above or below the design value. A consequence is that the exact choice of p'_l and p'_h is not critical for the determination of the fluence distribution as long as they contain a range of few percent around the design momentum. In experiment conditions these values are in general given by boundary conditions limiting the spectrum such as remaining material in the beam path or the detector bandwidth. Therefore, one can conclude that the stopping of very low energy particles in beamline elements will not affect the measured focus shape. It is important to note that under perfect alignment condition, that is $\delta' = 0$, the shape is mainly determined by the minimum possible spot at a certain design momentum, $\sigma'_{x0}(p')$ and $\sigma'_{y0}(p')$. This will enable determining the energy dependent source size in the course of the experimental work.

The analysis of the model leads to the conclusion that the smallest focus, i.e. fluence distribution is expected to appear for $\delta' = \sigma'_{x0} = \sigma'_{y0} = 0$. It represents the case of perfect imaging of a perfect point source where all design energy particles are focused to the axis. It is a special case of the above discussed discontinuity of the integral function and therefore the fluence diverges at $x' = y' = 0$ which impedes the definition of a width of the resulting lineouts. Hence, it is impossible to determine a lower limit for the focus size using this calculation[2]. Instead, due to the well behavior of the integral function an approximation to $\sigma'_{x0} = \sigma'_{y0} \approx 0$ can be used. Rescaling with the setup dependent factors $a_x\,(p_{0x})$ and $a_y\,(p_{0y})$ will later allow to estimate a minimum focus size under consideration of the influence of the broad energy spectrum (see Sec. 4.6).

[2]However, it is a case that can be solved analytically yielding a 2D fluence distribution function. The solution is shown in the appendix of this work.

4. The Laser-Ion Beamline at the Centre for Advanced Laser Applications

This chapter presents the first focusing setup in the laser-driven ion (LION) acceleration experiment in the Centre for Advanced Laser Applications (CALA) which is powered by the ATLAS3000 laser. Under current operation conditions in the commission phase this system is able to deliver a 28 cm diameter laser beam of up to 8 J in 28 fs to the LION experiment chamber. The laser is focused by a f/5 off-axis parabolic (OAP) mirror to a 4.6 µm full-width at half-maximum (FWHM) diffraction limited focal spot [95]. It hits under 6.7° onto a thin plastic foil (formvar) which is mounted on a automatic positioning system [96] that is able to replace the foil with 0.5 Hz repetition rate and in its updated version has a wheel that can store up to 760 targets in 19 different sections.

The focusing setup design goal was to collect as many of the emitted ions as possible and to focus them to a remote location from the particle source which is the laser target. Therefore, the focusing elements had to be capable of being positioned in close proximity to the laser focus and target. As the laser-target interaction happens in vacuum, the focusing setup had to be not only vacuum compatible but also capable of focusing the ions through a vacuum exit window at 1.845 m distance to the target. For the first realization of the setup a pair of compact and strong permanent magnet quadrupoles (PMQs) was chosen as suitable device. In the context of different works these magnets were characterized [31, 97] and a positioning setup was developed to allow the motorized and precise positioning of the doublet downstream of the laser target [31]. Based on these achievements, here the setup and properties of the first LION doublet shall be summarized and analyzed. The treatment comprises the PMQs themselves and their positioning but also the radiation and laser protection measurements implemented in the setup. Further, the detectors used for the measurements within this work are introduced. Finally, it will be shown how the expected fluence distribution and spectrum in the focal plane are calculated. The extension of the beamline with a second doublet will be treated in a subsequent chapter.

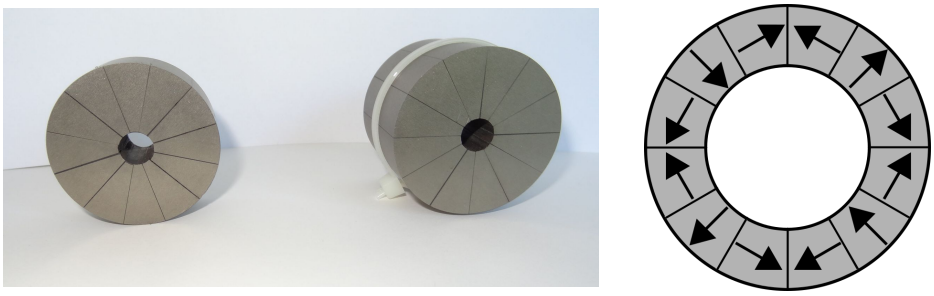

Figure 4.1.: The Halbach design PMQs of the LION experiment in CALA with the magnetization scheme.

4.1. Permanent Magnet Quadrupoles

The focusing elements in the CALA LION experiment are PMQs. They have the advantage that they can be built very small without loss of magnetic field strength allowing to create high field gradients. They are passive devices with constant fields and hence no need for power supply, a property that makes them insensitive to the occurring electro magnetic pulse (EMP) and hence suitable for the use close to the laser plasma interaction. Another advantage is that no special cooling is required when used in vacuum.

Every quadrupole consists of 12 wedges of NdFeB magnets arranged in a cylinder with a bore and magnetized according to a Halbach design [98]. This special arrangement of magnetization creates a quadrupole field inside the bore. A focusing unit combines one PMQ of 40 mm and one of 20 mm length. The quadrupoles have a total diameter of 50 mm including a bore diameter of 10 mm (Fig. 4.1). The effective magnetic gradients of the PMQs were determined via two different methods. The magnetic field was measured with a three axis hall probe and the gradients calculated via both, field evaluation and numerical particle tracking simulations [31, 97]. Additionally, to experimentally check the simulations and calculations, the quadrupole doublet was used to focus a parallel 20 MeV proton beam generated by a Tandem van de Graaff accelerator. From the here determined focal length, an effective gradient could be deduced. It was also possible to confirm that the central part of the quadrupole fields behave like ideal quadrupole fields when using this effective gradients for the beam transport calculations. This allows a sufficiently accurate modeling of the setup by means of the matrix formalism. The descriptions and results are explained in [97] and are given in Table 4.1.

	Length	Gradient sim.	Gradient exp.
PMQ 1	40 mm	(329 ± 12) T/m	(332 ± 13) T/m
PMQ 2	20 mm	(333 ± 13) T/m	(334 ± 13) T/m

Table 4.1.: Gradients of the LION doublet PMQs according to [97]

4.2. Doublet Setup and Free Parameters

Two permanent magnets were combined to form a doublet with first the longer, i.e. stronger magnet PMQ 1 and second the shorter magnet PMQ 2. In general, the aim of the setup in LION is to create a proton focus at different distances to the laser target foil, i.e. the source of the protons. The position outside the vacuum chamber is of particular interest, as it allows various applications of the laser-accelerated protons. As the magnets are fixed in length and gradient, i.e. in their quadrupole strength, the only free parameters to adjust the focusing properties of the doublet were the drift lengths. The first drift length d_1 is determined by the distance between the laser target foil and PMQ 1 entrance. The second drift length d_2 is the distance between the magnets and the third the distance from the exit of PMQ 2 and the desired focus d_3. The overall (laser) target-focus-distance (TFD) defines the position of the focus along the beamline and is the sum of the drift lengths and the quadrupole lengths. It is typically determined by external circumstances in the experimental setup and a fixed parameter which is identical to D from Sec. 3.3 leaving d_1 and d_2 as the main tunable setup parameters.

The quadrupoles are positioned downstream of the target with a motorized positioning setup consisting of three motorized linear stages, three manual linear stages, one motorized and one manual goniometer. A long transverse motorized stage along the x direction allows to introduce and remove the doublet to and from the beamline as required. The

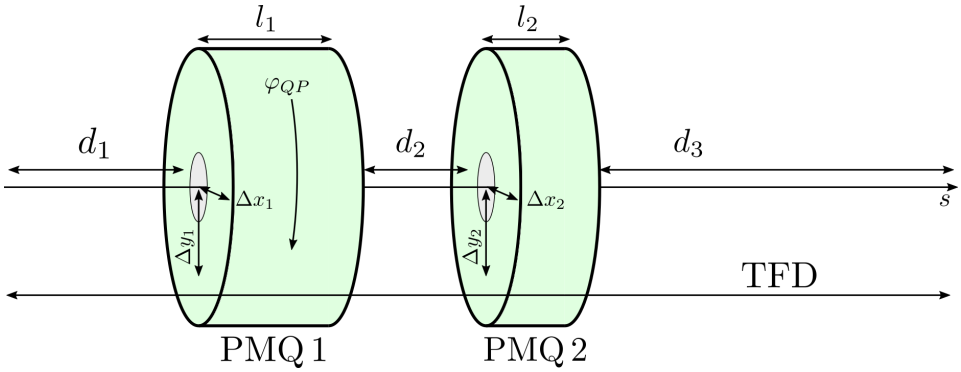

Figure 4.2.: Drifts and lengths for the doublet setup.

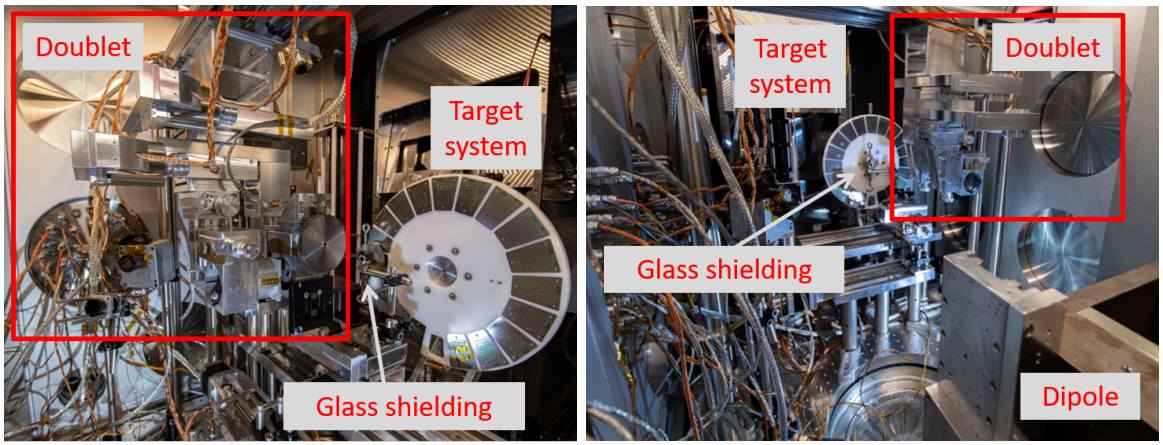

Figure 4.3.: Focusing setup in the LION vacuum chamber together with the glass shielding in front of the target positioning system. Adapted from image by T. Naeser.

two other motorized stages are used to set d_1 and d_2 independently. Therefore one stage moves both PMQs together along the beamline and one moves only PMQ 2. The manual stages are for absolute alignment in y and relative alignment in x. The goniometers are used to align and optimize the relative angle between the focusing planes of the PMQs to 90°. This means that in summary there are four degrees of freedom that can be changed remotely during the experiment, namely the drifts d_1 and d_2, the overall transverse x position and the relative angle between the focusing planes φ_{QP}. The quadrupoles are oriented such that PMQ 1 focuses in the vertical, i.e. y dimension, and PMQ 2 focuses in the horizontal, i.e. x dimension. The setup is shown in Fig. 4.3 inside the LION vacuum chamber and in front of the target positioning system (wheel).

Before installation in the vacuum chamber, the setup was pre-aligned in order to minimize the relative alignment errors between the two magnets. For that the magnetic fields of the PMQs mounted in the positioning setup were measured sequentially with a motorized three-axis hall probe which served as reference for the magnetic axes. The procedure is described in greater detail in [31]. With a particle tracking code the magnetic axes of the measured fields were determined and with iterative field measurements, using the degrees of freedom of the setup, the relative transverse offset was minimized and the relative angle φ_{QP} set to 90°. The precision of this alignment was given mainly by the precision of the positioning devices but also by the achievable resolution of the magnetic field measurement determined by the size of the hall probe. The accuracy of the alignment is estimated to be on the order of 0.1° for φ_{QP} and 200 µm for the transverse offsets which correspond to the scale on the goniometer and the size of the measurement tip of the hall probe.

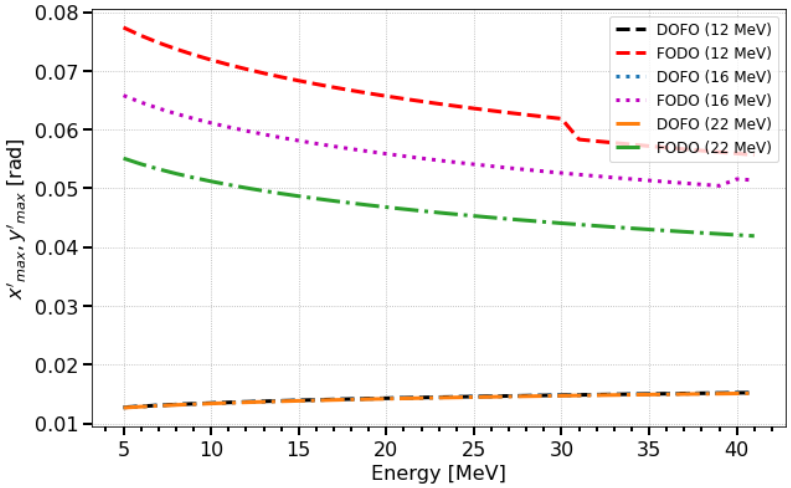

Figure 4.4.: Calculated maximum acceptance angles x'_{max} and y'_{max} as function of incoming proton energy calculated in defocusing x dimension (DOFO) and focusing y dimension (FODO) for three different design energy setups (12, 16 and 22 MeV.

4.3. Acceptance and Radiation Shielding

The limited bore of the PMQs represents an intrinsic geometric limit to the angles under which protons can enter the doublet. Only particles on trajectories with an maximum excursion smaller than the bore diameter can be focused. Particles with too large initial divergence are absorbed at some point along their trajectory through the doublet causing not only a loss of particles but also a degradation of the magnetization, activation and damage of the magnets over time. Here, we define acceptance as the maximum angle with respect to the central axis through the doublet under which a proton can enter PMQ 1 and still exit PMQ 2. Due to the nature of the focusing, the maximum angles are different in the x and y dimensions. A detailed calculation of the acceptance angles is given in [97]. The acceptance angles x'_{max} and y'_{max} depend on the drift lengths and the design energy of the setup. In the y dimension (FODO) the dominating condition is that the maximum bunch trajectory inside PMQ 1 has an extension smaller than the bore. In the x dimension (DOFO) the maximum excursion happens inside PMQ 2.

Applying these conditions for fixed drift lengths determined by the design energy yields an energy dependent behavior of the acceptance angles that is shown in Fig. 4.4 for a TFD of 1.845 m. For different sets of drift lengths, every particle energy present in the incoming bunch has a different acceptance angle. The kink in the curves results from a transition

between different cases in the calculation of the acceptance angles [97]. In theory, by reducing the bunch divergence at any position before the doublet to the acceptance, the absorption in the magnets is minimized as only protons that are transmitted enter the doublet. The divergence reduction can be achieved by an aperture of a defined size placed at a defined distance. Protons with a divergence surpassing the acceptance would be dumped around the aperture. The ideal aperture size depends on the selected drift lengths (i.e. design energy) as well as the particle energy. A perfect aperture would be required to be energy selective and adapt as the drift lengths changed. But due to space restrictions around the target this was not possible to realize in a first setup. As seen in Fig. 4.4 the acceptance in DOFO dimension is almost independent of both of these parameters. This can be explained by the weaker focusing strength of PMQ 2 and the pre-selection made by PMQ 1. Therefore, in this dimension a fixed size aperture is a reasonable implementation to tailor the bunch divergence to the acceptance. The accepted angles in FODO get smaller with higher particle energies as the effect of the magnetic fields is weaker. For the same reason the drift lengths increase with design energy causing an additional decrease of accepted divergence angles for all particle energies. However, the dependence of the acceptance on the drift lengths is stronger than on the proton energy. Hence, an aperture that adapts with the drift lengths only, without being tailored to the proton bunch energy distribution is already a first approximation to reduce radiation. As a compromise for both dimensions it was decided to use a fixed size aperture mounted directly on the upstream surface of the first quadrupole and moving with it. Although this ignores the energy dependence of the acceptance completely, it is a first simple geometric approach to protect the magnets from both radiation and target debris.

The setup was equipped with a plate with an elliptical aperture as seen in Fig. 4.5. It was machined in 1 mm aluminum with 3 mm maximum aperture in y and 6 mm maximum aperture in x dimension. This plate is able to stop up to 13 MeV protons and was designed for a previous setup of the PMQs which is described in [31]. The size was chosen according to an acceptance that would prevent proton energies of 5 MeV to be absorbed in PMQ 1 at a TFD of 1.3 m. For the drift lengths used in the current setup this aperture corresponds to angles between 30 to 45 mrad in y dimension (FODO) and 60 to 90 mrad in x dimension (DOFO)[1]. Fig. 4.5 also shows the installed plate after several experimental campaigns with up to 8 J on target. The ablation and damage due to laser

[1]The reader will realize that the aperture should be rotated by 90° to fit better the calculated acceptance. Indeed, this was a mistake that revealed itself only during the data analysis. Its influence will be analyzed later.

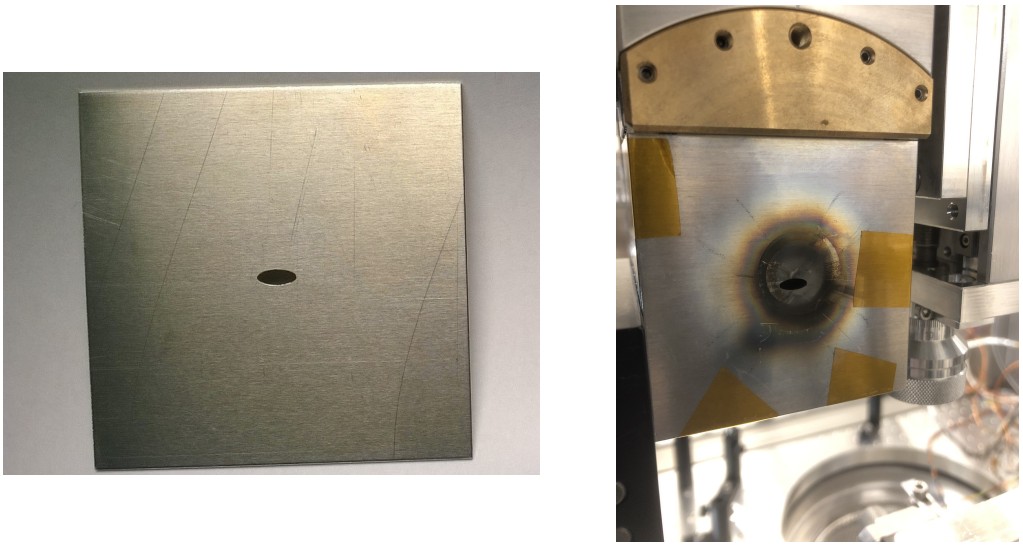

Figure 4.5.: Aluminum shielding with elliptical aperture mounted in front of PMQ 1.

light and radiation is clearly visible around the aperture. For further protection a tube of aluminum with 300 µm wall thickness is inserted in the bore of the magnets. It absorbs protons with less than 3.5 MeV but also electrons that enter the magnetic field and are turned around. Further, protons above 13 MeV that can penetrate the aluminum cover plate with the aperture will then have a reduced energy causing them to be deflected and stopped inside the tube. Also, PMQ 2 is covered with a 1 mm aluminum plate with an aperture of the same size as the magnet bore diameter to protect the magnet bulk from particles exiting the first PMQ without being further transported through the second.

The front aperture determined the divergence as a function of the aperture size and its distance from PMQ 1 to the source d_1. With the approximation of a point source the divergence can be calculated as

$$x'_{ap}\left[y'_{ap}\right] = \frac{(3.0 \pm 0.2)\,\text{mm}\,[(1.0 \pm 0.2)\,\text{mm}]}{d_1}. \tag{4.1}$$

The uncertainty is estimated on the basis of two contributions, the uncertainty of the machining of the aperture and its centric positioning in front of the magnet paired with the fact that the magnetic axis is not along the geometric center of the PMQ. As will become clear later, the error of d_1 can be estimated with 1 mm and it has largest influence for the shortest $d_1 = 47.8$ mm at 12 MeV design energy. A propagation of the errors with this d_1 leads to an estimate of the error of x' and y' of 4 mrad.

Fig. 4.6 illustrates the influence of the chosen aperture on the bunch divergence in two example cases of 12 MeV and 22 MeV design energy which represent the relevant

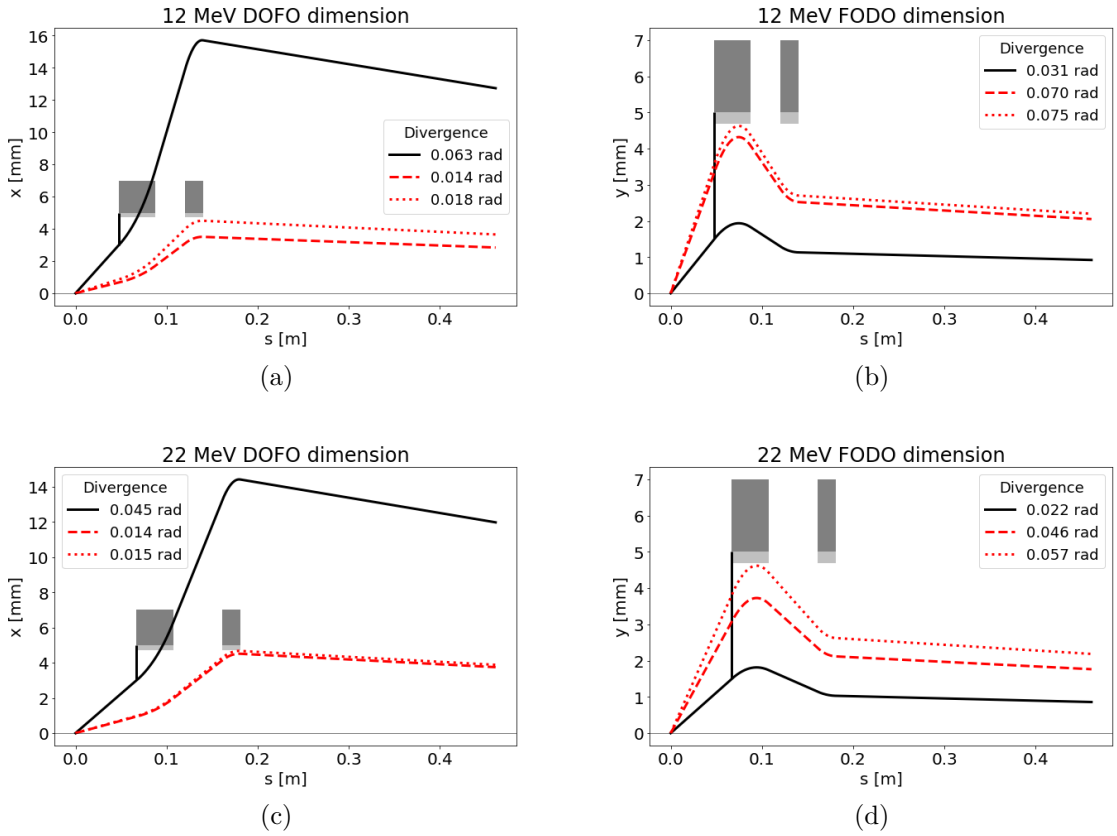

Figure 4.6.: Trajectories of 12 MeV and 22 MeV design particles through the doublet in x dimension (a), (c) and in y dimension (b), (d). The gray and silver boxes indicate the bores of the PMQs and the thickness of the inserted aluminum shielding tube, the vertical lines the front aperture. The black solid curves correspond to a particle divergence x'_{ap}/y'_{ap} as defined by the aperture. The red dashed line show a trajectory with the maximum divergence according to the calculated acceptance x'_{max}/y'_{max}. The red dotted line is a trajectory for a manually adjusted acceptance used for error estimation.

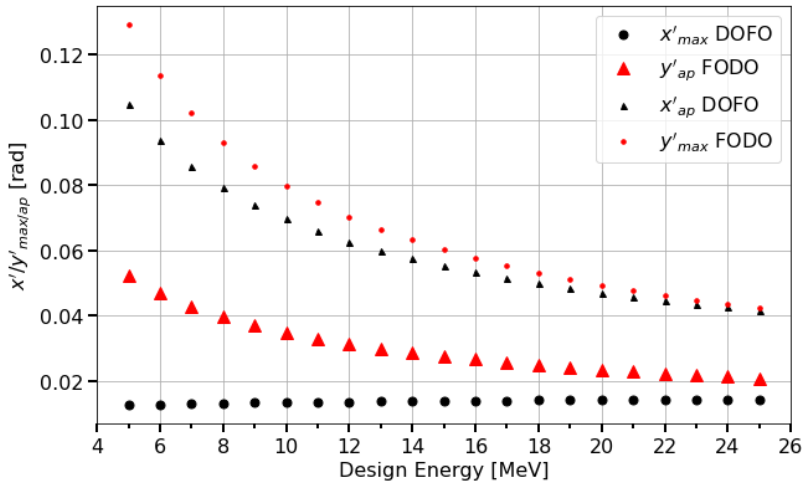

Figure 4.7.: Bunch divergence x'_{ap}/y'_{ap} as defined by the aperture in the LION experiment from Fig. 4.5 together with the calculated design energy acceptance x'_{max}/y'_{max} as a function of design energy. The larger markers indicate the divergence of relevance for the respective dimension.

design energy range in this work. It shows the trajectories in unbounded magnetic fields of design energy particles that, because of the energy selectivity of the doublet, are meaningful representatives of the transported energy interval. The gray and silver boxes in the image background represent the magnet bulk as well as the thickness of the inserted aluminum shielding tube. Further, the vertical lines indicate the extent of the front aperture. The solid black curves represent aperture defined divergence x'_{ap}/y'_{ap}. One can see, that in DOFO dimension the chosen aperture is too large allowing divergences x'_{ap} that will be absorbed by PMQ 1. In this dimension the transmitted bunch divergence is determined by the smaller acceptance x'_{max} drawn in Fig. 4.6 as red dashed line. The aperture has only little protective effect since there is a large number of particles dumped inside PMQ 1 and can be ignored for considerations on the transmission through the setup. On the other hand in DOFO dimension, the aperture restricts the divergence more than necessary. For both design energies the acceptance y'_{max} is by a factor 2 larger than y'_{ap}. Therefore, the aperture absorbs more particles than necessary reducing the overall fluence in the focus, in first approximation by the same factor 2.

An extension of this analysis of the relation between x'_{ap}/y'_{ap} and x'_{max}/y'_{max} towards a larger range of design energies can be seen in Fig. 4.7. It shows how the different divergences (marker style) behave in the two dimensions (colors). For every dimension the respective smaller divergence will be the dominating for the transmission of the doublet

(larger marker). Like observed for the two examples, this is in the FODO dimension y the aperture divergence y'_{ap} and in DOFO dimension x the acceptance x'_{max}. An ideal aperture would rise the red triangles to the red dots and lower the black triangles to the black dots.

y'_{ap} has the expected more pronounced dependence on the design energy and decreases for the relevant cases from $y'_{ap} = 31\,\text{mrad}$ at 12 MeV to $y'_{ap} = 22\,\text{mrad}$ at 22 MeV. The error of y'_{ap} was estimated above to be 4 mrad.

For the acceptance in x dimension one obtains $x'_{max} = 14\,\text{mrad}$ for both 12 MeV and 22 MeV respectively reflecting the very weak dependence of this quantity on the design energy. One can see from Fig. 4.6 that an error remains for the result of the acceptance calculation. To estimate that error of x'_{max} trajectories with manually set divergence were added to to the figure with the constraint to have a maximum excursion within the indicated magnet bore. Comparing the manually found values to the calculated allows to set $x'_{max} = (16 \pm 2)\,\text{mrad}$ for 12 MeV and $x'_{max} = (14 \pm 1)\,\text{mrad}$ for 22 MeV meaning that an energy independent acceptance can be approximated with the mean $\hat{x}'_{max} = (15 \pm 2)\,\text{mrad}$. Therefore, for all subsequent calculations we use the acceptance $\hat{x}'_{max}$ and $y'_{ap}\,(d_1)$ as maximum divergences in the respective dimension.

For future improvements of the setup one can calculate with knowing the drifts length d_1 that the acceptance in x and y dimension (see Fig. 4.6 (b), (d)) for 12 MeV corresponds to a width at the PMQ 1 surface of 1.4 mm in x (DOFO) and 6 mm in y (FODO). In the high energy case with 22 MeV design energy widths result to be 1.8 mm in x and 5.6 mm in y. Hence, in the investigated design energy range using a fixed size aperture with the dimensions 1.4 mm in x and 5.6 mm in y could increase both the protection of the magnet bulk and the total particle number arriving in the focal plane by a factor of six compared to the studies presented here.

4.4. Laser Light Shielding

The doublet is positioned close to the laser target and hence to the laser focus. This causes additional challenges in the operation of the doublet as the magnets need to be protected from both, radiation and intense laser light. Laser light can be transmitted to a certain amount through the target but also accidentally delivered shots without any target can hit the quadrupole surface. This is critical for two reasons, one because the quadrupole surface suffers ablation and second because significant amount of light can be reflected back into the laser chain risking severe damage to laser components. In order to

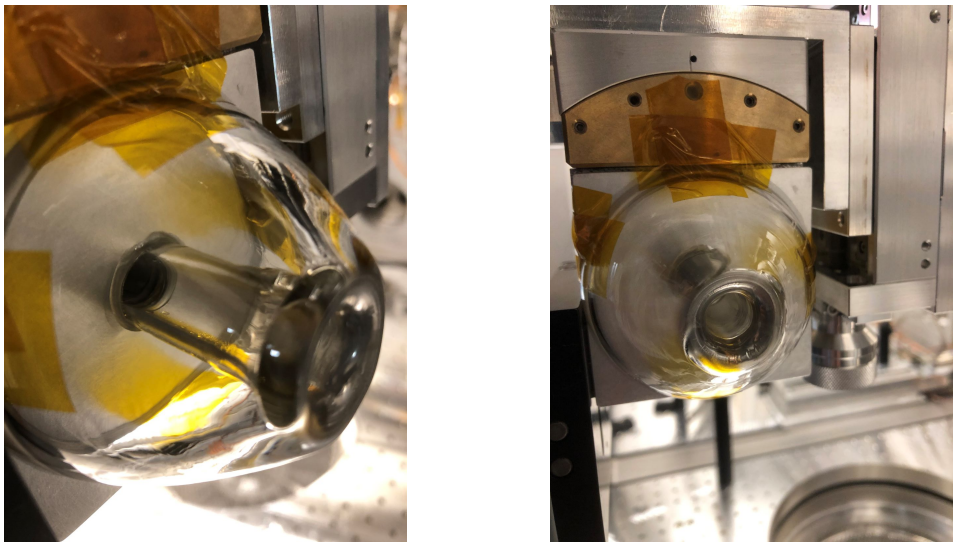

Figure 4.8.: Glass cone with aluminum shielding mounted in front of PMQ 1.

Figure 4.9.: Glass shielding for laser light guidance and back reflex protection.

reduce these damage risks protection measures were implemented. In a first step a glass cone with a 1 cm bore glass tube in the center was manufactured and glued to a 5 mm aluminum plate. Also, the plate exhibited a 1 cm bore diameter. Plate and cone were mounted in front of PMQ 1 for first experiments with accelerated protons. This meant that they moved together with the quadrupoles. A photograph of the setup is seen in Fig. 4.8.

In a second iteration it was decided to install the above mentioned thin aluminum plate for reduction of divergence and to decouple the laser protection from the quadrupole motion. A 3 cm long glass tube with 1 cm bore diameter was glued to a 6 cm diameter 5 mm thick glass disc with a 1 cm bore diameter. It is shown in Fig. 4.9.

This shielding was mounted on a three axis stage between target and quadrupoles

Figure 4.10.: Positioning system of the glass laser shielding in front of the target wheel.

(Fig. 4.10). This allowed to insert and remove the shielding and to align it both on the beamline axis and as close to the target as possible in order to reduce the minimum achievable d_1. The 28 cm diameter laser is focused with a f/5 OAP mirror under 6.7° with respect to the target normal onto the target. The bore diameter was chosen such that for this geometry a transmitted laser pulse would hit the inner wall of the glass tube and under multiple reflections be guided to the rear exit of the tube and hence not be reflected back into the laser chain. Glass was chosen due to its high damage threshold.

4.5. Detection

Regarding possible applications it is of special interest to focus the protons to a spot on air outside the vacuum chamber as indicated in Fig. 4.11. The air vacuum interface represents an inevitable transition through material when delivering the protons to any application on air. The LION vacuum exit window consists of a 50 µm Kapton polyimide foil which is covering an 8 cm long and 1 cm broad vertical slit. Since Kapton is partially transparent to light, additionally a 12 µm aluminum foil covers the exit window to prevent stray light to exit the chamber. According to SRIM [99,100] calculations, the combination of these foils is thick enough to stop 2.1 MeV protons.

For transmitted protons, the transverse bunch profile can be heavily influenced by the pass through matter which has to be considered when trying to characterize and

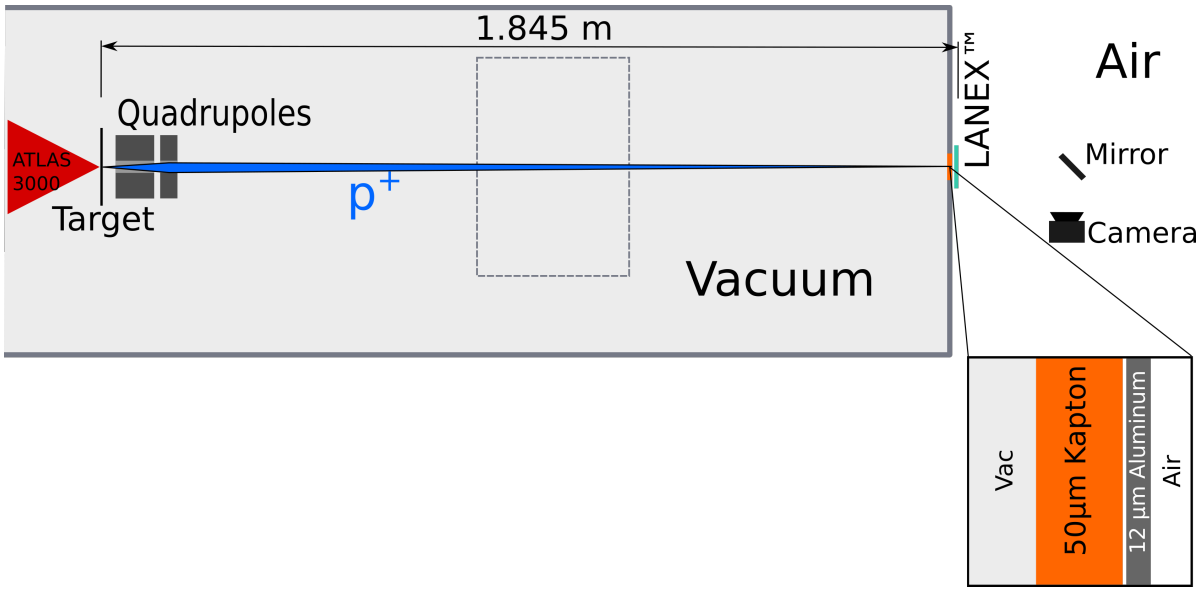

Figure 4.11.: Scheme of the doublet focusing setup in CALA LION with the scintillator setup for proton focus imaging. The gray dashed box indicates the position of the dipole that can be inserted into the beamline. Th right box is a zoom into the layers of the exit window. Dimensions are not to scale.

understand the focal shape. Scattering leads to an unwanted broadening of the focus and is potentially one limit for the smallest possible focus. A good tool to assess this effect are 3D Monte Carlo simulations with the Fluka code [101, 102] that include scattering in their particle matter interaction models. Its influence was evaluated by simulating the transition of a proton pencil beam through the sequence of foils forming the exit window. The beam was modeled as a perfectly collimated monoenergetic flat top beam with 100 µm diameter. Beams with energies of 10 and 20 MeV were simulated in order to get an upper and lower boundary for the effect in the relevant energy range. The beam profile was recorded at 1.5 and 2.5 cm after the exit window. This corresponds to a range of distances to the exit window in which detectors are positioned during the experiments.

The simulation results can be seen in Fig. 4.12. A lineout through the center of the focus is taken as a measure for the beam size. As expected the beam size depends on both the proton energy and the distance to the foils. Protons with 10 MeV are scattered more than 20 MeV protons and the larger the distance on air the more the influence of the scattering in the foil is visible. Mainly the divergence gained in the exit window leads to beam expansion which is demonstrated by simulation of a direct air/vacuum interface in Fig. 4.12b. The resulting beam size at FWHM is only half of the one obtained with exit

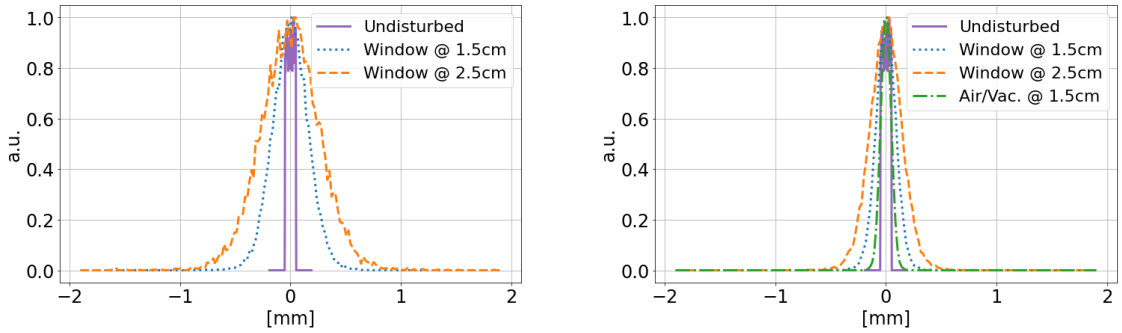

(a) (b)

Figure 4.12.: Results from Fluka simulations of the vacuum exit window made of 50 µm Kapton and 12 µm aluminum for (a) 10 MeV and (b) 20 MeV protons. Particle numbers were normalized.

window. This can be explained by the more than 1000 times higher density of Kapton and almost 3000 times higher density of aluminum compared to air. Therefore the scattering in 50 µm of Kapton is similar to the effect caused by 5 cm propagation in air and 12 µm aluminum correspond to around 3 cm air length. For this reason, ignoring the Kapton and aluminum interface reduces the scattering by about a factor of two. According to the stochastic nature of the process, the scattered profile results in a Gaussian distribution, which is confirmed by fitting a Gaussian function to the simulated data (Fig. 4.13). The FWHM of the fits are a factor of 2 to 6 larger than the initial beam. From the FWHM and the distance to the foil a divergence angle α can be calculated via

$$\tan(\alpha) = \frac{FWHM - 100\,\mu m}{2 \cdot Distance\ in\ Air}$$

yielding a divergence of around 9 mrad for 10 MeV and around 4 mrad for 20 MeV protons. The scattering in the exit window has a non-negligible effect on the focus broadening. In order to observe the smallest spot it is recommended to focus the protons onto the exit window and position the particle detector directly on top of it. This reduces the contribution of scattering to a minimum and eases the assessment of any correlation between focus shape and beamline or source properties. Data presented in this thesis use mostly this setup, therefore, the broadening of the beam due to scattering is estimated to stay below 10 µm.

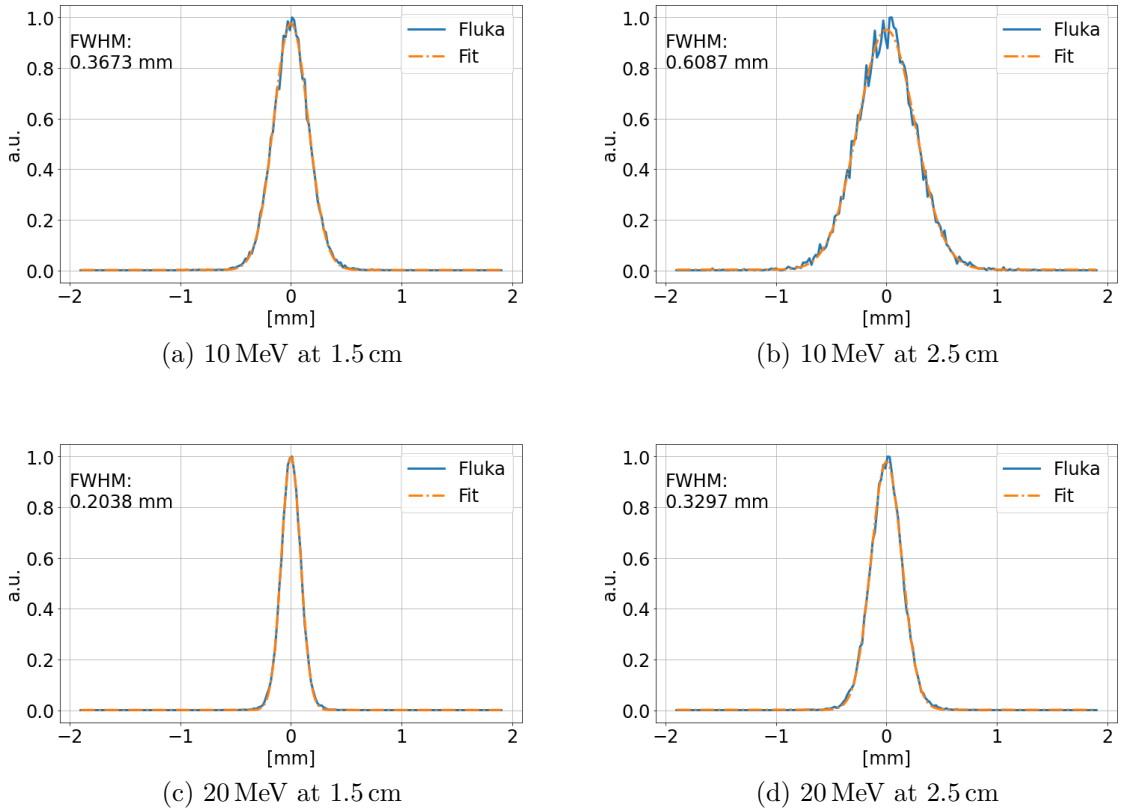

(a) 10 MeV at 1.5 cm (b) 10 MeV at 2.5 cm

(c) 20 MeV at 1.5 cm (d) 20 MeV at 2.5 cm

Figure 4.13.: Fits to the results from Fluka simulations of the vacuum exit window for 10 MeV and 20 MeV protons.

4.5.1. Scintillator

As primary detector we use a LANEX^{TM} scintillator screen which is a Gd_2O_2S:Tb granular phosphor screen [103]. The scintillator was imaged via a mirror and two lenses onto a CCD camera (Fig. 4.14) in front of which neutral density filter were installed to adjust the signal intensity. In a first setup (Fig. 4.14a) the screen was mounted on a motorized stage in order to be able to remove it from the beamline with the white phosphor facing the mirror. This resulted in a distance from the exit window to the screen of (2.5 ± 0.2) cm and an image resolution of (19 ± 2) µm per pixel which was determined via an image of a ruler. In a second configuration (Fig. 4.14b), used for most of the focus characterization experiments, the effect of scattering was minimized by mounting the screen directly on the exit window with the phosphor towards the window. In this configuration the achieved image resolution was (15 ± 2) µm per pixel. The combination of camera position, lenses and mirror result in an image inverted in the horizontal x

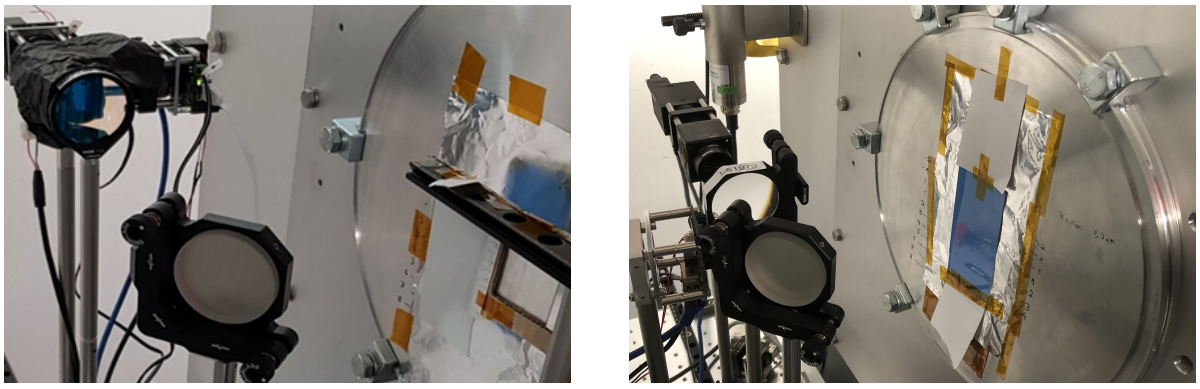

(a) (b)

Figure 4.14.: Scintillator setups for proton focus imaging.

dimension leading to an image in beams eye view.

4.5.2. Radiochromic Films

Occasionally we used radiochromic film (RCF) stacks for absolute dosimetry [104]. A RCF is a self developing film consisting of an active layer and polyester support substrates. The active layer darkens under the effects of ionizing radiation and is sensitive to photons as well as charged particles. For this work EBT3 films were used which have a symmetric structure with a 28 µm thin active layer sandwiched in between two 125 µm polyester bases [105]. The scintillator screen was removed and instead previously calibrated RCF stacks of 20 layers were used to analyze the maximum proton energy, the transverse bunch profile and the depth dose profile in the proton focus [106, 107]. Due to the motorization of the stack positioning, the distance to the exit window of these detectors was a few centimeters.

4.5.3. Image Plates

An image plate (IP) was used for capturing the proton focus with high dynamic range. An IP is a film detector based on photo-stimulated luminescence comprising trapping centers where charge carriers accumulate depending on the deposited energy of incident particles [108]. This creates a latent image of the incident radiation that can be read out via optical stimulation and depletion of the trapping centers. The image plates were fixed directly on the aluminum foil of the exit window. After irradiation an IP is scanned multiple times until the image exhibits no more saturated pixels. The multiple readouts

can be composed to a high dynamic range image and it is also possible to reconstruct the dose distribution deposited in the film [109].

4.5.4. Wide Angle Spectrometer

It is possible to insert and remove a 10 cm long and around (150 ± 20) mT strong permanent magnet dipole with an iron yoke into the beamline. This magnet can be used to steer the bunch downwards in y direction and is useful for analysis of the bunch. Combined with a 200 µm thin horizontal entrance slit and a CMOS detector it serves as wide angle spectrometer (WASP) for analysis of the bunch energy spectrum [110]. The detector is covered with aluminum layers of different thickness representing a lower energy cutoff of the measurable spectrum.

4.6. Doublet Focus Shape Calculation

In order to asses any measured focus shape it is necessary to have an estimate of the best, i.e. smallest achievable focus. Since the gradients of the PMQs have been determined, an expected focus shape can be calculated for a given design energy and drift lengths by integration of Eq. 3.57. The found analytic solution allows only to calculate lineouts for a flat spatial source distributions. To implement also other distributions, the integration of Eq. 3.57 is performed directly numerically using a $N(x, y, p)$ where the σ_x and σ_y are obtained through the matrix formalism. This numerical approach yields a 2D fluence distribution that allows to compare not only the width of the proton focus but also its transverse position to experimental measurements.

As input to the calculations we must provide the proton spectrum and the energy dependent bunch sizes. To correctly respect the contributions of different proton energies close to the design energy, which have a large influence on the total focus shape, it is important to have sufficient energy resolution. The required resolution was calculated for different design energies $\mathcal{E}_0$, i.e. drift lengths, by demanding that the difference between the design energy spot size $\sigma_{x/y}(\mathcal{E}_0)$ and the spot size $\sigma_{x/y}(\mathcal{E}_0 + \Delta\mathcal{E})$, produced by a bunch of energy $\mathcal{E}_0 + \Delta\mathcal{E}$, has to be equal to the detector pixel resolution of 15 µm. For every design energy the corresponding drift lengths were calculated and the system matrix set up for $\mathcal{E}_0$ and $\mathcal{E}_0 + \Delta\mathcal{E}$. As initial particle distribution a point source was assumed represented by the initial matrix σ^s. This means that the width of the initial particle distribution at the source were set to $\sigma_x^s = 0$ and $\sigma_y^s = 0$. The divergence y'_{ap}

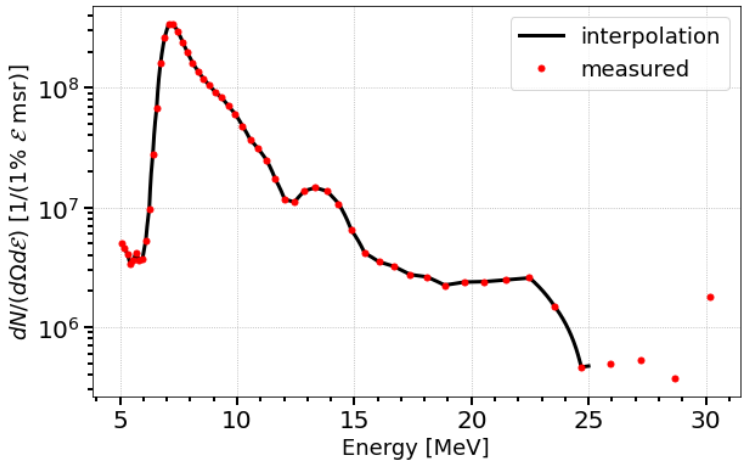

Figure 4.15.: Differential spectrum from Shot 5 on May 12, 2021 on a 600 nm target foil with approx. 8 J on target. Spectrum measured with the WASP after a 6.48 MeV aluminum cutoff layer.

was determined with d_1 according to Eq. 4.1 giving the matrix element $\sigma^s_{y'} = y'_{ap}$. As the relevant energy interval in this work ranges from 12 MeV to 22 MeV, for the orthogonal divergence the energy independent mean $\hat{x}'_{max} = 15$ mrad was used for $\sigma^s_{x'}$. The remaining elements of the σ^s-matrix were set to 0. The spot sizes σ_x and σ_y were then calculated by transporting the source matrix σ^s through the system matrix M_{sys} to the image plane with the method introduced in chapter 3. By means of a minimization algorithm it was found that the smallest resolution in both dimensions needs to be 3 keV for the 12 MeV design energy setup and 9 keV for 22 MeV. Therefore, to be safe to obtain plausible results for all cases the resolution was set to $\Delta\mathcal{E} = 2$ keV independent for all design energies.

The absolute momentum spectrum $N(p)$ of the proton bunch is estimated from the differential spectrum $\frac{dN}{d\Omega d\mathcal{E}}$ obtained from WASP measurements. One exemplary spectrum is shown in Fig. 4.15 and was selected as representative for one of the experimental days used for the focus characterization measurements. The laser and target parameters used for the reference spectrum are comparable to the ones in the focusing experiments (always around 8 J in around 5 µm FWHM and 28 fs on formvar targets of 400 nm or 600 nm thickness). This allowed to reduce systematic errors in the fluence calculation that would arise from substantially different particle numbers due to different laser energy or target material and thickness. Nevertheless, shot-to-shot fluctuations prevailed during all studies. The energy resolution of the measurement is much larger than the required

2 keV. Therefore, the values in between measurements are interpolated linearly. From the differential spectrum given in $\frac{1}{msr\,1\%\mathcal{E}}$ the absolute particle numbers per energy interval with central energy $\mathcal{E}$ can be calculated by

$$N(\mathcal{E}) = \frac{dN(\mathcal{E})}{d\Omega d\mathcal{E}} \cdot \Delta\Omega \cdot \Delta\mathcal{E} = \frac{dN(\mathcal{E})}{d\Omega d\mathcal{E}} \cdot \pi\sigma_{x'}\sigma_{y'} \cdot 0.01\mathcal{E} \ . \tag{4.2}$$

For the momentum spectrum a unit conversion is required yielding the relation

$$N(p) = \frac{dN(\mathcal{E})}{d\Omega d\mathcal{E}} \cdot \Delta\Omega \cdot \frac{d\mathcal{E}}{dp} = \frac{dN(\mathcal{E})}{d\Omega 0.01} \cdot \pi\sigma_{x'}\sigma_{y'} \cdot \frac{1}{\mathcal{E}}\frac{d\mathcal{E}}{dp} \tag{4.3}$$

with the differential

$$\left(\mathcal{E}\frac{dp}{d\mathcal{E}}\right)^{-1} = \sqrt{\frac{\epsilon+2}{\epsilon}}\frac{1}{(\epsilon+1)mc} \tag{4.4}$$

where $\epsilon = \frac{\mathcal{E}}{mc^2}$.

Using the energy or momentum resolution one can also calculate the bunch size in the focal plane in both dimensions x and y for a discrete set of proton momenta or energies. These are the functions $\sigma_x(p)$ and $\sigma_y(p)$ that are required for calculation of the fluence. For fixed drift lengths defined by the design energy, a system matrix is computed for every momentum of the discretized spectrum. Then the same initial sigma matrix is multiplied according to Eq. 3.31 with the system matrix. The resulting matrices contain the bunch size for every momentum after propagation through the system, i.e. in this case in the focal plane,

$$\sigma_x = \sqrt{\sigma_{11}} \tag{4.5}$$

$$\sigma_y = \sqrt{\sigma_{33}} \tag{4.6}$$

where σ_{ij} corresponds to the matrix element of the 4×4 σ-matrix Eq. 3.7 (no misalignment, i.e. transverse offsets are assumed). In Fig. 4.16 the bunch size is plotted as function of energy. The energy steps were chosen according to the determined energy resolution within the range of the measured proton energies. In this example, the drift lengths in the setup were calculated for 12 MeV design energy. This fits with the position of the minimum beam size. On closer inspection of Fig. 4.16b it becomes apparent that in both dimensions the minimum spot size is at a slightly different energy values than the design energy. This small shift represents the detuning δ introduced in Sec. 3.4 and results from numerical limits in the drift length calculation. Mathematically, there is

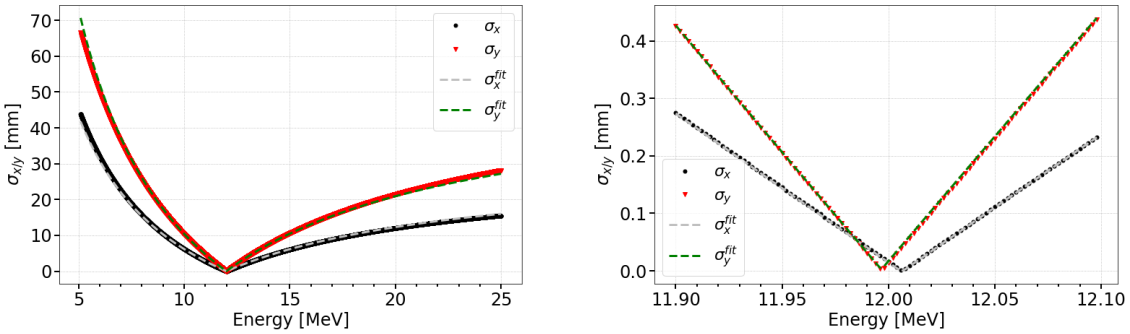

(a) (b)

Figure 4.16.: Bunch size in the focal plane as function of proton energy with the fits of Eq. 3.70. (a): Size over the whole spectrum. (b): Zoom into the energy range around the design energy

no reason that prevents $p_{0x} = p_{0y}$. The remaining δ is very small and on the order of the energy resolution. Therefore, it determines the numerical accuracy of the design energy. Fig. 4.16 shows also the fits of Eq. 3.70 to the calculated bunch sizes as a function of momentum. The fit was performed independently in both dimensions in the range $p_0 \pm 0.1 p_0$ to secure a good description in the spectral range most relevant for the focus. It shows that Eq. 3.70 reproduces well the relationship between bunch size and momentum obtained from the matrix calculation and yields the design momenta $p_{0x} = 12.006\,\mathrm{MeV}$ and $p_{0y} = 11.997\,\mathrm{MeV}$ resulting in a numerical accuracy of 9 keV and a $\delta = 4.5\,\mathrm{keV}$. Further, the fit allows to determine the scaling parameters $a_x^0(p_{0x}) = (28.57 \pm 0.01)\,\mathrm{mm}$ and $a_y^0(p_{0y}) = (51.91 \pm 0.01)\,\mathrm{mm}$ for in this case 12 MeV design energy, as they are free fit parameters. The errors were estimated by averaging fit results of fitting $\sigma_{x/y}\,(p \pm \delta)$ over p.

Having calculated both spectrum and bunch size per momentum on the same set of momenta, it is possible to perform a numerical integration of Eq. 3.57 via the trapezoidal method. Therefore, the initial spatial particle distribution generated at the source $N(x, y, p)$ remains to be assumed. In Sec. 3.4 we considered two cases, the Gaussian distribution Eq. 3.59 and the flat elliptic distribution Eq. 3.63 which both will be used for the calculations as they can be regarded as extreme cases of the real distribution, which is unknown. The discrete 2D fluence distribution in the focal plane is calculated with a spatial resolution corresponding to the pixel size of the image of the scintillation screen, i.e. 15 µm.

Fig. 4.17 displays the results of exemplary fluence calculations. Fig. 4.17a shows the

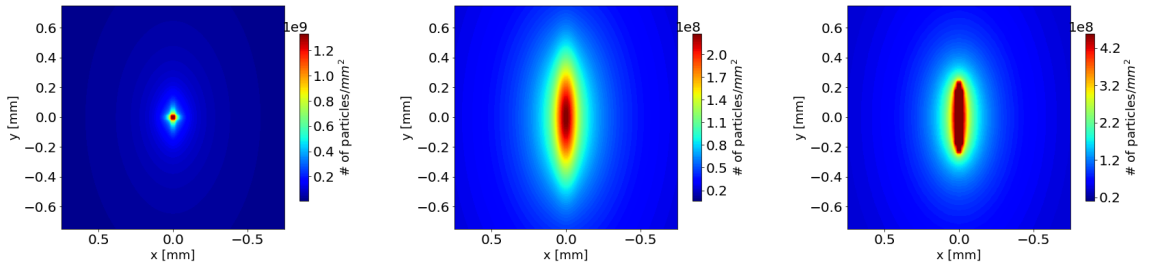

(a) Point source (b) Gauss distribution (c) Flat top distribution

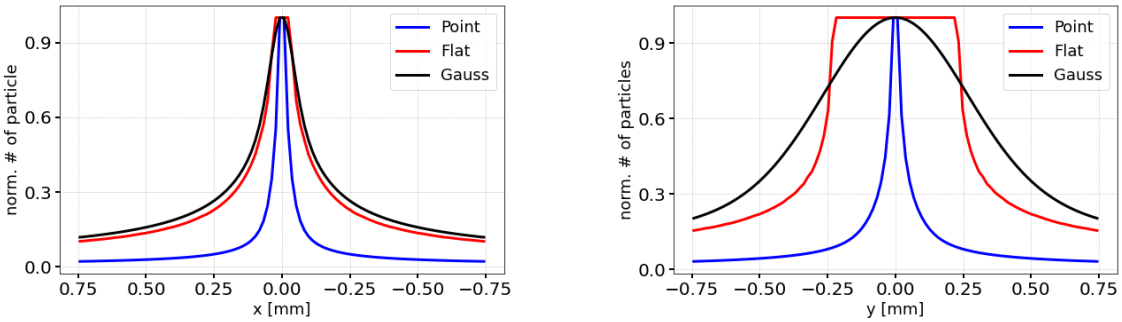

(d) Lineouts along x at $y = 0$ (e) Lineouts along y at $x = 0$

Figure 4.17.: Calculation of fluence profile in the focal plane for different source distributions for 12 MeV design energy. (a) Point source ($\sigma_x^s = \sigma_y^s = 0$) with Gaussian distribution in focal plane. (b) Extended source ($\sigma_x^s = \sigma_y^s = 5\,\mu\text{m}$) with Gaussian distribution in focal plane. (c) Extended source ($\sigma_x^s = \sigma_y^s = 5\,\mu\text{m}$) with flat elliptical distribution in focal plane. Lineouts in (d) x and (e) y direction through the center of the calculated fluence distribution.

obtained beam profile in beams eye view for a 12 MeV design setup and a point source modeled with the Gaussian distribution using $\sigma_x^s = \sigma_y^s = 0$. One can see that despite the infinitely small source the profile exhibits a finite size due to contributions from not perfectly focused particles with momenta different from the design. Due to the restriction of the divergence to the acceptance the spot is almost round. Only the background shows ellipses elongated along the FODO direction. However, the round shape is lost as soon as an extended source is used as shown in Fig. 4.17b which was calculated with $\sigma_{x/y}^s = 5\,\mu\text{m}$ and a Gaussian distribution. Here, the elongation of the focus in the FODO dimension y compared to the point source is clear. Also the maximum fluence drops approximately by a factor of 10 compared to the point source as the particles get distributed over a larger area. Maintaining the source size but changing the distribution to flat elliptical yields the fluence distribution as shown in Fig. 4.17c with sharper edges and a homogenous

maximum fluence area that reflects the sharp edges of the initial distribution. The fluence values are a factor 2 higher than in the Gaussian case.

The differences between the three calculated shapes becomes more apparent when comparing the normalized lineouts through the center of the images (Fig. 4.17d and 4.17e). A clear difference between the point source and the extended source is visible especially in the y dimension where the magnification is larger. While the point source results in a lineout with a FWHM $y_{point}^{FWHM} = 60\,\mu m$, the 5 µm small source causes significantly broader curves for the different distributions[2] ($y_{Gauss}^{FWHM} = 750\,\mu m$, $y_{flat}^{FWHM} = 540\,\mu m$). The Gaussian distribution yields a 39% larger spot size than the elliptical flat top distribution. The narrower FWHM of the flat distribution results from the sharp edges which are smeared out and broadened when transiting to the Gaussian case. As these two cases can be regarded as extreme cases of real distributions, it is feasible that measured lineouts will adopt intermediate shapes and in any case be clearly distinguishable from the case of a point source by analyzing the lineouts. For the x dimension the difference between the two distribution functions is less pronounced, the effect of the finite source size is still very obvious. $x_{point}^{FWHM} = 60\,\mu m$ compares to $x_{Gauss}^{FWHM} = 210\,\mu m$ and $x_{flat}^{FWHM} = 180\,\mu m$. Here, the Gaussian width is 17% larger than the flat top one.

Both investigated cases yield comparable lineouts with similar shapes, maximum fluence and FWHM. Therefore, the resolution limit for the source size is determined by the minimum size of an extended source to result in the same lineout in the x dimension as the point source. For the Gaussian distribution this comparison is shown in Fig. 4.18. For this setup the limit was determined to be 0.2 µm for Gaussian and 0.3 µm for flat top input distributions. These observations lead to the conclusion that the lineouts are reasonable measures for the fluence distribution as they reflect both the initial spatial distribution and the source size with a resolution smaller than the minimum plausible source size which is the laser focus diameter of 4.6 µm.

Based on a comparison to the source size, the magnification of the 12 MeV setup can be calculated. The source size σ_x^s is converted into a FWHM via

$$x^{FWHM} = 2\sqrt{2\ln(2)}\sigma_x$$

and put in relation to the FWHM of the calculated lineouts x_{Gauss}^{FWHM} yielding a total spot size increase of 18 times in DOFO dimension. Analogously in y (FODO) dimension, it results in 64 times greater spot size. Since every proton energy interval is magnified by a

[2] Using the flat elliptical distribution for the point source calculation leads to narrower fluence distributions with $x_{point}^{FWHM} = y_{point}^{FWHM} = 30\,\mu m$.

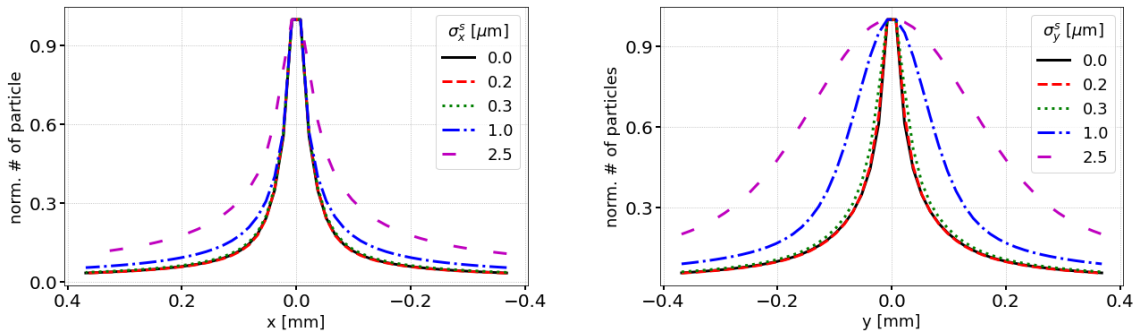

(a) Lineout along $y = 0$

(b) Lineout along $x = 0$

Figure 4.18.: Estimation of the resolution limit of the fluence distribution from the numerically integrated Gaussian distribution. Comparison of lineouts for different source sizes with the point source $\sigma^s_{x/y} = 0$.

different factor and therefore the total magnification of the source size is in principle a combination of all these different magnifications, this ratio integrates the contributions of the individual sizes of every $\sigma_{x/y}(p)$.

A better quantity to indicate the system magnification is the magnification of the design momentum bunch size retrieved from the elements of the system matrix $M_{sys}(p_0)$ according to Eq. 3.37. This magnification is independent of the initial particle distribution and a better estimate of the magnification around the high fluence area, crucial for relating the focus to the source size. Fig. 4.19 illustrates the matrix elements $V_x(p) = M_{sys,11}(p)$ and $V_y(p) = M_{sys,44}(p)$ for the 12 MeV design energy setup. Since an imaging of the source happens only for particles of the design energy, only $V_x(p_0)$ and $V_y(p_0)$ represent actual magnifications according to the lens equation Eq. 3.36. This is why it is possible that V_x, $V_y < 0$ for $p > p_0$. However, the deviation from the imaging condition is small for the energy interval around the design energy, which contributes most to the fluence in the focus. Therefore, $V_x(p_0)$ and $V_y(p_0)$ represent a meaningful approximation value for an overall magnification in the most relevant part of the spectrum within $p_0 \pm 0.25 p_0$. As uncertainty for the magnification one can compute the standard deviation in this interval. In the present example the magnification yields $V_x(p_0) = 7 \pm 3$ and $V_y(p_0) = 47 \pm 5$. Note that the magnification is larger in the direction where the stronger magnet focuses, probably partly due to the asymmetric acceptance.

For a more accurate reproduction of the effect of the finite bore and the elliptical aperture on the fluence distribution in the focal plane, the matrix formalism was used to implement a Monte Carlo like individual particle tracking code that discarded particles

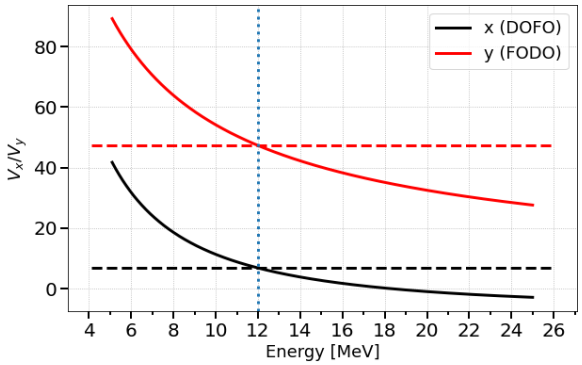

Figure 4.19.: V_x and V_y as function of energy for a 12 MeV design energy setup obtained from $M_{sys}(p)$. The dotted line indicated the design energy and the dashed lines the magnification of the design energy $V_x(p_0)$ and $V_y(p_0)$.

whose trajectories extended further than the bore diameter of the magnets. The particles were randomly assigned with starting positions within a 5 µm radius around the central axis. This resembles the elliptical flat top distribution. In order to reduce computational efforts the random divergence angles were limited to the range between the angles x'_{ap} and y'_{ap} determined by the aperture and the first drift length. The simulation was performed with a script in *Wolfram Mathematica® 11.0* and was limited by RAM to 50,000 particles per energy bin. Therefore, to obtain a significant result the energy interval for the simulation had to be limited to a design energy dependent interval around the design energy with 20 keV resolution based on the energy selectivity of the doublet. The spectrum was assumed exponentially decaying and the relation between particle numbers per energy extracted from the spectrum used for the previous calculations (Fig. 4.15).

The results for a simulation of one 12 MeV and one 22 MeV design energy setup are shown in Fig. 4.20. The a particle spectra were simulated in intervals of 10 to 14 MeV (3.8 million particles) and 18 to 26 MeV (13.9 million particles). Although, the tracking considers a much narrower bandwidth of particle energies it is expected to reproduce well the focal fluence distribution as particles with energies outside the simulated interval will contribute mostly at the background level. The obtained fluence distributions and lineouts yield $x^{FWHM}_{tracked} = 120\,\mu m$ (Fig. 4.20c) and $y^{FWHM}_{tracked} = 435\,\mu m$ (Fig. 4.20e) for 12 MeV. For the 22 MeV the tracking results $x^{FWHM}_{tracked} = 105\,\mu m$ and $y^{FWHM}_{tracked} = 345\,\mu m$ compare to the results of a 22 MeV calculation, $x^{FWHM}_{flat} = 120\,\mu m$, $y^{FWHM}_{flat} = 390\,\mu m$ and $x^{FWHM}_{Gauss} = 150\,\mu m$, $y^{FWHM}_{Gauss} = 540\,\mu m$. The shapes resemble strongly a combination of the distributions obtained for the flat and Gaussian source distribution although this

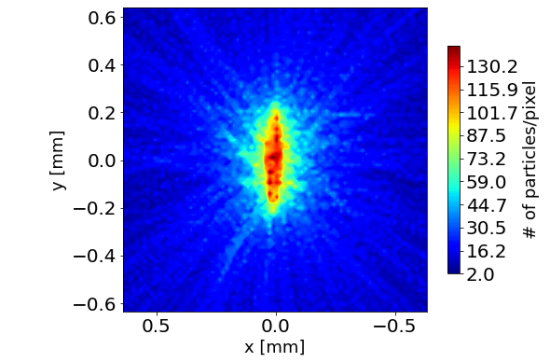

(a) Tracked beam profile 12 MeV

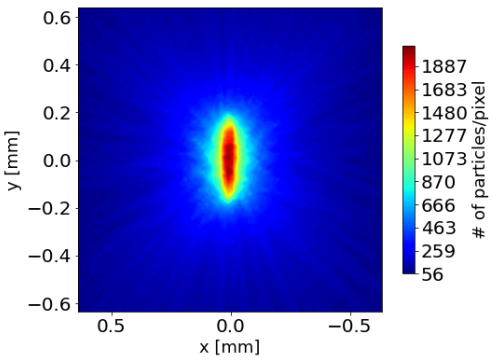

(b) Tracked beam profile 22 MeV

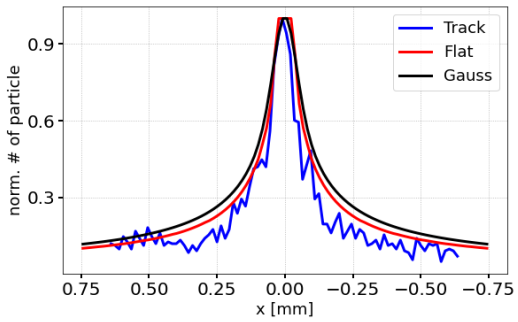

(c) DOFO 12 MeV

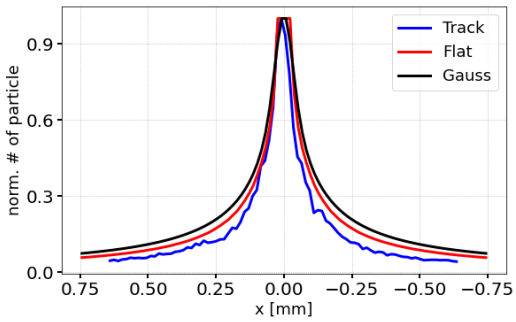

(d) DOFO 22 MeV

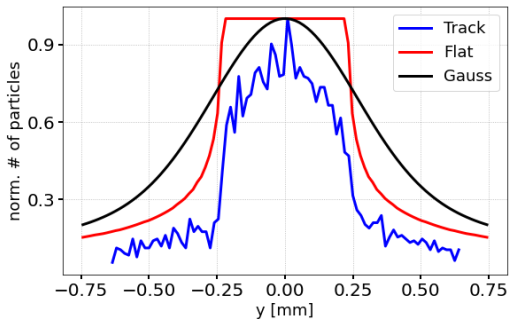

(e) FODO 12 MeV

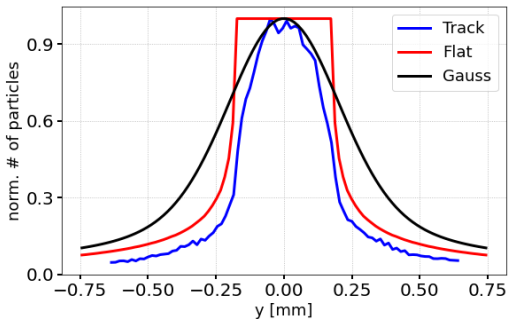

(f) FODO 22 MeV

Figure 4.20.: Results of particle tracking through a 12 MeV (a), (c), (e) and 22 MeV (b), (d), (f) design energy setup. Fluence distribution in focal plane and the lineouts through the image center. For comparison the calculated lineouts for extended sources from Fig. 4.17 are shown again.

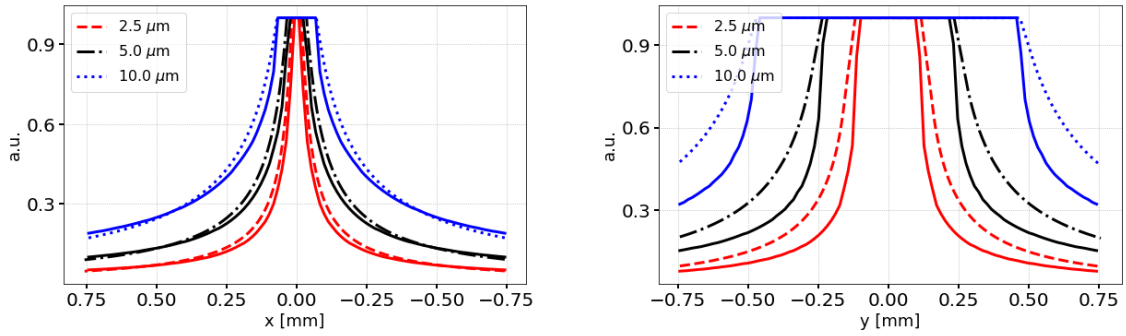

Figure 4.21.: Comparison of the numerically integrated distribution lineouts with 2.5 µm, 5 µm and 10 µm source size $\sigma^s_{x/y}$ (solid lines) in (a) x and (b) y dimension to the analytical model lineouts calculated for the same source sizes at 12 MeV design energy and $\delta = 4.5$ keV.

might be a consequence of still lacking statistics. Due to the definition of the input source, the distribution of the elliptical flat source distribution would be expected to emerge as result from the particle tracking. Nevertheless, the results already are enough to evaluate the effect of absorption in the magnets and compare it to the calculations with the adapted divergence. The chosen constraints for the divergence angles seem to represent the effect of the limited bore but underestimate its magnitude slightly. For 12 MeV design energy the FWHM of the calculated lineouts from the flat top distribution is 24% (FODO) and 50% (DOFO) greater than the tracking results width. At 22 MeV design energy the width of the lineouts is narrower and the results for calculation and tracking approach each other. Here, the calculation overestimated the FWHM by 13% (FODO) and 14% (DOFO). One can conclude that the higher the design energy the less the error is made by tailoring the initial bunch divergence. For the investigated design energy range one can expect that the widths agree enough to accept the divergence reduction as meaningful measure to represent the effect of the limited magnet bore.

In Sec. 3.4 it was shown that it is possible to calculate the lineouts using an analytical model. To validate this model it was compared to the numerically calculated lineouts. As the model relies on the assumption of flat elliptical distributions it is expected to agree better with the numerical fluence calculations based on the same distribution instead of the Gaussian distribution. Fig. 4.21 shows the lineouts in both dimensions obtained with the analytical model when using the above obtained values for the design momentum magnification $V_{x/y}(p_0)$ as well as the values from Fig. 4.16 for δ and scaling parameters

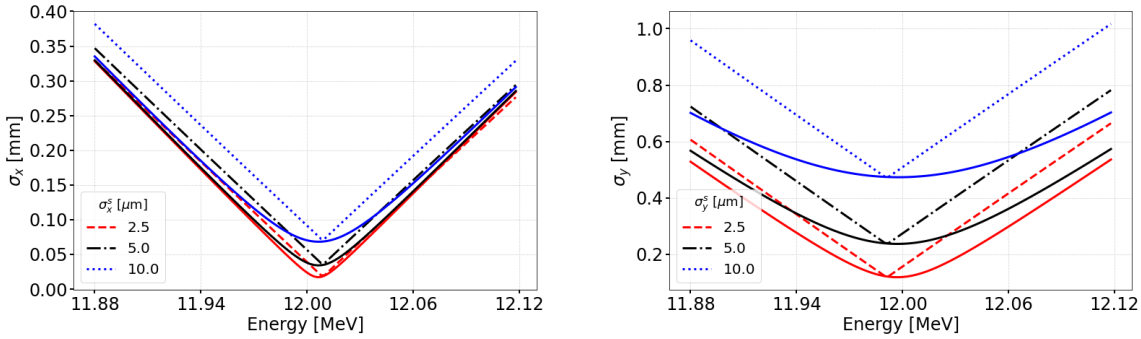

(a) (b)

Figure 4.22.: Bunch sizes in the focal plane as function of momentum (solid lines) compared to the curve of Eq. 3.70 (structured lines) calculated with the scaling parameters obtained for the point source around the design energy 12 MeV for different source sizes $\sigma^s_{x/y}$.

$a_{x/y}(p_0)$ to derive the normalized minimum spot size in the focal plane

$$\sigma'_{x0/y0} = \frac{\sigma^s_{x/y}}{a_{x/y}(p_0)} V_{x/y}(p_0) \tag{4.7}$$

and to scale the results of the model. The 5 µm source size used in the completely numeric approach yielded $x^{FWHM}_{flat} = 180\,\mu m$ and $y^{FWHM}_{flat} = 540\,\mu m$. The same source size applied to the analytic model results in a broader width of the lineouts $x^{FWHM}_{analytic} = 210\,\mu m$ and $y^{FWHM}_{analytic} = 728\,\mu m$. Also for smaller and larger source sizes the analytic model returns broader lineouts. The ratio between analytic and numeric FWHM is in all cases between 1.1 and 1.4 and averages to 1.3 over all considered source sizes.

The reason for this difference becomes clear when looking at Fig. 4.22 and comparing the bunch sizes in the focal plane as function of momentum $\sigma_{x/y}(p)$ calculated in the numerical model (solid lines) and the curves of Eq. 3.70 (structured lines) which were calculated with the scaling parameters $a_{x/y}(p_0)$, δ and the magnification $V_{x/y}(p_0)$.

One can see, that the analytic model agrees with the numeric model in the minimum spot size leading to the same width of the plateaus in Fig. 4.21. Also the detuning obtained based on the point source reproduces the minimum position of the wrist only within the error margins of the detuning. However, the wrist of $\sigma_{x/y}(p)$ caused by the extended source size is not well represented. The analytic model overestimates the bunch size for all other energies. Therefore, the integral over $\sigma_{x/y}(p)$ will be larger leading to a mismatch in the lineout slopes and broader lineout in Fig. 4.21 caused by the uncertainty

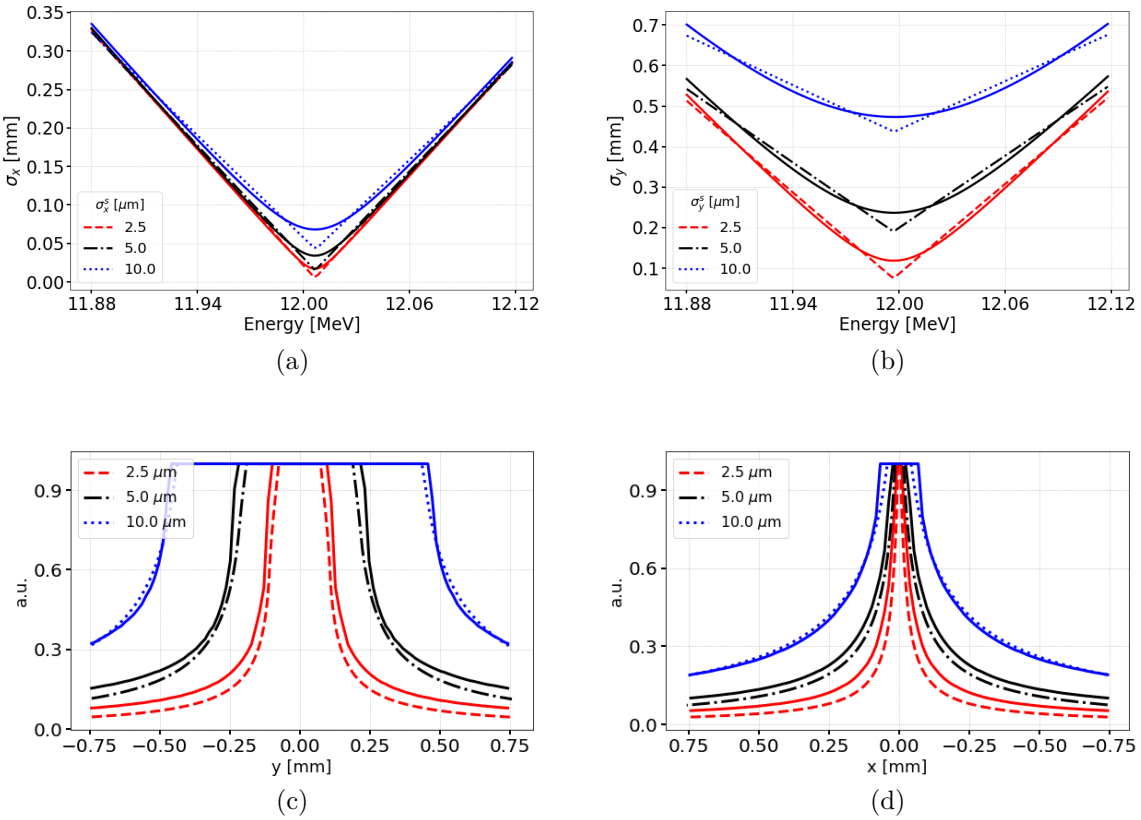

Figure 4.23.: Bunch sizes in the focal plane as function of momentum (solid lines) compared to fits of Eq. 3.70 around the design energy 12 MeV for different source sizes $\sigma^s_{x/y}$ in (a) in x and (b) in y. With the fit parameters calculated lineouts in (c) in x and (d).

of the scaling parameters $a_{x/y}$ and the magnification $V_{x/y}$.

The minimum spot size is determined only by the source size and the magnification ($a_{x/y}$ cancel out). The slope of Eq. 3.70 is given by the scaling parameters $a_{x/y}$. Thus, Fig. 4.22 suggest that the parameters obtained from a fit to the $\sigma_{x/y}(p)$ of a point source lead to too broad lineouts when applied to calculate the case of source sizes greater than zero.

To estimate the uncertainty of $a_{x/y}$ a fit of Eq. 3.70 to each numerically calculated $\sigma_{x/y}(p)$ is performed in Fig. 4.23a and Fig. 4.23b. It yields a tradeoff between representing well the minimum spot size and the slope of $\sigma_{x/y}(p)$. The ratio between the fit results and the point source value $\frac{a^{fit}_{x/y}}{a^0_{x/y}}$ is between 1.05 and 0.92 in x dimension and between 0.85 and 0.46 in y dimension decreasing with increasing source size. It shows that the scaling factors for the point source are on the upper limit of the scaling parameters.

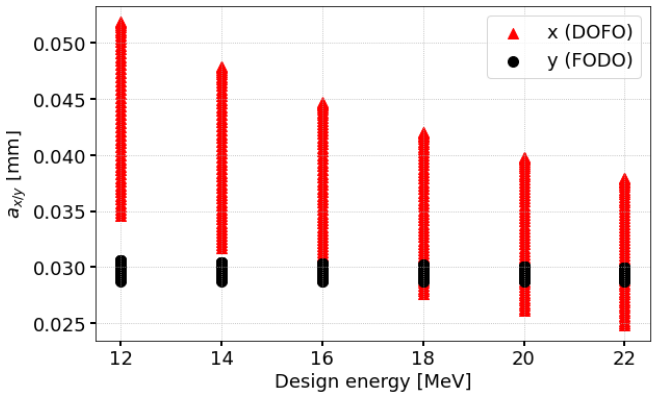

Figure 4.24.: Scaling factors $a_{x/y}$ obtained from fits of Eq. 3.70 to the numerically calculated functions $\sigma_{x/y}(p)$ for source sizes between 0 and 50 µm.

Fig. 4.24 shows the scaling factors obtained of fits of Eq. 3.70 for source size values between 0 and 50 µm and at different design energies. One can see how the average value decreases for higher design energies. The relative spread however is approximately constant with a ratio of standard deviation to mean of $\frac{\Delta a_x}{a_x} = 0.02$ and $\frac{\Delta a_y}{a_y} = 0.13$ giving an estimate for the uncertainty of the scaling factors.

The fit underestimates the minimum spot size $\sigma_{x0} = \sigma_x^s V_x^{fit}$. It leads to a smaller plateau in the calculated lineouts in Fig. 4.23c and Fig. 4.23d and an underestimation of their widths. The magnification $V_{x/y}^{fit}$ retrieved from σ_{x0} is therefore smaller than $V_{x/y}$ as determined from the system matrix. The ratio $\frac{V_{x/y}^{fit}}{V_{x/y}}$ increases from 0.3 to 0.6 in x and 0.6 to 0.9 in y for larger source sizes. This ratio has special meaning when trying to calculate the source size $\sigma_{x/y}^s$ from the fitted minimum spot size $\sigma_{x0/y0}$. Using $V_{x/y}$ instead of $V_{x/y}^{fit}$ leads to an underestimation of the source size. This holds also after the integration of $\sigma_{x/y}(p)$ and is relevant when retrieving the source size by fitting the analytic model to the numeric lineouts using as free fit parameters δ', σ'_{x0} and σ'_{y0} as well as an additional scaling value A and and offset *off*.

Fig. 4.25 shows the result of a the model fitted simultaneously in both dimensions to numerical calculated lineouts from source sizes $\sigma_x^s = \sigma_y^s = 5$ µm, $\sigma_x^s = \sigma_y^s = 10$ µm and $\sigma_x^s = \sigma_y^s = 50$ µm for a 12 MeV design energy setup. Due to the unequal differences between the modeled and calculated $\sigma_{x,y}(p)$ in the two dimensions (Fig. 4.22), the combined fitting leads to a slightly corrupted but nevertheless sufficient agreement of the fits with the numerical lineouts. The values indicated in every plot of the figure are the rescaled fitting parameters. The fitted source size σ_x^{fit} and σ_y^{fit} were calculated according

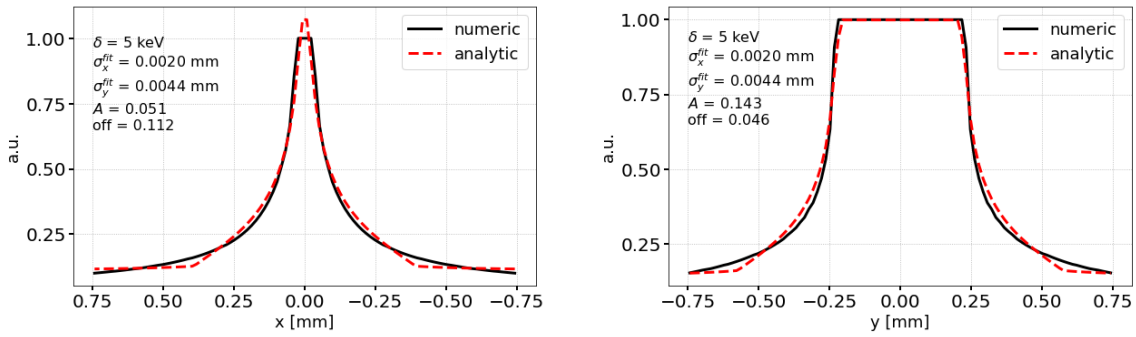

(a) 5 µm

(b) 5 µm

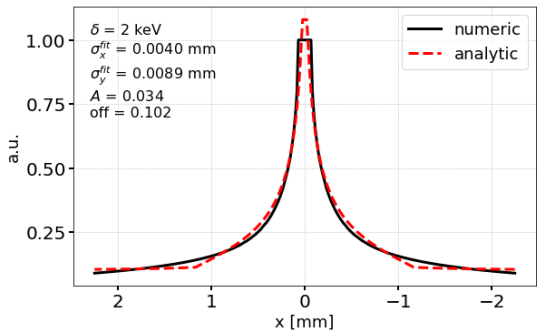

(c) 10 µm

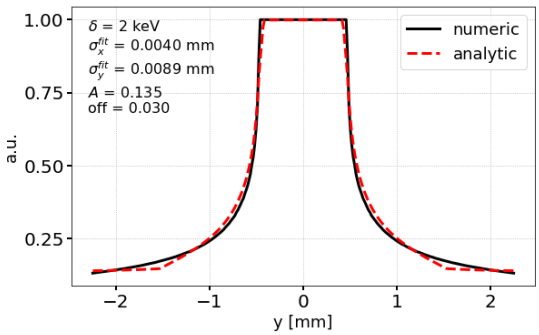

(d) 10 µm

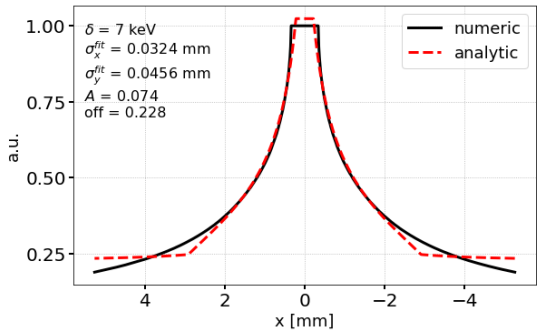

(e) 50 µm

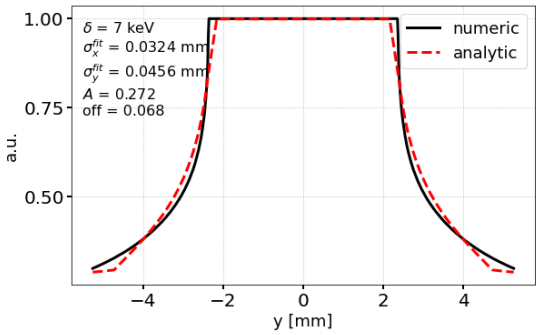

(f) 50 µm

Figure 4.25.: Fit of the analytical model to the numerically calculated lineouts for (a), (b) $\sigma_x^s = \sigma_y^s = 5\,\mu\text{m}$, (c), (d) $\sigma_x^s = \sigma_y^s = 10\,\mu\text{m}$ and (e), (f) $\sigma_x^s = \sigma_y^s = 50\,\mu\text{m}$ at 12 MeV design energy.

to the rearranged Eq. 4.7 from the minimum spot sizes σ'_{x0} and σ'_{y0} using the average scaling factors $a_x(p_0)$, $a_y(p_0)$ and magnifications $V_x(p_0)$, $V_y(p_0)$. One has to note that the choice of $a_x(p_0)$ and $a_y(p_0)$ is somewhat arbitrary since they are also used to scale the data prior to the fit and therefore cancel out when scaling back the parameters in the source size calculation. As shown above, the source size relates to the minimum spot size only via the magnification. Therefore, a reasonably close estimate for the scaling factors is enough to not disrupt the result.

The detuning δ has the expected order of magnitude and varies for the three source sizes within the error margin. The retrieved source size is always smaller than the one actually used for the forward calculation which is the effect of $\frac{V^{fit}_{x/y}}{V_{x/y}} < 1$. Based on the comparison of the three different source size scenarios in a 10% smaller σ^s_y size is obtained from the fit. In other terms, the retrieved source size needs to be scaled with an correction factor $\kappa_y = (1.1 \pm 0.03)$. The error for σ^s_x is greater with the actual source size being larger than the retrieved one by factors $\kappa_5 = 2.5$, $\kappa_{10} = 2.5$ and $\kappa_{50} = 1.5$ for 5 µm, 10 µm and 50 µm respectively. This larger error is because the magnification is smaller in x resulting in smaller minimum spot size σ'_{x0} and less resolution of the fit for $x' < \sigma'_{x0}$. Hence, the error factor reduces for lager $\sigma^s_{x/y}$. Since the resolution of the calculated lineouts is the same as obtained for the experimental measured data, this leads to the conclusion that a conservatively estimated correction factor $\kappa_x = (2.0 \pm 0.5)$ for retrieved σ^s_x is a reasonable estimate. With this correction factors the source size in both dimensions can then be calculated by

$$\sigma^s_x = \kappa_x \sigma^{fit}_x = \kappa_x \frac{\sigma'_{x0}}{V_x} a_x, \quad \sigma^s_y = \kappa_y \sigma^{fit}_y = \kappa_y \frac{\sigma'_{y0}}{V_y} a_y \tag{4.8}$$

with an relative error that can estimated from the errors of the contributing quantities (analogously for y)

$$\frac{\Delta\sigma^s_x}{\sigma^s_x} = \sqrt{\left(\frac{\sigma'_{x0} a_x}{V_x}\Delta\kappa_x\right)^2 + \left(\frac{\kappa_x \sigma'_{x0}}{V_x}\Delta a_x\right)^2 + \left(\frac{\kappa_x a_x \sigma'_{x0}}{V_x^2}\Delta V_x\right)^2 + \left(\frac{\kappa_x a_x}{V_x}\Delta\sigma'_{x0}\right)^2}. \tag{4.9}$$

In summary, in this section there have been developed and compared two methods to calculate the fluence distribution in the focal plane for a source of a given size and broad energy distribution. The first approach was a numerical integration of Eq. 3.57 with an exponential energy distribution, using two different assumptions for the spatial particle distribution in the focal plane, a Gaussian distribution and a flat elliptical distribution. This methods on the one hand yields a 2D fluence distribution and on the other hand

allows to investigate the influence of the distribution on the spot size in the focal plane by means of lineouts. It showed that a Gaussian distribution with the same source size causes a 38% larger FWHM in the focal plane. Further, it is possible to resolve differences in the fluence lineouts coming from sub micrometer changes in the source size.

The second method relied on the analytical model introduced in Sec. 3.4 which is based on the assumption of a flat elliptical fluence distribution in the focal plane. It can only reproduce the lineouts through the fluence distribution in both dimensions x and y. The model requires scaling parameters $a_x(p_0)$, $a_y(p_0)$ and magnifications $V_x(p_0)$, $V_y(p_0)$ that had to be identified through comparison to the numerical model. Finally, correction factors κ_x, κ_y account for the wrist of $\sigma_x(p)$ and $\sigma_y(p)$ around the design energy. This method does not only allow to forward calculate the fluence distribution from a given source, but it can also be used as a fit model to any calculated or measured fluence lineout. With the fit parameters it is then possible to find an estimate for the source size that produced the measured lineout using the minimum spot size in the focal plane (Eq. 4.8). Therefore, this model is useful for the automated analysis of measurement data. The errors of the retrieved source size can be estimated according to Eq. 4.9. But as the model is based on a flat distribution the retrieved results could overestimate the actual source size by up to 38% if the distribution was in fact Gaussian.

4.7. Doublet Spectrum Calculation

Based on the assumptions for $N(x, y, p)$ and the calculations of $\sigma_{x/y}(p)$ it is also possible to numerically integrate Eq. 3.60 with the Gaussian spatial distribution. The integration limits for x and y have crucial influence on the result because the larger the area over which $N(x, y, p)$ is integrated, the stronger the resemblance to the input spectrum shown in Fig. 4.15.

Fig. 4.26 displays spectra for three different radii $r = \sqrt{x^2 + y^2}$ of a fictive aperture in the image plane determining the integration limits for two different design energy setups. The larger the radius the higher the particle numbers and the stronger the contribution from lower energies. This is due to the fact, that protons of lower energies are spread over a larger area by the doublet so they enter in the integration domain only at larger distance to the center. Integrating over a small area around the center yields a spectrum peaked around the design energy. One can see that the peak positions shift to different energies when increasing the radius of the virtual aperture. In the 12 MeV design energy case the actual peak shifts from 12 MeV at 0.5 mm to 11.7 MeV at 2.5 mm radius. Also

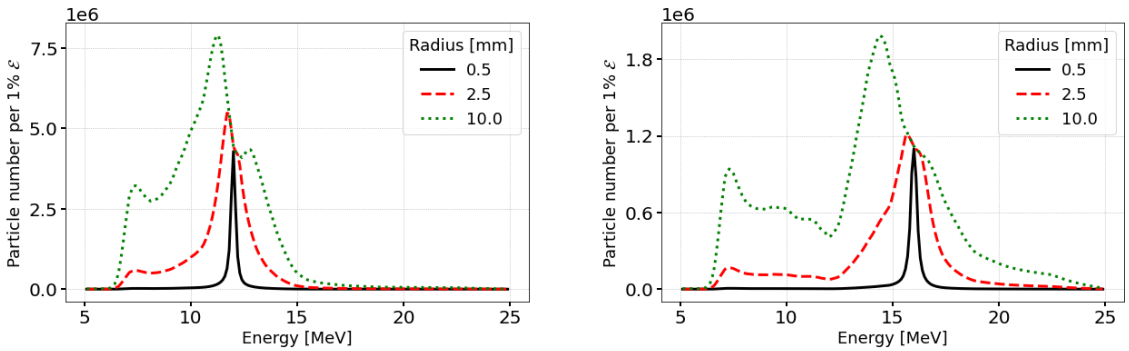

(a) 12 MeV (b) 16 MeV

Figure 4.26.: Calculated spectra in focus of different radii for a 12 MeV and 16 MeV design energy setup.

the FWHM of the peaks increase from 0.2 MeV to 1.2 MeV for increasing radius resulting in a relative spread $\frac{\Delta\mathcal{E}}{\mathcal{E}}$ that increases from 2% to 10%. At 1 cm aperture the peak position is shifted to 11.2 MeV and has a relative spread of 50%. For 16 MeV design energy peak shifts significantly from 16 MeV to 15.7 MeV to 14.4 MeV as the radius increases from 0.5 mm to 1 cm. However, the relative energy spread stays comparable to the 12 MeV spectra at 1% and 13% for 0.5 mm and 2.5 mm integration radius.

The calculated spectra can be transformed into a correlation of energy loss as a function of depth in a determined material (Bragg curve). This depth profile relates to the deposition of energy, i.e. dose, in the material which is of interest for any application

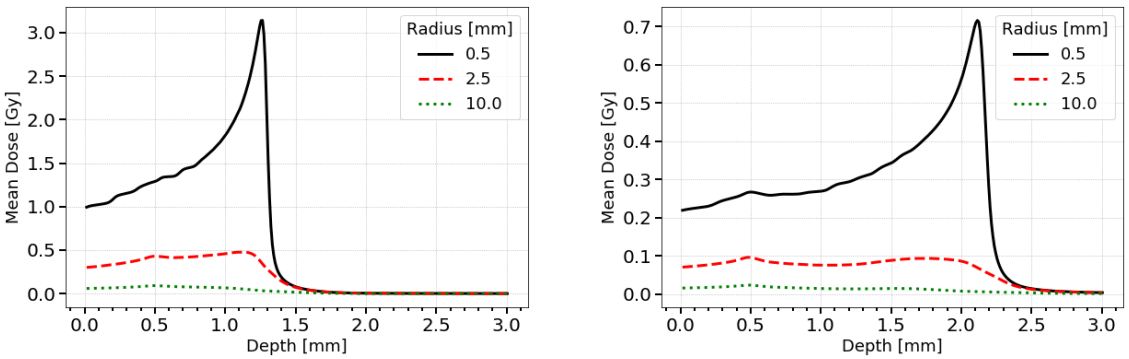

(a) 12 MeV (b) 16 MeV

Figure 4.27.: Bragg curves reconstructed from the calculated spectra in focus with different radii for a 12 MeV and 16 MeV design energy setup. Dose averaged over the area of the fictive aperture.

experiment and was measured with stacks of RCFs (EBT3). As EBT3 is mainly ($\approx 90\%$) made of polyester, polyethylene terephthalate (PET) was assumed as material for the energy loss calculations. The stopping power of protons in PET as a function of energy was determined using range tables from SRIM. The energy distribution from Fig. 4.26 then results in the depth curves in Fig. 4.27 of the dose averaged over the aperture area.

As expected the curves yield a finite range of the protons in PET determined mainly by the highest proton energies of the spectrum. The higher the (design) energy the larger the penetration depth. One can see that the average dose reduces for a larger area as the dose values far away from the center are small and contribute little to the deposited dose. This is the case because the high particle numbers in the spectrum at energies far below the design energy appear only for large radii meaning that they are spread over a larger area. Therefore, the main dose contribution is coming from the spectral peak around the design energy.

5. Experimental Results

If one aims at achieving the minimal possible focal spot size with a polychromatic proton bunch it is important to assess what influences and limits the focal spot shape. These factors can be attributed to either one of the two fundamental parts of any transport setup: On the one hand the injected bunch which in this case is determined by the source and its emittance and on the other hand the beamline. For the LION beamline the geometric positions of the beamline elements determine the focus shape. For instance, possible uncertainties in the magnetic field gradients can be compensated by adjusting the drift lengths. This is one reason why despite of the drift lengths being computable with the matrix formalism it is still necessary to perform a parameter scan for the drifts. Also, the transverse positions of the magnets along the beamline can only be set with limited precision due to the fact that the magnetic axis of the PMQs is not perfectly aligned with the central axis of the bore. Only if the effects from geometric misalignment to the focus shape are minimized the contribution from the source emittance becomes dominant and measurable.

In this chapter the focus of the LION doublet will be experimentally investigated and be analyzed. In contrast to continuous or quasi-continuous beams from conventional accelerators, bunches from laser-driven acceleration are produced with a very low repetition rate. Also, there is typically a limited number of available targets, i.e. proton bunches per experiment. This imposes high constraints on an online beamline characterization and focus shape optimization since there are both a large number of free setup parameters and a large shot-to-shot variation of the bunch energy spectrum. Therefore, the optimization has to be made based on a small number of parameter scans for different design energies which leads to a certain uncertainty of the actual best focus. Based on these parameter studies and in combination with calculations the influence of different position parameters are assessed and the best focus determined. Subsequently, it shall be made the attempt to assess the source size by reproducing the measured shape with the derived model of the focusing setup.

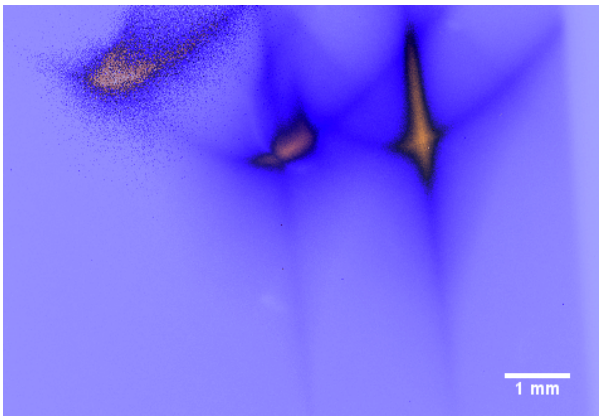

Figure 5.1.: Observation of Steering in x direction by intentional changes for 16 MeV design energy. Overlay of three consecutive shot images with both PMQs shifted by 250 µm between shots. Images were taken before focus optimization. (Contrast enhanced for better comparison, Shot IDs: 202105120046, 202105120047, 202105120048)

5.1. Transverse Offsets

The first online alignment step in the beamline setup was to produce a proton focus outside of the vacuum exit window. Due to the motorization of the setup it was possible to adjust the x position of both PMQs together such that transverse steering was minimized relative to the exit window center. This was done by changing the position online between shots and observe the immediate influence on the focus position via the scintillator and the camera (setup Fig. 4.14b). Fig. 5.1 shows an overlay of three consecutive shots where the doublet has been moved in positive x direction by (250 ± 10) µm in between shots (corresponding to a relative shift of the source in negative direction). The drift lengths were set to focus protons of 16 MeV design energy. The observed shift in the focus position was (2.5 ± 1.0) mm per step in the positive x direction.

To include the lateral offsets into the calculation of the fluence distribution the translation matrix 3.32 was used to calculate the steering of a single orbit particle as a function of momentum or energy representing the center of mass of the bunch in x and y. These position offset $x_{st}(p)$ and $y_{st}(p)$ were included in the calculation of the fluence distribution by shifting the Gaussian particle distributions in the fluence integrand in Eq. 3.57 accordingly for every momentum

$$N(x, y, p) = N(p) \exp\left(-\frac{(x - x_{st}(p))^2}{2\sigma_x^2(p)} - \frac{(y - y_{st}(p))^2}{2\sigma_y^2(p)}\right). \tag{5.1}$$

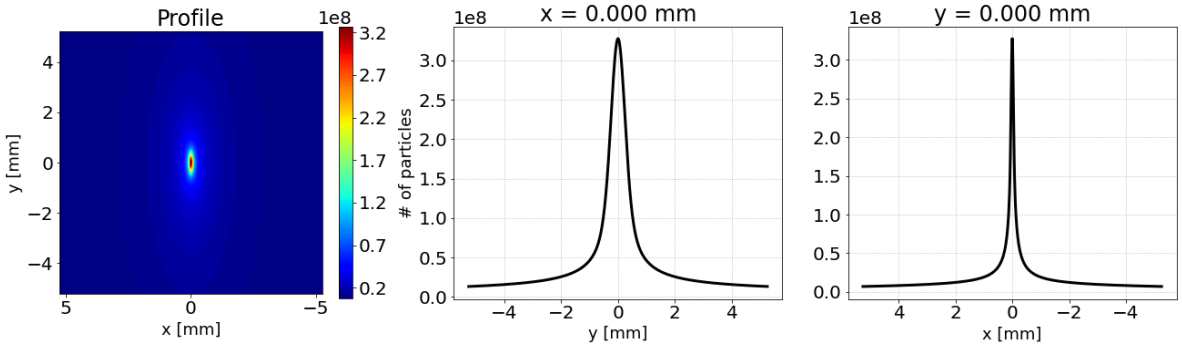

(a) No offset

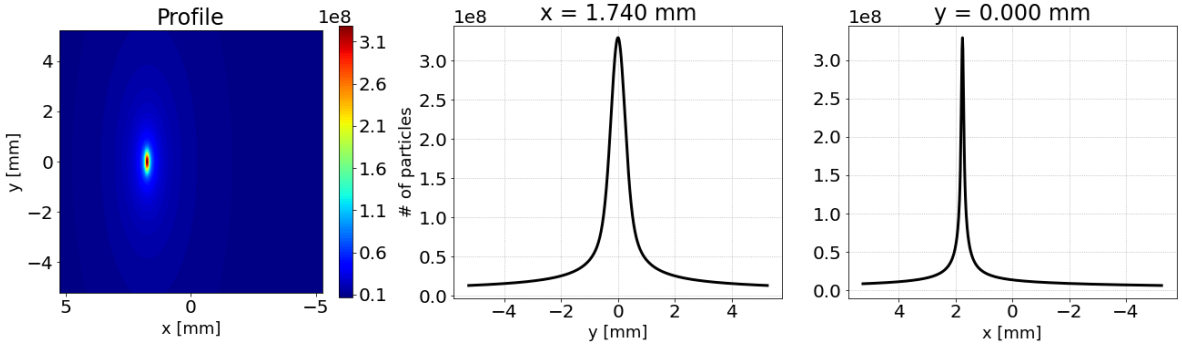

(b) 250 µm x offset both PMQs

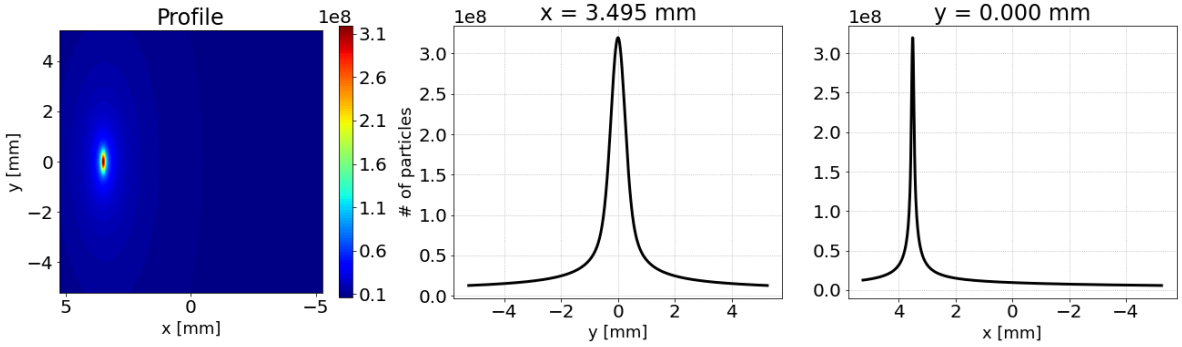

(c) 500 µm x offset both PMQs

Figure 5.2.: Calculation of steering due to lateral shift with 5 µm source size of a 16 MeV design energy setup.

The corresponding $\sigma_{x/y}(p)$ were calculated without any steering effects as the matrix formalism for the σ-matrix breaks down in this case. Also the bunch size per momentum is regarded unchanged by a weak dipole moment. Fig. 5.2 shows the calculated bunch profile from a source with 5 µm diameter emission area for the experimentally used parameters. In Fig. 5.2a the profile and lineouts of a bunch without any lateral offsets is shown. Shifting both PMQs together by 250 µm and 500 µm in x direction (Fig. 5.2b) produces a shift of the peak of 1.7 mm and 3.5 mm respectively which is in reasonable agreement with the experimentally measured shifts in Fig. 5.1. Also the correlation between PMQ displacement direction and steering direction is the same as experimentally observed. This allows the conclusion, that magnitude and direction of the steering can be reproduced by the model accurately.

Besides the shifting of the entire doublet there is still the possibility of relative offset between both PMQs remaining after the pre-alignment. Fig. 5.3a is an example of the effect of shifting only PMQ 1, i.e. the stronger magnet, by 250 µm in the x and 50 µm in the y dimension. This relative offset between the PMQs has a stronger effect than the combined shifting. According to the calculations the shift direction of the peak is inverted in x direction and both shifts increased compared to when both PMQs are misplaced together. Adding a different misplacement to PMQ 2 creates both an overall offset of the doublet from the source and a relative offset between both PMQs (Fig. 5.3c). For this case in x the steering from the relative offset adds to the previous steering in positive direction from an offset of both PMQs (Fig. 5.3b). Adding relative shift of less than half of the absolute shift more than doubles the overall focus shift indicating that in this dimension the relative offset has a stronger impact. The opposite relation is observed in the y dimension. Here, a relative offset that is double of the absolute offset creates the same amount of shift in the focus in the opposite direction. In this dimension the influence of the relative offset is weaker than the influence of the absolute offset. In both dimensions holds that, depending on the direction of the relative offset, it can increase or decrease the effect of the overall offset. Relevant for the direction of the overall steering is the larger of both effects. Especially in the DOFO dimension, the relative alignment of both magnets on one axis seems to be more relevant than the absolute alignment with respect to the source.

In summary, these observations mean that the lateral alignment of the setup is an important parameter that influences the focus position but does not contribute to the size and shape. Further, it shows that relative offsets can be compensated by absolute motion of both PMQs together without significant influence on the focus shape within

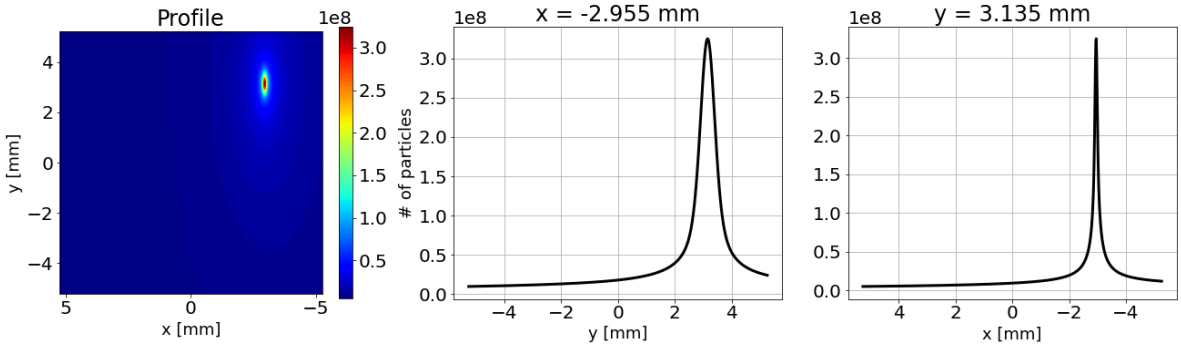

(a) Only PMQ 1

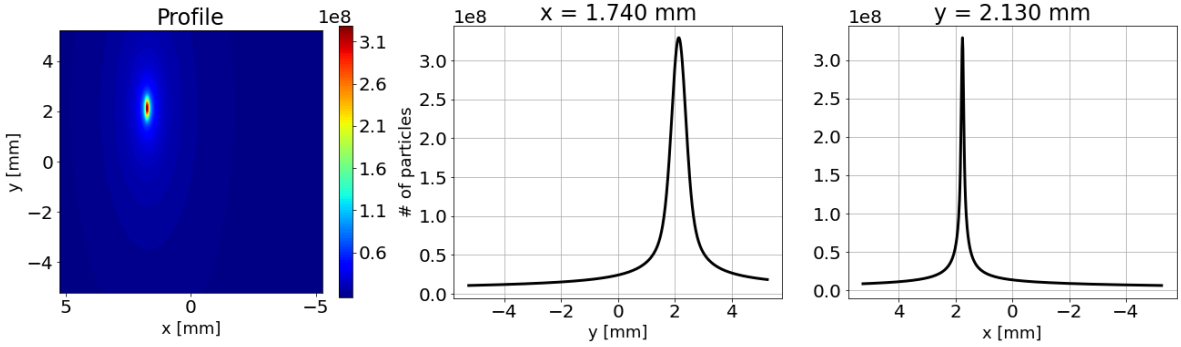

(b) Both PMQs, absolute offset

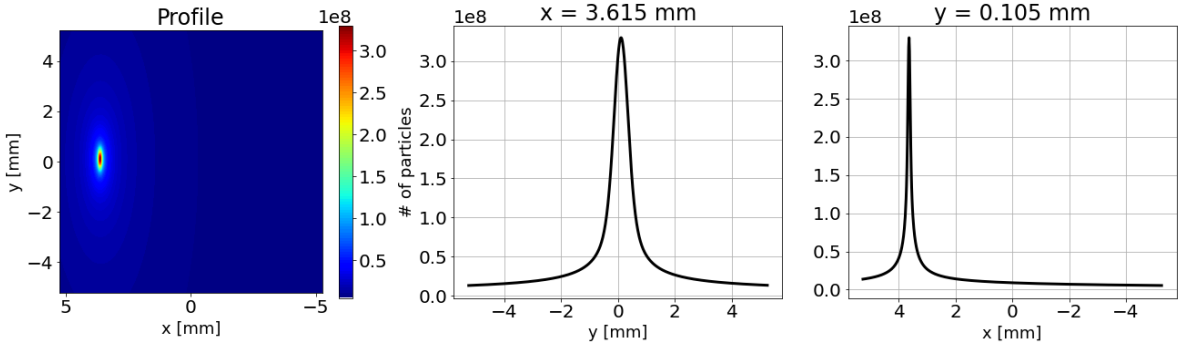

(c) Both PMQs, absolute and relative offset

Figure 5.3.: Example of beam profiles for different relative offsets for a 16 MeV design energy setup. (a) Only PMQ 1 was moved by 250 µm in x and 50 µm in y. (b) Both PMQs were moved together by 250 µm in x and 50 µm in y. (c) In addition to PMQ 1, PMQ 2 was moved by 350 µm in x and 150 µm in y creating both an overall offset of the setup from the source of 250 µm in x and 50 µm in y and a relative offset between the magnets of 100 µm in both dimensions.

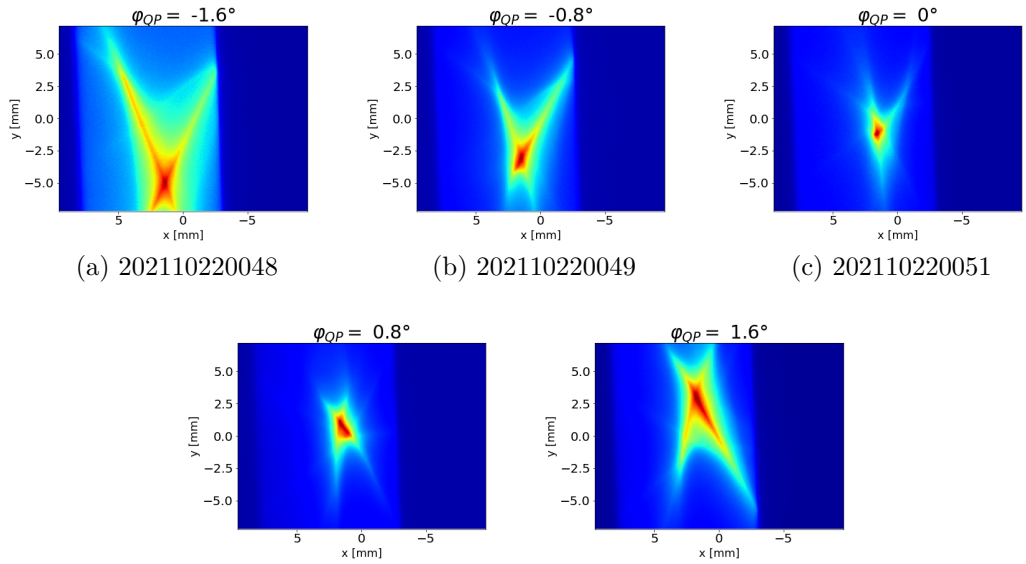

(a) 202110220048 (b) 202110220049 (c) 202110220051

(d) 202110220052 (e) 202110220053

Figure 5.4.: Measured bunch profiles for different rotation angles φ_{QP} of PMQ 1 with respect to the pre-aligned setting for a 12 MeV design energy setup. Every image is normalized to its maximum. The image ID indicates date and shot number.

the range of relevant shifts below 1 mm. Based on the precision on the magnetic field measurement done for aligning the doublet it is estimated that the remaining lateral offsets from the orbit are in the order of a few 100 µm. Also, the size of the aperture in front of PMQ 1 and the accuracy of the positioning method for the setup in the chamber indicate this order of magnitude.

5.2. Rotation

The influence of an offset in the relative angle between the magnets focusing planes has been investigated in previous works both theoretically [31] and experimentally [97]. Therein it was found that even if the relative angle is a critical parameter for fluence maximization and bunch profile, the alignment of the magnets is good enough to reduce this error beyond the contributions of others. Another measurement of the bunch profile for different relative rotation angles φ_{QP} between the PMQs is shown in Fig. 5.4. The doublet was set to focus 12 MeV protons and the bunch profiles were recorded with scintillator and camera according to the scintillator setup Fig. 4.14b. A modification of the pre-aligned angle by rotating the first PMQ has a strong effect on the shape of the

observed focus distribution. The bunch profile size increases and two diagonal crossed wings appear. Depending on the sign of angle detuning φ_{QP}, the most intense wings are either on the top or bottom of the bunch center. Further, it is possible to observe a steering of the bunch. This shows that the central magnetic axes of the PMQs are not perfectly in the geometric center of the PMQs around which the rotation is performed. By rotating one PMQ the axes alignment is worsened resulting in a net dipole moment that causes the steering. According to the considerations of Sec. 5.1, the change of shape is not due to this steering effect though. Overall, this measurement confirms that relative angle between focusing planes has a very strong influence on the bunch profile. This was also found by Bin et al. in [111] where they required a broad dose distribution and identified $\varphi_{QP} \approx 5°$ to maximize their line focus fluence. That a rotation of PMQ 1 of only 0.8° causes a deterioration of the focus supports the assertion about the precision of the pre-alignment being 0.1° and confirms that it is better than one degree. It is possible to conclude that at a relative angle below 0.8° the influence of the bunch energy spectrum on the focus shape exceeds the influence of the angle such that the overall fluence distribution remains independent of the angle. This series of measurements proofs that it is fundamental for any focus optimization to minimize φ_{QP} to obtain minimum focus size and maximum fluence.

5.3. Drift Lengths

To investigate the influence of gradient uncertainties and the uncertainty of the z-positioning, the drift lengths d_1 and d_2 were varied from a calculated design value between different laser shots. The corresponding calculations for the beam profiles were made in [97] where it was found that every change from the optimized design parameters results in an increase of the spot size. Some example measurements for a 12 MeV design energy setup recorded with scintillator setup Fig. 4.14a are shown in Fig. 5.5. In this set of measurements the smallest focus size was obtained for a drift length d_1 1 mm larger than the design and drift length d_2 smaller by 1 mm (Fig. 5.5g). To see an observable change in the spot shape in the experiments the drifts had to be varied on the order of millimeters. Therefore this represents the order of magnitude to which the drift lengths for the optimized focus can be known. Although the offline alignment procedure as described in [31] suggests a higher precision for d_1, it is feasible that the error of determination of the magnet surface paired with the influence of gradient uncertainties and the exact position of the target can sum up to an uncertainty on the order of millimeter. The

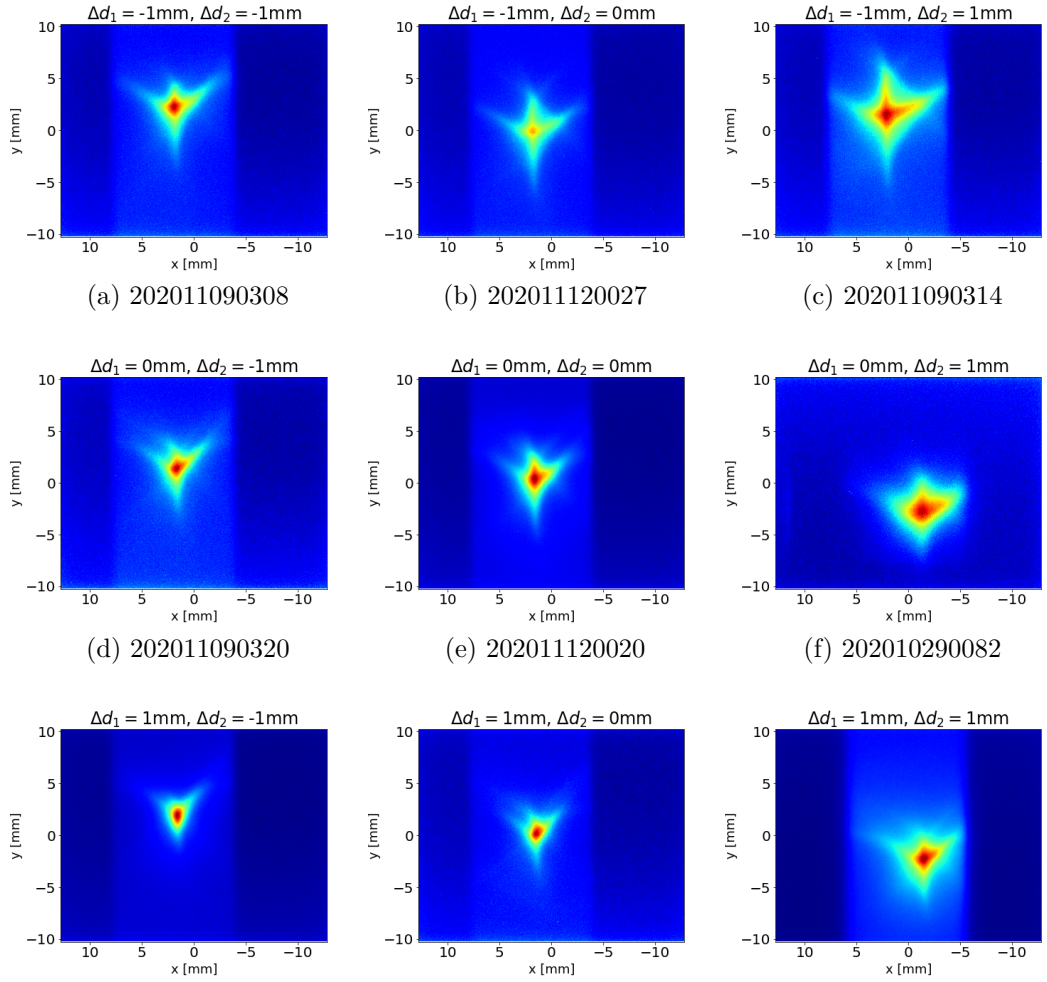

(a) 202011090308 (b) 202011120027 (c) 202011090314

(d) 202011090320 (e) 202011120020 (f) 202010290082

(g) 202011090305 (h) 202011120023 (i) 202010290062

Figure 5.5.: Bunch profile measurements for different offsets Δd_1 and Δd_2 from the calculated design energy drift lengths for a 12 MeV design energy setup. Data was collected over different experiment days and every image is normalized to its maximum. The image ID indicates date and shot number. Data acquired within the master-thesis work of L. Tischendorf.

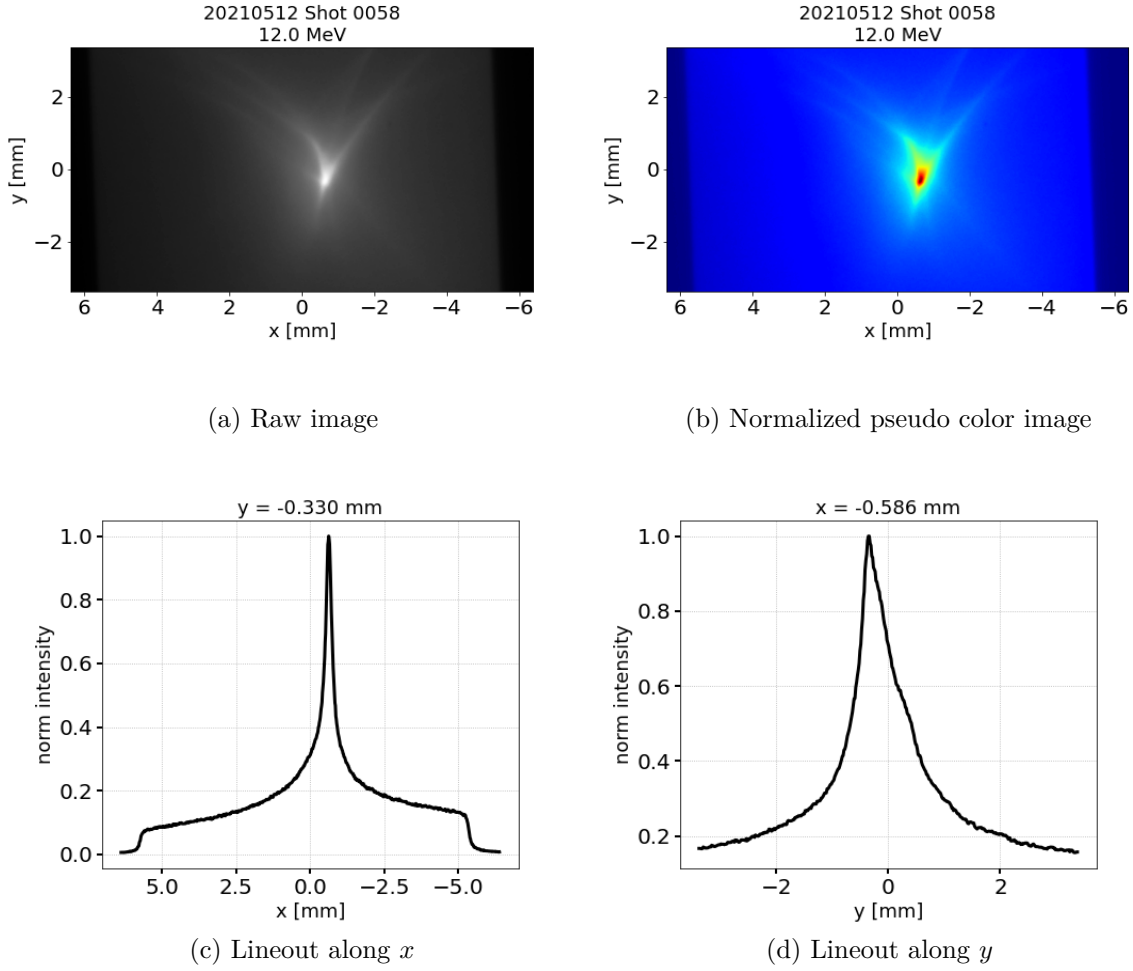

(a) Raw image

(b) Normalized pseudo color image

(c) Lineout along x

(d) Lineout along y

Figure 5.6.: Bunch profile measurement for 12 MeV design energy.

determination of d_2 which is based on lengths measurements with a caliper has a smaller uncertainty which is in the order of 100 µm. Nevertheless, experimentally it turned out that the optimized focus can be obtained for drift lengths up to a millimeter different from the calculated value. Therefore, the overall accuracy of both drift lengths can be estimated with 1 mm.

5.4. Best Proton Focus

The best possible proton focus was regarded as the smallest focus with minimum number of short wings closest possible to the beamline central axis. A typical optimized focus shape obtained with the LION doublet setup is shown in Fig. 5.6. This shape is obtained

when fine tuning the calculated drift lengths by varying them between shots around the design positions for 12 MeV. The signal was measured with the scintillator setup Fig. 4.14b as described in Sec.4.5. The raw image Fig. 5.6a allows to recognize the small thin wing structures that emerge around the central spot whereas the normalized pseudo color image Fig. 5.6b shows better the overall shape and the low and high fluence areas. One can see that the shape is not symmetric, slightly elongated and has a high intensity center with less intensive wings. The high intensity area is elliptical with a FWHM of (0.41 ± 0.04) mm in x direction and (1.08 ± 0.07) mm in y direction. The wings spread out on the order of millimeters around the center. The zero position of the image 5.6b is in its center and does not represent the center defined by the beamline. It is given in order to easier assess the focus size in the lineouts. Here, one can observe that the size of the focus is significantly larger than calculated for a perfect point source (Fig. 4.17a) but close to the size calculated with a 5 µm source for 12 MeV (Fig. 4.17b). This observation indicates that the source size is limiting the focus size of this imaging setup.

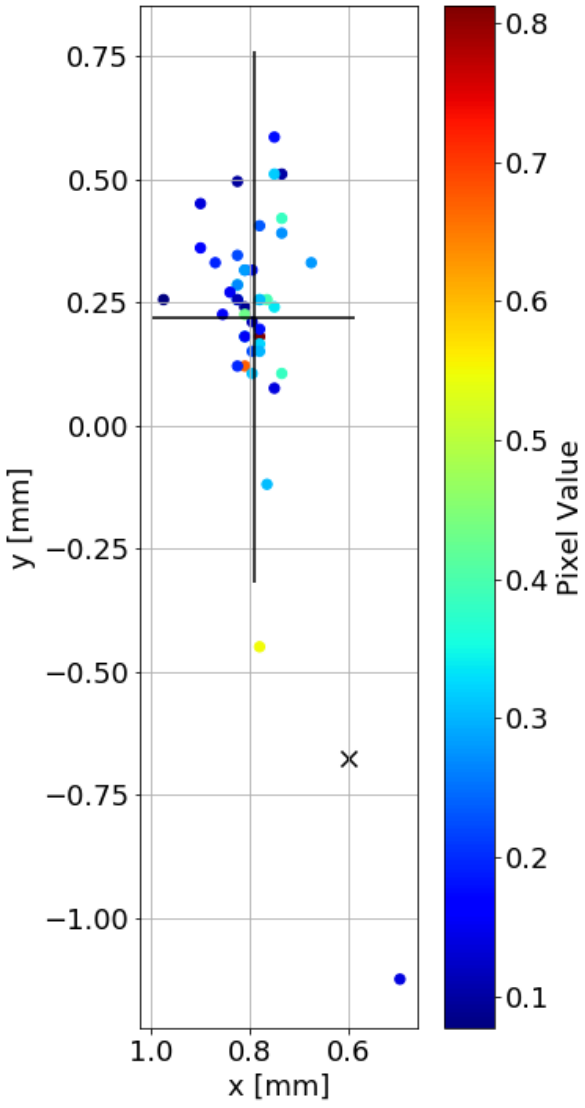

Figure 5.7.: Position of the peak in the fluence distribution for 45 consecutive shots with 12 MeV design energy setup from October 22, 2021 (Shots 158-202).

5.5. Reproducibility

To measure the stability of the bunch position in the focal plane a series of 45 consecutive shots was recorded and evaluated. Fig. 5.7 shows the result of these measurements as a scatter plot of the positions of the fluence peaks. For every shot the transverse position of the maximum fluence was determined and plotted in the transverse plane color coded with its pixel value in

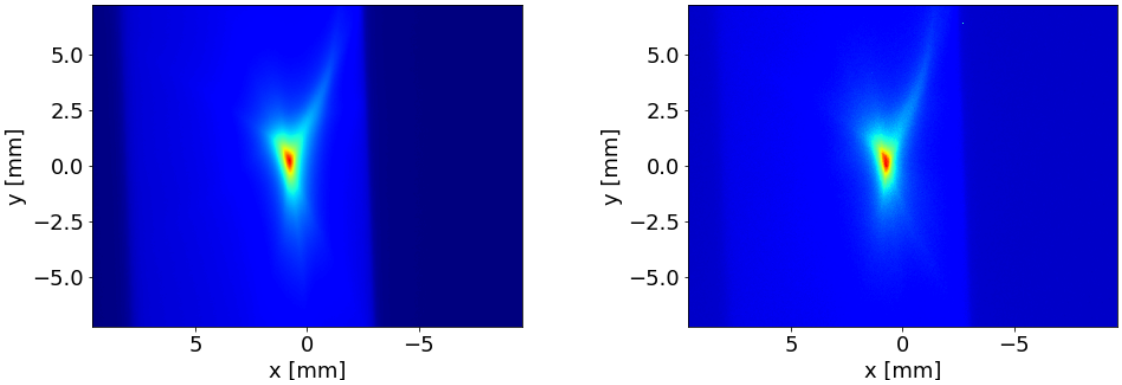

(a) Sum of 45 images (b) 20211022 Shot 179

Figure 5.8.: (a) Sum of images of 45 consecutive shots with 12 MeV design energy setup. (b) Example of a single shot of the 45.

the image. The zero axes in the figure correspond to the center of the image and the "x" marks the position of the defined center of the beamline. The vertical and horizontal lines represent the FWHM of the measured focus that was shown in Fig. 5.6. The position of the focus jitters less than the overall focus size and there is no obvious correlation between fluence and jitter. This indicates an overall sub-millimeter stability and reproducibility of the focus position which is illustrated by Fig. 5.8 where all 45 images are summed up and where the shape of a single bunch focus is retained (Fig. 5.8b). There is observable merely a slight blurring of the contours. Further, it is plausible to assume that the origin of the jitter is the jitter of the laser focus on the target. If one coarsely estimates from Fig. 5.7 a spread of the peak position of 300 µm in y and 150 µm in x and divides these values by the estimated magnification of 47 and 7 respectively, one obtains around 6 µm and 21 µm of jitter in the target plane. The value is on the order of magnitude of the laser focus diameter which coincides with the focal spot position jitter that we measured independently.

5.6. Source Size Estimation

The proton focus was investigated and optimized for different design energy setups. For all setups the drift offset was corrected to obtain the best focus and resulted in a constant offset of $\Delta d_1 = 1\,\text{mm}$ and $\Delta d_2 = -1\,\text{mm}$. For a meaningful analysis of the focus size, a set of suitable focus images had to be selected from the images recorded during the

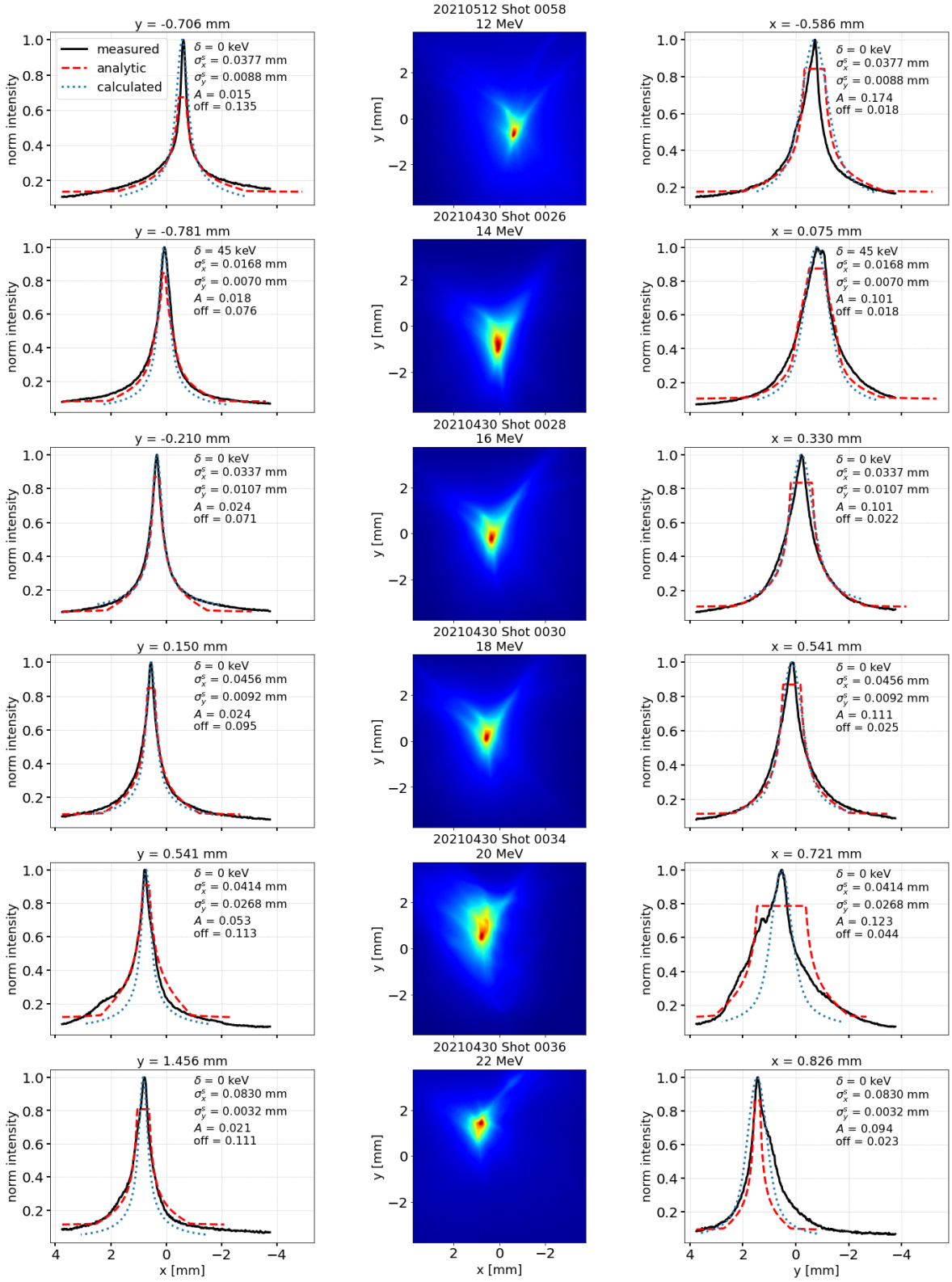

Figure 5.9.: Source size estimation for optimized foci of different design energies. Normalized focus images and lineouts in x (DOFO) and y (FODO) direction of measured data. Fits of the analytic model and forward calculated lineouts from Gaussian source distribution.

different experimental campaigns. Fig. 5.9 shows example images of different design energies chosen from the available data set. For selection they were required to not be saturated and exhibit a high signal level above background. The intensity was normalized to the individual image maximum because the number of protons diminishes for higher proton energy according to the spectrum of accelerated protons.

At the sides of the images the lineouts through the intensity peak along x (left side) and y (right side) are displayed. According to the method presented in Sec. 4.6 the analytical model was fit to these lineouts simultaneously in both dimensions in the range $x > 0$ and $y > 0$. Alignment errors were neglected since after the considerations in the sections above it is clear that they are small enough to have only little influence on the overall focus shape. Therefore one can assume the focus shape being mainly determined by the spectrum and the source size. The resulting lineouts are plotted as red dashed lines with the scaled fit parameters shown to their side. The source sizes σ_x^s and σ_y^s were calculated by rescaling the fit results for the minimum spot size with the average a_x and a_y parameters calculated from Fig. 4.24, the magnifications $V_x(p_0)$ and $V_y(p_0)$ as well as the correction factors κ_x and κ_y. The detuning δ was obtained by scaling the fit parameter δ' with p_0.

For comparison and shown in blue dotted lines, there were also plotted the lineouts of a Gaussian spatial distribution with a $\sigma_x^s = 20\,\mu\text{m}$ and $\sigma_y^s = 8\,\mu\text{m}$ for all design energies, forward calculated with the numerical integration method. These source sizes were found manually to reproduce best the measured lineouts. Varying them by 2 µm already leads to a mismatch between calculated and measured profile. It was tried to use the numerically calculated lineouts as fitting function, but the fit routine did not converge and no good agreement with the data was achieved. The numerical calculation seems to be too complex for an automated fit which shows the value of the analytic model.

The fit of the analytical model reproduce well the slope of the measured data but as the model parts from the assumption of a flat spatial source distribution, the fitted lineout saturates at some level below the peak of the measured lineouts. Also the forward calculated and measured lineouts are in good agreement. They confirm the order of magnitude of the fitted source sizes and show that the a priory assumption of a source distribution is not critical for the determination of the source size. However, as expected assuming a Gaussian distribution yields smaller source sizes than retrieved result with the flat distribution.

After having shown that the analysis method works for exemplary measurements across the design energy setups the analysis was expanded towards all available suiting

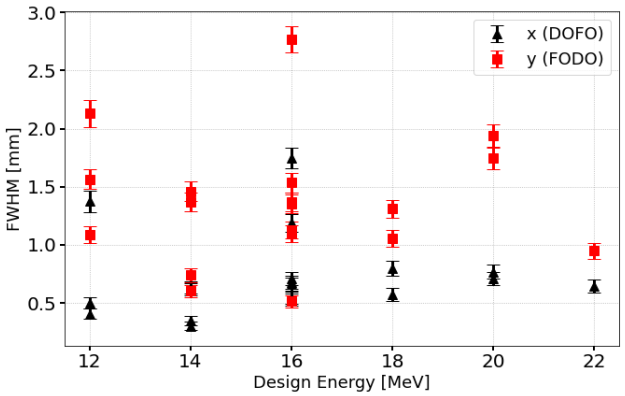

Figure 5.10.: Proton focus size for different design energy settings.

images, partially measured also on other experiment days. The FWHM of these foci were calculated and are shown in Fig. 5.10. The uncertainty was determined as the radius of a circle with the same area as the one given by the number of pixel covered by the FWHM

$$\Delta FWHM = \sqrt{\frac{FWHM}{l_{pix}} \frac{A_{pix}}{\pi}} \tag{5.2}$$

where l_{pix} is the width of a pixel and A_{pix} the area of a pixel. The average FWHM of all normalized foci are (0.7 ± 0.3) mm in x and (1.4 ± 0.5) mm in y and, in agreement with the expectations, larger in FODO dimension y than in DOFO dimension x. Within the observed variability there is no significant energy dependence of the focus size. The large spread in measured size for the same design energy setup is more pronounced in the high magnification dimension and is probably related to shot-to-shot or day-to-day fluctuation of the source conditions.

Fig. 5.11 shows the retrieved source sizes for all these measurements. The errors were calculated according to Eq. 4.9 assuming the errors determined in Sec. 4.6 and $\Delta FWHM$ was used as error of the minimum spot size $\Delta\sigma'_{x0/y0}$. The dashed lines indicate the source sizes used for the forward calculation with the numerical model using the Gaussian distribution that was shown in Fig. 5.9. Again, within the uncertainty margin there is no observable dependance on the design energy. In accordance with the forward calculation the source size suggest larger source size in DOFO dimension x than in FODO dimension y. Due to the smaller magnification and larger correction factor the uncertainty in x is larger. Nevertheless, the average values over all energies are $\hat{\sigma}^s_x = (34 \pm 18)$ µm and $\hat{\sigma}^s_y = (11 \pm 7)$ µm and are larger than but comparable to the laser focus size. The large

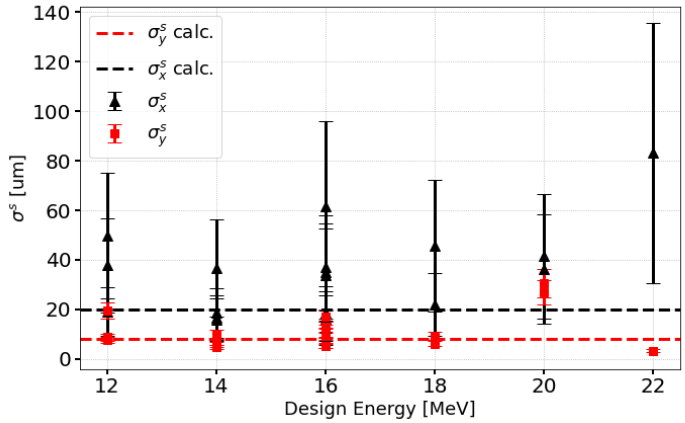

Figure 5.11.: Retrieved source size for different design energy settings. The dashed lines indicate the size of the source used for the numerical forward calculation in Fig. 5.9.

variability of the results can thus be attributed as well to the shot-to-shot or day-to-day fluctuations.

The shot-to-shot fluctuations can be assessed by analyzing the 45 foci from consecutive laser shots used to investigate the reproducibility in Sec. 5.5. They were recorded for the 12 MeV design energy setup with comparable laser and target conditions. After excluding saturated and low signal images the data set reduced to 31 foci whose FWHM and retrieved source sizes are shown in Fig. 5.12. One can see that the fluctuations of FWHM and σ^s are on the same order as between different design energy setups. This confirms that the variability of the measured source size caused by changing micro-conditions of laser and target is larger than the variability due to the spectrum. Therefore, one can conclude that within this variability it is not possible to observe an energy dependent source size and attribute the fluctuations to changes of size of the source.

Also for this data set both the forward calculation and the analytical model indicate that the lineouts can be best reproduced with the assumption of an elliptical source size with larger extension in x than in y. Again for the forward calculation $\hat{\sigma}_x^s = 20\,\mu\text{m}$ and $\hat{\sigma}_y^s = 8\,\mu\text{m}$ best approximate the measurements. Retrieving the source size from the analytical model yields $\hat{\sigma}_x^s = (36 \pm 9)\,\mu\text{m}$ and $\hat{\sigma}_y^s = (8 \pm 3)\,\mu\text{m}$, which is in good agreement with Fig. 5.11. Note that this data set was recorded around 6 months later than the data shown in Fig. 5.11 indicating a long term reproducibility of the observation.

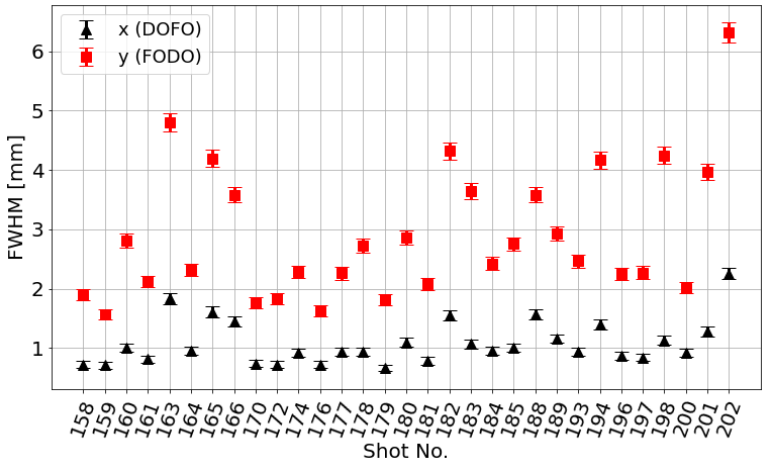

(a)

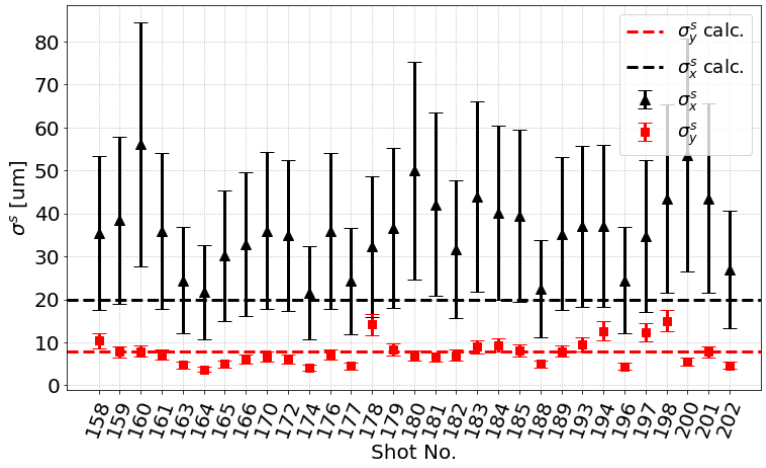

(b)

Figure 5.12.: Source size analysis of 31 of the 45 shots used for Fig. 5.7. (a) Measured FWHM. (b) Retreived source sizes σ^s. The dashed lines indicate the size of the source used for the numerical forward calculation.

5.7. Dose Distribution in Focus

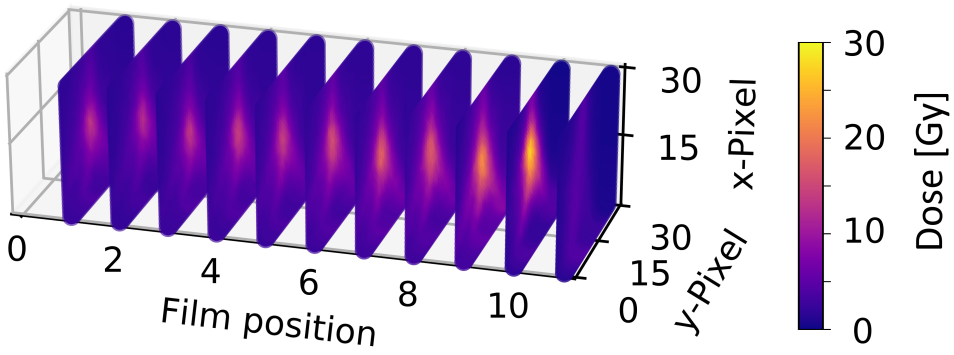

Figure 5.13.: Dose distribution in the RCF stack for 18 MeV design energy and three accumulated bunches. Image taken and adapted from [106] with permission from D. Walcher.

The dose distribution of the optimized focus was measured with a calibrated stack of RCFs for different design energies in the bachelor thesis work of D. Walcher [106]. Each stack contained 20 RCF layers. For design energies 12–16 MeV individual bunches were recorded. In the range between 18–20 MeV three bunches were accumulated. The evaluated dose distribution within 11 of the 20 RCFs obtained from 3 accumulated shots with design energy 18 MeV is shown in Fig. 5.13. From the central area of $1.28 \times 1.28\,\mathrm{mm}^2$ where the dose is highest we can extract an average depth dose curve.

This measurement of single shot dose deposition can be compared to the calculated depth dose curves from Fig. 4.27 with the spectrum over an area with 0.5 mm radius. However, the area used for the measurement evaluation corresponds to a 0.7 mm radius. As this difference is small, the calculated curves could be scaled by the ratio between these areas to make all curves comparable. The resulting curves at 12 and 16 MeV design energy are plotted in Fig. 5.14. The measured and calculated curves agree very well in the range of the particles within less than half a millimeter. The peak mean dose of the calculated 12 MeV curve is in between the two measured values which illustrate the variability of the dose due to shot-to-shot fluctuations. For 16 MeV the calculated peak value is smaller than the measured one. The ratio of the 12 MeV peak to the 16 MeV peak is comparable between measurement and calculation being for calculated curves 4.4 and for the average of the measured curves 3.1. An explanation for the differences is that the spectrum from Fig. 4.15, which is the basis for the calculated depth dose

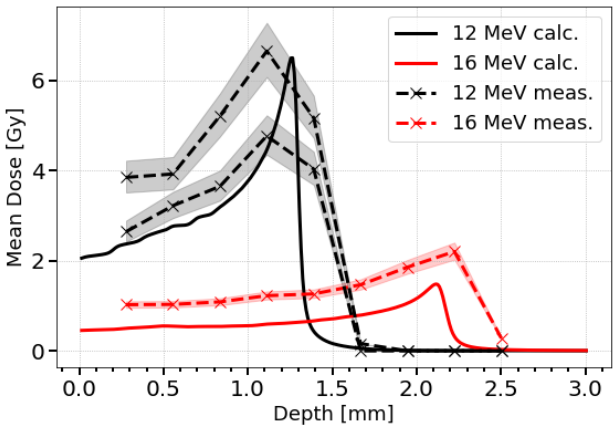

Figure 5.14.: Depth dose curves from RCF stack measurements [106] (dashed lines) and calculations with radius 0.5 mm from Fig. 4.27 (solid lines). To make all curves comparable, the calculated curves were scaled by the ratio to the area used for the measurement evaluation.

curves, was recorded on a different day than the RCF measurement. Although the laser and target parameter were apparently the same, the actual ion spectrum has likely varied significantly between experiment days. Therefore, considering shot-to-shot and day-to-day fluctuations in the spectrum, the calculated mean dose distributions agree well with the measured ones.

5.8. Transverse Steering

To determine the absolute position of the focal spot with respect to the beamline an alignment laser pointer was used for defining the central axis along the experimental chamber. For coarse alignment the PMQs were positioned along this axis (the fine alignment of the setup is described in [31]). The laser spot on the Kapton exit window was marked and transferred to the aluminum cover foil by drawing a cross. Overlaying the camera image of the cross with the image of the scintillator one can determine an absolute steering of the proton bunch. Fig. 5.15 shows six of these overlay images taken for six different design energy setups after optimization.

The distances of the maximum fluence position from the horizontal (x dimension) and vertical (y dimension) lines were measured for every image and are summarized in Table 5.1. The uncertainties were calculated by adding the line width, the resolution uncertainty and a spot size uncertainty. The latter was determined by the radius of the

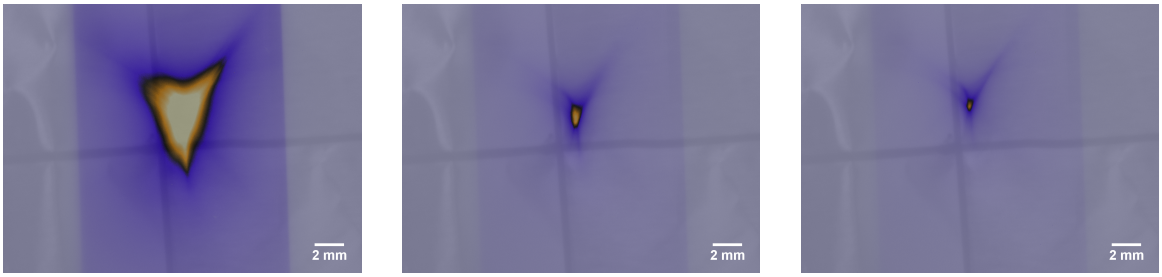

(a) 20210430 Shot 24
12 MeV design energy

(b) 20210430 Shot 26
14 MeV design energy

(c) 20210430 Shot 28
16 MeV design energy

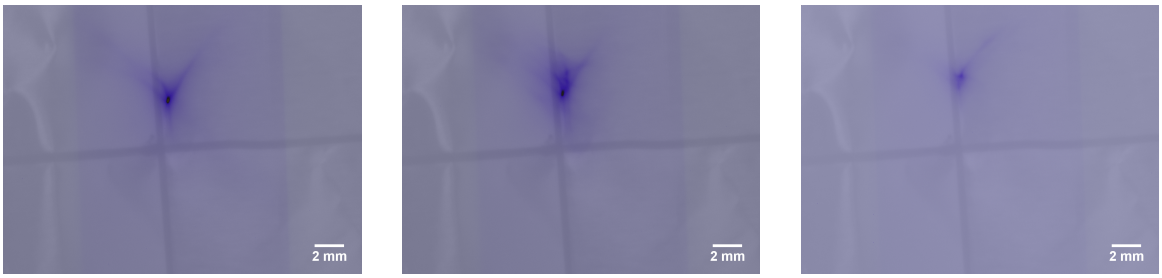

(d) 20210430 Shot 30
18 MeV design energy

(e) 20210430 Shot 34
20 MeV design energy

(f) 20210430 Shot 36
22 MeV design energy

Figure 5.15.: Observation of steering on April 30, 2021. Focus images overlaid with the reference image of the central chamber axis position for optimized setups with different design energies.

Shot. No	$\mathcal{E}_D$	Distance Y [mm]	Distance X [mm]
24	12 MeV	(2 ± 2) mm	(1 ± 2) mm
26	14 MeV	(2.0 ± 0.6) mm	(1.2 ± 0.6) mm
28	16 MeV	(2.8 ± 0.6) mm	(1.0 ± 0.5) mm
30	18 MeV	(3.2 ± 0.6) mm	(0.7 ± 0.5) mm
34	20 MeV	(3.7 ± 0.7) mm	(0.5 ± 0.6) mm
26	22 MeV	(4.9 ± 0.7) mm	(0.5 ± 0.5) mm

Table 5.1.: Measurement of steering with shots from April 30, 2021

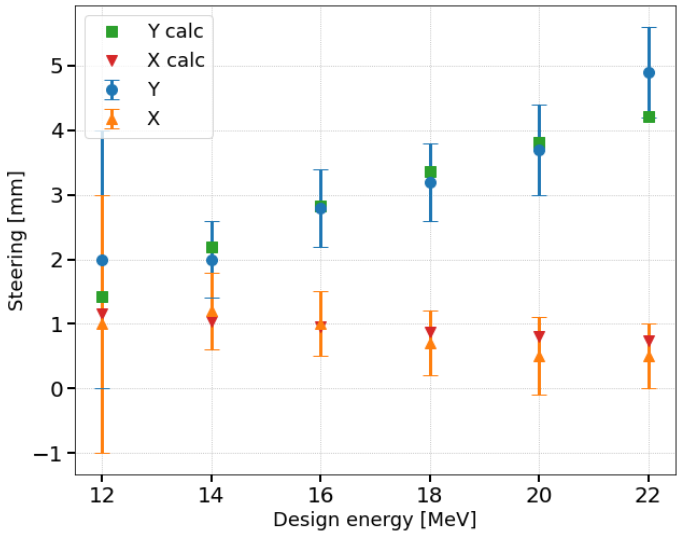

Figure 5.16.: Representation of results from Table 5.1 for the steering in x and y together with the calculated steering resulting from transverse doublet offsets of 250 µm in x and −250 µm in y.

circular area that corresponds to the area of all pixels with an intensity above 75% of the maximum intensity of the image.

Fig. 5.16 shows these displacement values as function of design energy and the trend that the steering away from the axis increases with increasing proton energy in y and decreases in x. Because the steering originates from a dipole moment due to lateral displacement of the PMQs, this observation is contrary to the expectation. Therefore this result indicates, that the axis defined by the alignment laser does not correspond to the magnetic central axis of the PMQs setup. From the direction of the steering one can deduce, that the cross marks a position that is below and left of the actual PMQ axis.

This behavior can be reproduced when calculating the steering of a design energy particle for a constant lateral absolute offset of the doublet adding the absolute position of the axis. In Fig. 5.16 the shifts of the design particle position in the focal plane were calculated with offsets of 250 µm in x and −250 µm in y and reproduce the measurements within the error margin. A constant value of 13.5 mm and −0.8 mm was added to the shift values to consider the axis shift in agreement with the observation, that the cross marks are above and left of the real axis. The absolute offsets assumed here could easily be corrected in the experiment leading to the focus being at the same position for all energy settings. However, this would probably lead to a focus position away from the

central chamber axis. One likely cause of this discrepancy between chamber and magnet axis could be alignment errors in tip and tilt of the magnets inside the positioning setup, which cannot be easily adjusted to higher precision. Another possible reason could be that the magnetic axes of the individual PMQs are tilted with respect to the geometric axes of the bore. Both possibilities lead to the effect that changing the drift lengths does not move the magnets along their magnetic axes, resulting in the observed steering.

6. The LION Quadruplet

The majority of studies within this work considered a single quadrupole doublet. The geometric boundary conditions were such that the microscopically small source was imaged with high magnification to a distance of approximately 1.85 m downstream. This allowed for the collection of the largest number of particles, but of course resulted in comparably large proton foci with an extent of 0.7 mm by 1.4 mm. Reducing the spot size, potentially down to the initial source size of 34 µm and 11 µm within the same geometric conditions requires further particle optics. We therefore study the potential of using a second PMQ doublet in a refocusing geometry with the upstream doublet, i.e. the complete beamline now consists of a quadruplet.

6.1. Imaging with a Quadruplet

In the ideal refocusing geometry the four magnets consist of two identical but inverted doublets with pairwise the first and the last as well as the second and the third PMQ having the same strength. The first pair of quadrupoles is positioned close to the particle source to collect as many particles as possible. It is set to reduce the divergence of the design energy particles to zero in order to transport them with parallel trajectories to the second pair. This second pair is positioned as close to the focus as the first pair is to the target creating a strong focusing which ideally recovers the initial source size. Therefore, the entire setup comprises five drift sections, d_1 and d_2 for the first doublet, d_3 as parallel

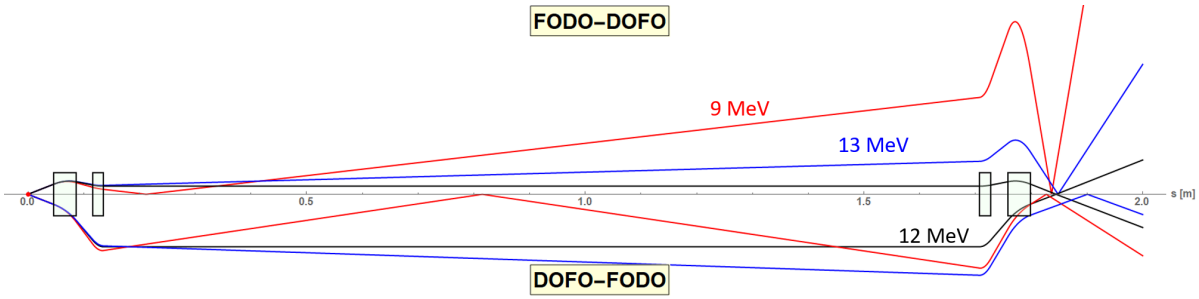

Figure 6.1.: Example trajectories through a PMQ quadruplet for protons with the design energy of 12 MeV and a higher and lower energy.

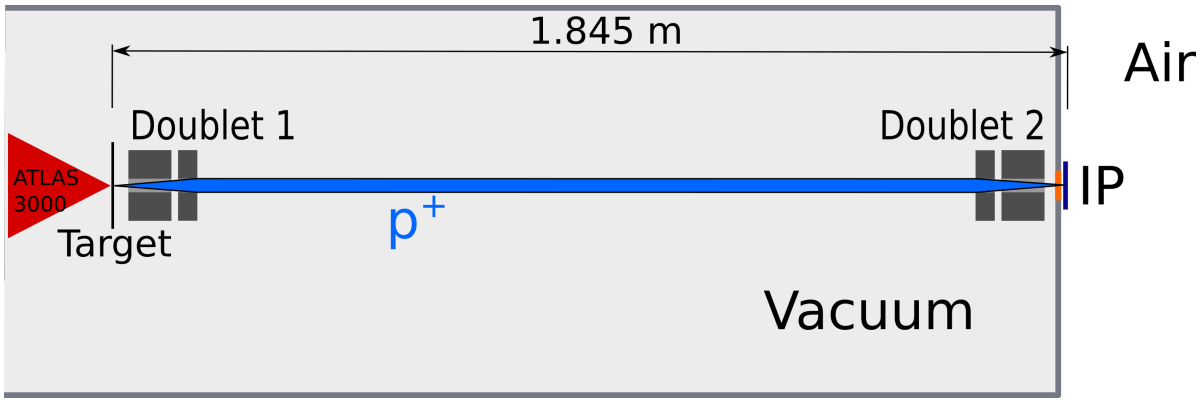

Figure 6.2.: Scheme of the quadruplet focusing setup in CALA LION with an image plate (IP) as detector system. Dimensions are not to scale.

drift section between the doublets and finally d_4 and d_5 for the second doublet.

Like in the case of the doublet only particles of the design energy are transported correctly and particles of different energies deviate from the ideal trajectories exiting the first doublet with a large variety of divergences. Fig. 6.1 shows the trajectories with maximum extend for a design energy particle together with two trajectories of one higher and one lower particle energy. However, a refocusing arrangement of quadrupoles exhibits two design energies. It is not only possible to focus particles of energies that are parallelized and refocused but also particles of lower energies that are re-imaged from an intermediate focus which causes them to have a second focus after the second doublet. Due to the broad energy spectrum of the laser-driven source this second focus at lower energy will contribute significantly to the proton fluence at a certain lower proton energy.

6.2. Quadruplet Setup

The schematic representation of the quadruplet setup in the CALA LION experiment is shown in Fig. 6.2. A second doublet was added downstream of the first in close proximity to the vacuum exit window.

	Length	Gradient sim.	Gradient exp.
PMQ 1	40 mm	(329 ± 12) T/m	(332 ± 13) T/m
PMQ 2	20 mm	(333 ± 13) T/m	(334 ± 13) T/m
PMQ 3	20 mm	(322 ± 2) T/m	N.A.
PMQ 4	40 mm	(332 ± 5) T/m	N.A.

Table 6.1.: Gradients of the LION quadruplet PMQs according to [97]

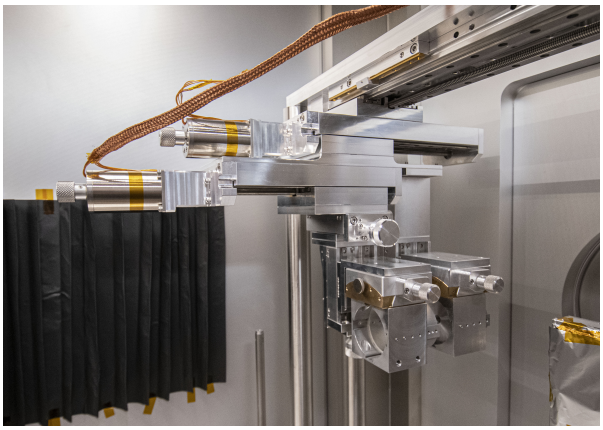

Figure 6.3.: Second pair of PMQs installed in the back of the LION vacuum chamber. Image by T. Naeser.

The second doublet consisting of PMQ 3 and PMQ 4 with lengths and gradients given in Table 6.1 was assembled with motorized and manual stages analogous to the first doublet (assembled of PMQ 1 and PMQ 2). The only difference was that the relative rotation between both quadrupoles was not motorized, because the pre-alignment procedure has proven sufficient as concluded in Sec. 5.2. A picture of the setup is shown in Fig. 6.3. To protect the magnets from debris or ionizing radiation, a 1 cm thick aluminum disc with a 1 cm diameter aperture was mounted on the upstream surface of both magnets. The setup was pre-aligned with the magnetic hall sensor measurement similar to the first doublet [31, 97] and transferred to the vacuum chamber. The alignment with respect to the axis of the first doublet was done optically via an alignment laser diode of 1 mm diameter which is used as reference for all beamline elements inside the chamber.

The positions of the magnets along the beamline where calculated with the same algorithm as for the doublet. For a desired design energy, the drift lengths d_1 and d_2 for the first doublet where calculated for a TFD of 30 m representing a long distance and yielding the drifts that produce a parallelized bunch of design energy particles. This approach of using a large but arbitrary TFD does not represent the best solution for the problem of finding the drift lengths for the quadruplet. However, it was found to represent a solution within the uncertainty range of the gradients and a good starting point for further experimental investigations. For an identical but inverted second doublet it would be possible to simply set $d_4 = d_2$ and $d_5 = d_1$ with an arbitrary d_3. But since the second doublet magnets have slightly different gradients they had to be calculated separately. As the trajectories through the magnetic fields are invertible the drift lengths were obtained by calculating the drift lengths for parallelizing the bunch with the same

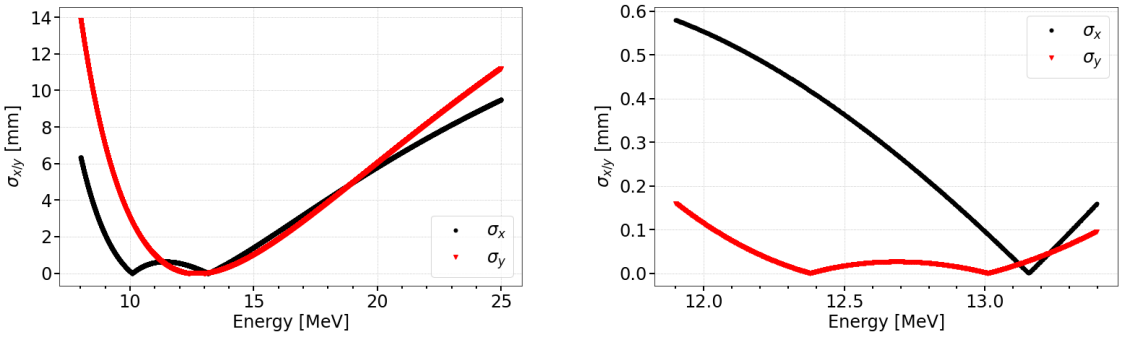

(a) (b)

Figure 6.4.: Calculated bunch size in the focal plane as function of proton energy for a setup design energy of 13 MeV and TFD of 1.845 m. (a): Size over the whole spectrum. (b): Zoom into the energy range around the two focused energies.

parameters as for the first doublet. The drifts were then set downstream in reversed order, such that $d_4 \approx d_2$ and $d_5 \approx d_1$. d_3 was determined by the demand that the proton focus had to be on air at 1.845 m away from the target. This means that the second doublet was positioned so far downstream that d_5 was equal to the distance between the exit of PMQ 4 and the Kapton window of the vacuum chamber.

Fig. 6.4 shows the calculated bunch size per energy for the quadruplet for calculated drift positions for 13 MeV design energy. One can see that there are four particle energies that exhibit a minimum spot size in the focal plane. First, there is one bunch size minimum in each transverse dimension close to the design energy indicating the refocused energies. The fact that these energies are different in both dimensions, i.e. that there is a detuning of $\delta \approx 100$ keV, confirms that the drift lengths are not optimized yet and that a better calculation method is required. For every transverse dimension there is also a second different energy with a minimum, creating an overall larger area around the high energy spot in which protons with lower energies contribute dose. The position in the spectrum of these second minima depend on d_3 and therefore also on TFD and design energy.

Fig. 6.5 shows the results of the calculation of the fluence distribution in the focal plane made by adapting the system matrix to the quadruplet configuration. The calculation was performed assuming a flat top fluence distribution in the focal plane and using the source sizes which were determined from the measured doublet focus in Sec. 5.6, $\sigma_x^s = 34\,\mu$m and $\sigma_y^s = 11\,\mu$m. The obtained result shows that the elliptical source shape is recovered. However, the lineouts through its center yield a FWHM of $x_{flat}^{FWHM} = 120\,\mu$m

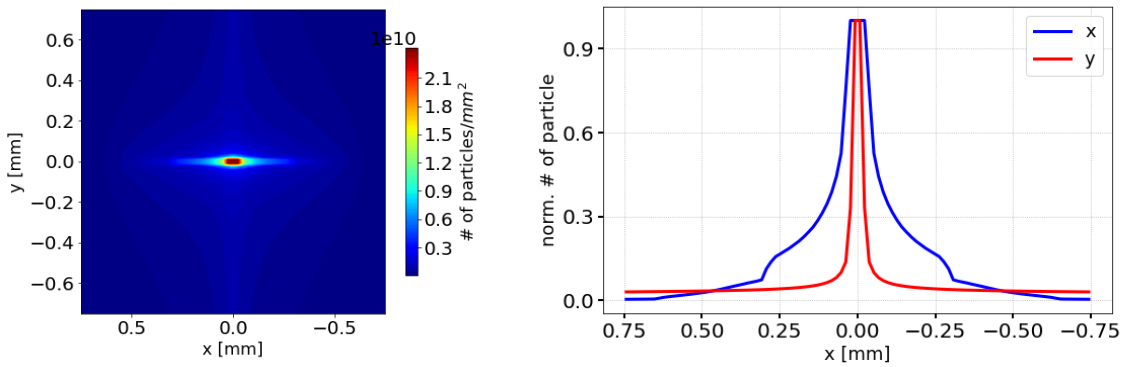

(a) (b)

Figure 6.5.: (a) Bunch profile of the quadruplet setup in the focal plane for a setup design energy of 13 MeV and a TFD of 1.845 m calculated with a flat top distribution using the in 5.6 determined source sizes of $\sigma_x^s = 34\,\mu\text{m}$ and $\sigma_y^s = 11\,\mu\text{m}$. (b) Lineouts through the center of the calculated fluence distribution.

and $y_{flat}^{FWHM} = 30\,\mu\text{m}$, which are larger than the source size. The large detuning in Fig. 6.4 prevents a complete refocusing. Therefore, an adaptation of all drift lengths is required that minimizes the detuning. Nonetheless, regardless of this optimization potential, the fluence calculation lets expect a focus one order of magnitude smaller than obtained with the doublet.

6.3. Quadruplet Focus

Fig. 6.6 shows scans of IPs that were irradiated with a single bunch, one for which the design energy was set to 13 MeV and one for 17 MeV. The IPs were scanned multiple times until no saturation was observed anymore. For the lower design energy of 13 MeV (Fig. 6.6a) it is possible to observe two distinct spots. They have elongated elliptical shapes with an angle of almost 90° between the major axes and are separated by $\approx 350\,\mu\text{m}$ at their closest encounter and $\approx 1\,\text{mm}$ between their respective maxima in y direction. The top spot is less intense than the bottom spot indicating a smaller fluence, i.e. less particles in that area. For the higher design energy the top spot vanished (Fig. 6.6b). Only in the second IP scan there is a faint remnant of an increased fluence around the expected position of the top spot. The separation of the spots together with the fainting of the top spot for higher design energies indicates that the two spots represent foci of two different proton energies with the top spot corresponding to the higher and the bottom

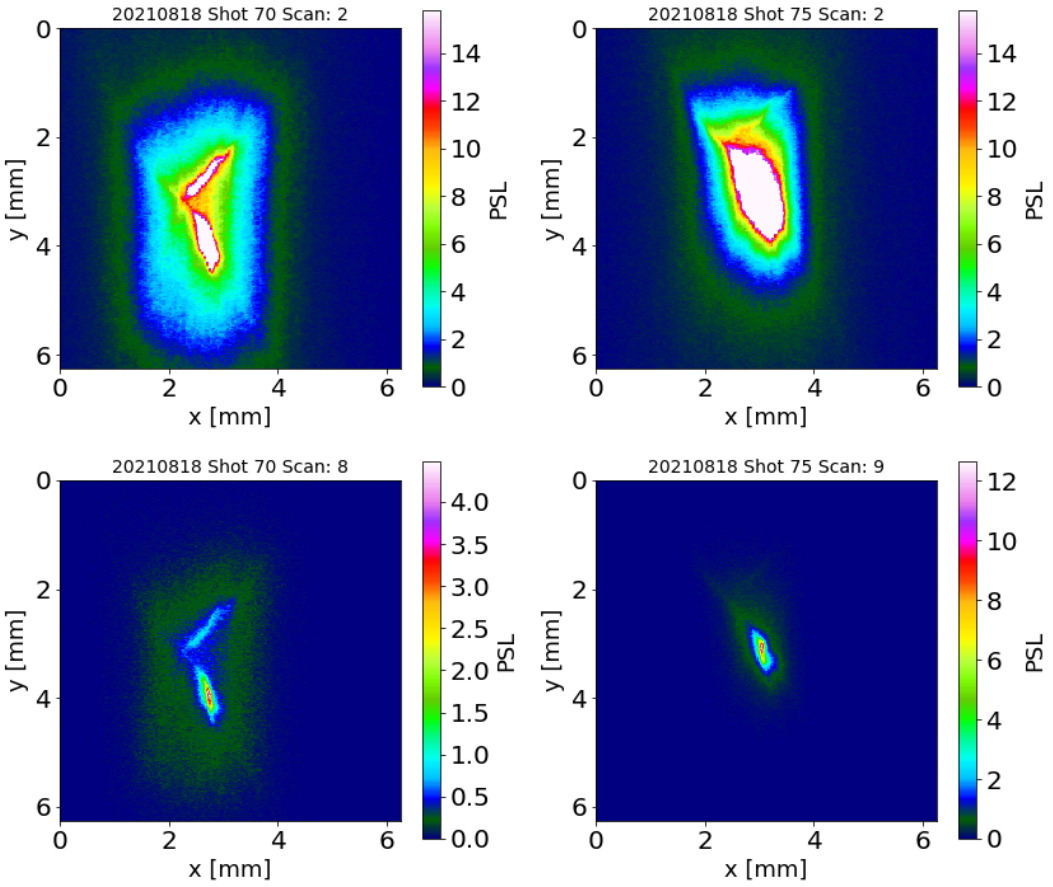

(a) 13 MeV (b) 17 MeV

Figure 6.6.: Images of the quadruplet focus for different design energies. Second and last scan of image plates for one shot with 13 MeV (a) and one shot with 17 MeV (b) design energy setups. The intensity is given in units of Photo Stimulated Luminescence (PSL).

spot to the lower focused proton energy. As explained in Sec.6.1 the quadruplet operated in a refocusing geometry has the property to focus two particle energies simultaneously. The separation results from a dipole moment in the beamline originating most probably from a relative misalignment of the two doublets. The dipole moment induced by the second doublet is likely irrelevant as it would need to be very strong to cause a 1 mm separation of MeV protons over few centimeters of trajectory. Therefore the magnets would need to be strongly misaligned which is not likely given the results of the previous investigations on the first doublet. On the other hand, a relative misalignment between both doublets can be easily produced during the setup of the system, since the alignment by means of a laser is precise only to 1 mm and the non-motorized vertical axis could

	FWHM (13 MeV)	FWHM (17 MeV)
Low Energy Focus Major Axis	(1.3 ± 0.1) mm	(0.93 ± 0.09) mm
Low Energy Focus Minor Axis	(0.55 ± 0.07) mm	(0.45 ± 0.06) mm
High Energy Focus Major Axis	(1.7 ± 0.1) mm	N.A.
High Energy Focus Minor Axis	(0.40 ± 0.06) mm	N.A.

Table 6.2.: Measured focus sizes from the shots with the PMQ quadruplet on Fig. 6.6

not be adjusted online. The difference in intensities in the 13 MeV setup agrees with the exponential energy spectrum of the bunch and the high number of low energy protons and low number of high energy protons. The vanishing of the top focus for the 17 MeV setup can be explained by the circumstance that the bunch maximum cutoff energy was below 17 MeV.

The sizes of the measured foci are listed in Table 6.2. Compared to the focus size produced with the doublet, the quadruplet foci are not considerably smaller. Further, they are much larger than expected from Fig. 6.5 meaning that the size increase originated from additional effects than the large detuning which dominates the size in the calculation. Together with the measured elongated shape this suggests that the combined uncertainties of drift length calculation and magnetic field gradients demand a experimental optimization of the drift lengths to reduce the focus size to the order of the source size.

A direct comparison of two consecutive shots with doublet and quadruplet on the same stationary IP is shown in Fig. 6.7. To record this image, first, the protons were focused with the upstream doublet using the calculated drift lengths for focusing on the vacuum exit window. For the next shot d_1 and d_2 were changed to parallelize the bunch and the downstream doublet was inserted into the beamline with d_4 and d_5 set to the calculated refocusing drift lengths.

This measurement allowed some important observations. First, introducing the second doublet moved the focus about 1 cm downwards. This shows clearly that there is a relative misalignment in y between both doublets that introduced energy dependent steering and hence the appearance of two quadruplet foci.

Second, even if the high fluence areas of both foci are comparable in size, the quadruplet focus exhibits a much steeper fluence gradient, confining the intense fluence to the central spot region giving the impression of a smaller focus. For the doublet case the fluence gradient in the spot is shallower. It is also worth noting that the fluence contributing to the background originates from the doublet shot only. Both observations mean that the quadruplet creates a cleaner focus with less background fluence which can be important for certain applications.

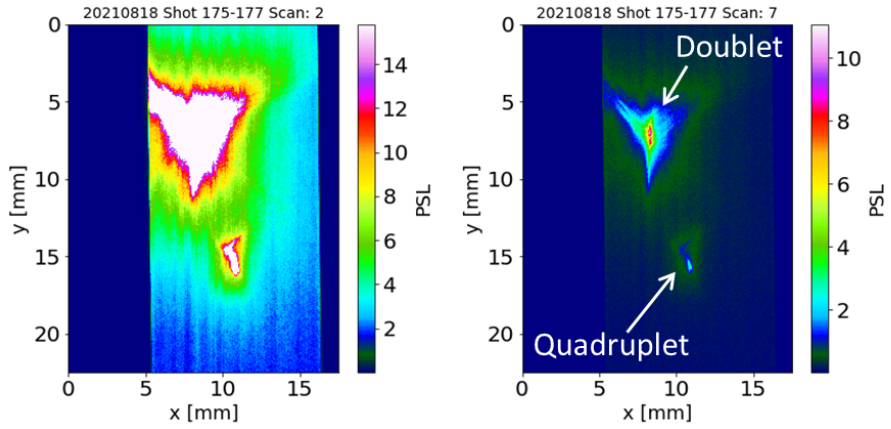

Figure 6.7.: Comparison of the focus from the doublet and the quadruplet setup. Second and last scan of the image plate. Both shots were delivered consecutively to the same image plate without a change of position of the plate.

Last, the doublet focus has not the optimized shape observed in Sec. 5.4. This suggests that the first doublet was not in the optimal position with the calculated drift lengths. It is the consequence of the gradient uncertainties that had been corrected for the optimized doublet focus. Therefore, these uncertainties influence also the shape of the quadruplet focus when the second pair of PMQs is introduced in the beamline with the calculated drift lengths, which confirms the demand for a drift length optimization to achieve an emittance limited focus. For that, d_1, d_2, d_4 and d_5 would need to be varied until minimizing the focus size. The parameters of most decisive influence are expected to be d_2 and d_4 as they have the strongest influence on the bunch divergence [31]. From the optimization of the doublet Sec. 5.3 one can adopt that the drift lengths have to be varied on the order of $\pm 1\,\mathrm{mm}$. Using three positions for four parameters results in 81 possible combinations for a first identification of a minimum. A final optimization might require fine alignment exploring few more settings and resulting in an expected optimization of the drift lengths with less than 100 proton bunches at one design energy. The determined offsets to the calculated drifts can then be applied at all design energy setups.

7. Discussion

The characterization of the LION focusing setup, accompanied by the development of mathematical tools that model the focus fluence distribution under consideration of the broad energy spectrum, enabled the measurement of a source size of the laser-driven protons. In summary, the measurement method consisted of creating the smallest possible proton focus and, after excluding sources of shape distortions, identifying it with the image of the proton source. Its size was retrieved by fitting the observed fluence distribution with a modeled image of known source size.

The developed analytical model was key for this approach and it is important to discuss some assumptions on which this model relies. First, it is postulated that the proton emission from the source is isotropic, i.e. there is no angular dependence on the proton energy. In general, for TNSA sources this is wrong. But as the opening angle accepted by the imaging system is smaller than commonly reported divergences for the highest proton energies of more than 10° [32, 38, 85], the assumption is regarded valid for the modeled proton transport behavior.

Second, a single measured WASP spectrum (Fig. 4.15) was chosen as representative for all fluence calculations in this work under the assumption that the spectrum has no influence on the focus shape. It is based on the narrow energy bandwidth of the protons contribution to the spectrum as calculated in Sec. 4.7. This can be further verified by comparing the fluence distributions calculated with two different spectra close to the cutoff energy of one of them. Fig. 7.1 shows the fluence distributions calculated for a 16 MeV design energy setup with the respective input spectra. One can see that the particle numbers and background level differ strongly for a changing spectrum but the spot size and shape are not affected. This observation justifies the assumption of a flat spectrum in a narrow energy range around the design energy made for the derivation of the analytical model. Furthermore, it supports the statement that measured changes in the focus size originate in changes of the source size and the spatial source distribution. The lack of knowledge of this distribution is a major source of uncertainty in the source size determination.

It is important to recognize that due to the imaging nature of the measurement, the smallest possible proton focus is not related to the actual area of the target from where

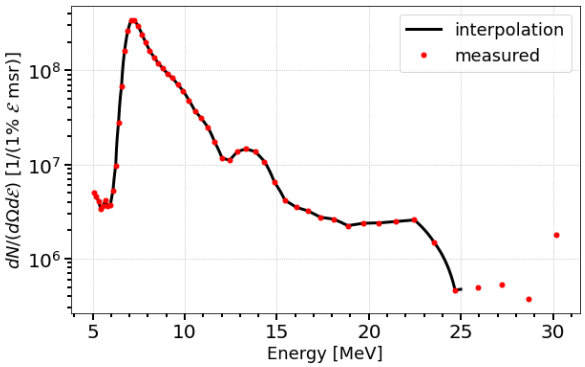

(a) Spectrum shot 202105120005

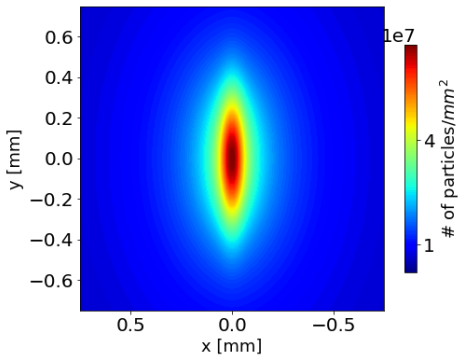

(b) Gauss source

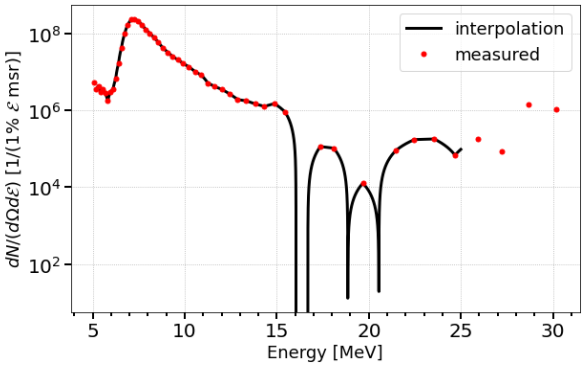

(c) Spectrum shot 202105120008

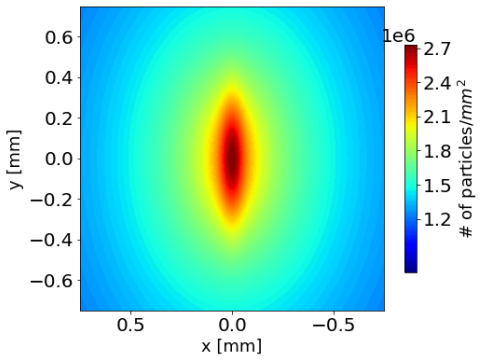

(d) Gauss source

Figure 7.1.: Influence of the bunch spectrum on the resulting fluence distributions for a 16 MeV deign energy setup.

the protons originate, called real source size, but to the emittance limited minimum possible source size, called the virtual source size. Therefore, by extracting a source size from this proton focus one obtains only a lower limit for the real source size.

Because of the flat spectrum assumption the calculated source size represents a source size valid only for the spectral interval that contributes to the focus. Hence, if the design energies are chosen sufficiently far apart, the source size for different particle energies can be determined which are expected to vary according to the TNSA behavior. However, no energy dependence within the uncertainty range was observed in this study. Therefore, one can claim that within the margin of error the virtual source size seems to be constant in the investigated energy regime. Its position along the beamline as well as the real source size cannot be extracted by this method. The error of the drift lengths of 1 mm translates to several centimeters changes in TFD yielding a too high uncertainty to

determine the source position. Due to the fact that the scattering in the vacuum exit window was minimized the resolution of the imaging setup is mainly determined by the quadrupoles. In a first try the resolution was estimated by choosing a source size for forward calculation that yielded the same lineout as the measurements. This lead to an estimate of 2 µm resolution for the source size.

The results of this thesis add important information to the variety of experiments that have investigated both real and virtual source sizes of proton bunches from thin foils for different proton energies with different techniques. In many cases, microstructured targets with RCF stacks as detectors were used to image the target rear side directly and obtain a spatially and energy resolved proton distribution for a bunch. The structure could be either machined directly in the target rear [16, 32–35, 85, 112] or imprinted with lasers into the plasma [38, 88]. In another approach RCF stacks were used for measuring the projection of metal meshes [38, 86]. Both methods rely on the analysis of a single shot for the determination of the source size. The well known target structure or mesh acts as fiducial for the magnification and therefore, in combination with the notion of the geometric lengths of the setup, both divergence and source size of the full proton bunch can be calculated for a single shot. Methods that structure the target rear side are used to determine the real source size whereas imaging methods are only able to measure the virtual source size. A multi-shot technique was the stepwise covering of the source with a knife edge with subsequent measurement of the spectrum in a Thompson parabola spectrometer and CR39 nuclear track detectors [87]. The vanishing of certain energies from the spectrum as a function of the knife edges transverse position behind the target indicate the area where they originated. This method sampled only the central beam with almost vanishing divergence and thus cannot be regarded as complete characterization of the source. The results of several studies employing one of these methods are summarized in Table 7.1. This table is not exclusive and further examples that agree with the listed values can be found in a similar table in [88].

Except for the works by Schreiber et al. [87] and Sommer et al. [88] the results of the mentioned experiments are based on single shots on metal foils with lasers of several 100 fs pulse duration. JanUSP, ATLAS and DRACO are titanium sapphire lasers operating at a wavelength around 800 nm. All other systems are glass laser systems at 1054 nm wavelength. Intensities were comparable in all experiments. The main differences between experiments was the target thickness. Nevertheless, the thickness in all reported experiments was larger than 2 µm which indicates operation in the TNSA regime. In contrast, the data provided in this work represent first information on proton source

Publication	Target (Laser)	$\mathcal{E}$ [MeV]	S_{real} [µm]	S_{virt} [µm]
Roth *et al.* 2002 [33, 34]	Au/Al/CH 5-100 µm (100TW-LULI)	3 10	260 80	
Patel *et al.* 2003 [16]	Al 20 µm (JanUSP)	4 12	250 80	
Cowan *et al.* 2004 [32]	Al 18 µm	4.5 7 $9-10$	70 45 ≈ 30	
Borghesi *et al.* 2004 [38]	Al 3 µm (JanUSP)	15	80 ± 30	10
Schreiber *et al.* 2004 [87]	Al 5 µm (ATLAS10)	> 0.8 < 0.8	<80 <500	
Brambrink *et al.* 2006 [85]	Au 25 µm (100TW-LULI)	6⋆ 8⋆ 9.5⋆ 11⋆ 12.5⋆	130⋆ 90⋆ 100⋆ 75⋆ 70⋆	
Roth *et al.* 2006 [112]	Au 50 µm	3⋆ 6⋆ 8⋆ 10⋆ 11⋆	90⋆ 73⋆ 50⋆ 47⋆ 35⋆	
Nürnberg *et al.* 2009 [35]	Au 30 µm (PHELIX)	< 1.2	57	4.0
	Au 10 µm (TRIDENT)	6.4 9.9 13.5	69 42 24	4.0 1.0 0.9
	Au 50 µm (100TW-LULI)	4.7 9.8 13.3	85 45 25	5.4 1.4 0.4
	Au 25 µm (VULCAN)	6.2 17.4	500 220	12.1 11.0
Sommer *et al.* 2018 [88]	2 µm Ti (DRACO)	4.7	450	
Liu *et al.* 2021 [86]	Au 10 µm (SG-II UP PW)	6.4 7.9 9.1 10.6 12.0 13.3 15.2 16.8 18.9		19.2 22.9 13.7 12.4 10.2 10.7 11.0 13.8 17.9

Table 7.1.: Overview of literature values for virtual (S_{virt}) and real (S_{real}) source diameters as function of proton energy $\mathcal{E}$. Values marked with ⋆ are approximations read from graphs. Not all laser systems could be identified in the publications.

sizes for thinner foils, in which the rear side cannot be considered unaffected by laser light. The measurements were made with 400–600 nm plastic foils and a pulse duration of 28 fs. The laser focus intensity was $4 \cdot 10^{20}\,\mathrm{W/cm^2}$ to $8 \cdot 10^{20}\,\mathrm{W/cm^2}$ and therefore comparable to the presented experiments. It is worth mentioning that we typically observed a transmission of laser energy in the range of 10^{-2} to 10^{-3} after optimizing the laser-target interaction for best proton performance.

All methods characterized the source with offline detectors which needed elaborate post-processing and were positioned close to the source. In contrast, the method of imaging the source with quadrupole magnets presents itself as an online tool to analyze the source from a remote distance and with the possibility of detection on air. No special targets or objects in the bunch that potentially bias the measurement are required and one obtains information about the bunch as it is used for a potential application. Both target thickness and material are not accessible for the microstructure technique because fabrication of such targets remains complicated.

On the other hand, the source size estimation relies on the energy selectivity of the quadrupoles and hence requires multiple shots to investigate the entire proton spectrum. The limit for the measurement is given by the minimum achievable distance between target and magnets and prevented to investigate further towards lower energies than 12 MeV design energy. Furthermore, due to the high repetition rate laser and target systems in the LION experiment, it was possible to investigate beyond single shots and obtain first results on shot-to-shot fluctuations. Interestingly, it seems that the source size, shape or distribution are the main contributions to variations in observed proton foci. Although the origin of these variations remains unclear, it is interesting from the context if laser-plasma interaction and related instabilities [113–116].

Over the sum of the here given publications one can find values for source size in the energy range between around 1 and almost 19 MeV. The measured diameters differ significantly for real and virtual sources. Real source sizes were found to span between 24 µm for 13.5 MeV and 500 µm for 6.2 MeV. Overall there seems to be an almost linear dependance of the energy and the source size. This linear trend is not so clear for the virtual source sizes. Per definition they are much smaller than the real source sizes and diameters between 0.4 µm and 22.9 µm can be found for different energy values.

The quadrupole imaging method determined a virtual source size that appears to be constant over a large range of the spectrum, thereby having a width of $\sigma_x^s = (34 \pm 18)\,\mu\mathrm{m}$ in DOFO and $\sigma_y^s = (11 \pm 7)\,\mu\mathrm{m}$ in FODO dimension, i.e. a diameter of around 68 µm and 22 µm, which is much larger than the virtual source sizes measured for micrometer foils

(Tab. 7.1). However, as the here determined values are estimated under the assumption of a flat spatial particle source distribution, a 39% smaller size, i.e. 21 µm and 7 µm are still within the uncertainty range due to the in reality unknown distribution. The independence of the source size from particle energy could be a hint towards a changing acceleration behavior during the laser plasma interaction in the transition away from TNSA dominated acceleration towards the onset of relativistic transparency effects. The short pulse duration with high contrast (10^{-10} at ns [95]) and thin target thickness provide suitable conditions for this regime. This assumption is supported by the observation that during the experiments the highest proton energies were always observed when there was a residual transmission of light through the target of the order of 10^{-2} to 10^{-3}.

In terms of source size and energy independence these results are most comparable with the study of Liu et al. [86] that represents the only available study where the mesh method was implemented to determine the virtual source size for different energies separated by their stopping in a RCF stack. Here, the virtual source size was almost constant and without correlation with the investigated range of particle energies. However, the authors give no explanation for their observations. In analogy to the attempted explanation of the results of the work at hand, one could imagine that for their 1053 nm laser with 130 J in 1 ps [86] the 10 µm target thickness provided comparable conditions to alter the regular TNSA behavior.

In contrast to all reported values, the virtual source sizes obtained with the imaging method are different in the transverse dimensions suggesting a larger virtual source in x than in y. However, as the virtual source size represents the lower limit for a possible focus size it is determined by the source emittance. Assuming an isotropic source means there is no correlation between divergence and source size and, therefore, the emittance is given by reducing Eq. 3.11 to

$$\varepsilon_x = \sigma_x \sigma_{x'}.$$

The PMQ doublet limits the divergence of the bunch to the acceptance and for the measurements this resulted in maximum divergence angles $x'_{max} = (15 \pm 2)$ mrad and $y'_{ap} = (31 \pm 4)$ mrad. With the determined virtual source sizes one can calculate a trace space emittance of $\varepsilon_x = (0.5 \pm 0.3)$ mm mrad and $\varepsilon_y = (0.3 \pm 0.2)$ mm mrad showing that the emittance is comparable for both transverse dimensions. Therefore, the ellipticity of the virtual source can be seen as a consequence of the different acceptance angles of the doublet. Hence, these values are not representative for the complete source, but for the part of the beam that is transmitted through the quadrupole doublet. In this sense, they represent lower limits for the complete source emittance. Therefore, the imaging method

alone is not suited to determine the complete emittance. Additional measurements of the divergence would be required and such techniques as the well known quadrupole scanning method [37] adapted to the present setup.

For some of the publications listed in Table 7.1 it was possible to calculate a bunch trace space emittance as they characterized the bunch directly after the source. Cowan et al. [32] determined a normalized transverse emittance of $< 0.004\,\mathrm{mm\,mrad}$ for 10 MeV protons. Without normalization this transfers to 0.03 mm mrad which is about 10 times smaller than the values calculated for our case. The difference diminishes for 7 MeV where they measure a trace space emittance of 0.1 mm mrad. Other normalized trace space emittance measurements can be recalculated to even greater values at, e.g. 1.7 mm mrad for 15 MeV in Borghesi et al. (normalized $\varepsilon_N = 0.1\pi\mathrm{mm\,mrad}$) [38] and similar for Roth et al. [33].

Wu et al. did not determine a source size but measured the trace space emittance with different methods along different points of a beamline with electromagnetic quadrupoles and a dipole [36]. For 5 MeV they measured a normalized trace space emittance $\varepsilon_N = 0.02\,\mathrm{mm\,mrad}$ after the target with the pepper-pot method [37] and $\varepsilon_N = 0.048\,\mathrm{mm\,mrad}$ at 2.5 m after the quadrupole triplet with the quadrupole scan technique [37]. These values without normalization transfer to 0.2 mm mrad and 0.5 mm mrad. They show the potential of emittance growth of particle bunches with large energy spread along a beamline [36, 117]. However, since our source reconstruction considers the bunch energy spread it inherently accounts for this emittance growth resulting in the determination of the source emittance. A calculation of the emittance in the image plane using the measured focus size of $x^{FWHM} = (0.7 \pm 0.3)\,\mathrm{mm}$ and $y^{FWHM} = (1.4 \pm 0.5)\,\mathrm{mm}$ and the calculated bunch divergence for the maximum source divergence at 12 MeV design energy at the exit of the quadrupoles $x' = 2.2\,\mathrm{mrad}$ and $y' = 0.7\,\mathrm{mrad}$ results in $\varepsilon_x^f = (0.7 \pm 0.3)\,\mathrm{mm\,mrad}$ and $\varepsilon_y^f = (0.4 \pm 0.1)\,\mathrm{mm\,mrad}$ which are slightly larger than the determined source emittance.

Most experiments operated in the TNSA regime and those seem to yield rather small emittance values. In TNSA, the target rear side can be considered unperturbed by the laser light. Therefore, the surface where the protons are accelerated is cold, i.e. the transverse electron temperature is low [32, 33]. For thinner targets as used in this work, this assumption is likely invalid as the laser starts affecting the entire target. Transmission of laser light can be observed [95] and heating of the target rear surface can lead to associated increase of the transverse phase space emittance. Assuming a transmission of 1% of the laser intensity yields an intensity on the target rear on the

order of $10^{18}\,\mathrm{W/cm^2}$ which is sufficient to impart MeV kinetic energy on electrons and 0.5 keV on protons simply by the oscillatory kinetic energy of particles in the laser field. A fraction of this energy would be enough to cause a larger transverse emittance. When parting from a cold surface temperature of $300\,\mathrm{K} = 25\,\mathrm{meV}$ an increase by a factor 100 of the transverse velocity of the electrons $v_{trans} \propto \sqrt{T_e}$ would require a temperature rise of a factor 10^4, i.e. an energy around only 250 eV. Even though this is a very speculative example it sheds light on the relation of emittance, target thickness and transmission that is worth investigating in greater detail. Considering that the inset of (relativistic) transparency is a very sudden process [89] and hence unstable, this might also explain the large fluctuations of our estimated virtual source sizes.

8. Conclusions and Outlook

The scope of this thesis comprised an extensive investigation of foci of laser-driven protons produced with PMQs. Various technological developments opened up the possibility to explore a wide range of setup parameters and record a vast set of experimental data. Based on this new resources, measured focal spots were analyzed in terms of spot size, shape and position in order to understand the influence of the broad proton energy spectrum and determine the limitations of the transport system in practice. This endeavor was accompanied by the development of different calculation tools to disentangle the contributions to the focus of the two major components, the transport system and the source.

The implementation of laser and radiation protection measures was important to achieve a reliable operation of the focusing setup. This allowed to perform parameter studies whose first result was that the implemented method to pre-align rotation and drift lengths is precise enough to start experiments close to the optimum. The remaining misalignment originates from e.g. gradient uncertainties and can be corrected during the experiment by online adaptation of the drift lengths. The imprinted transverse steering of the bunch originates from residual transverse misalignment which was within the range of few hundred micrometer and could be corrected in the motorized horizontal dimension. A correction in the manually adjustable vertical position is possible but more cumbersome since a venting cycle is required during the experiment. Nevertheless, the required adjustment for correcting this vertical steering is now possible within one or two iterations, based on the quantitative understanding of the transport system and predictive calculations.

Observing the reproducibility of the focus position over a series of consecutive shots showed the rigidity of the setup and suggests that the jitter is related to the laser focus jitter on the target or, even more interesting, the related change of laser-plasma interaction dynamics. The experiments confirmed that the resolution of the imaging system is able to image changes in the source position on the order of a few micrometers. The study also allows to assess the quality of the focus for application experiments and opens the way for planning reliable irradiation experiments.

Important conclusions were made regarding the acceptance of the setup. Even if the

chosen aperture in front of the magnets did not meet the ideal requirements, trajectory calculations suggest that it reduces the deposition of dose in the magnet bulk. The aperture does not match the acceptance of the doublet. Tailoring the bunch divergence to the acceptance in both dimensions is expected to increase the number of transported particles by a factor of six and correspondingly improve the shielding effect.

Neither the particle tracking nor the calculation methods can reproduce the complex real shape of the focus. Imperfections in the quadrupole field and steering could be ruled out experimentally in this work in agreement with previous works by others [97]. Fringe fields (or higher moments) could play an important role and should be investigated further. However, as of now, it is not obvious if the quality of the permanent magnet quadrupoles can be significantly improved. It is also likely that the wide spread background dose observed in many acquisitions is due to secondary radiation or particles other than protons.

The thorough characterization of the setup provided a high reproducibility of the proton focus for many experiment days over months of operation. Achieving the smallest possible focus size in combination with the detailed calculations enabled to retrieve a emittance dominated proton virtual source size of $\sigma_x^s = (34 \pm 18)\,\mu\text{m}$ and $\sigma_y^s = (11 \pm 7)\,\mu\text{m}$ for proton energies between 12 MeV and 22 MeV. As the calculated fluence distributions include the influence of the broad proton energy spectrum the results suggest that the virtual source size is energy independent within the uncertainty range. This and the overall large size are in strong contrast to evident TNSA sources.

The uncertainty of the source size originates mainly from the lack of knowledge of the spatial particle distribution of the source. We chose two representative extreme cases to assess this effect, a flat top and a Gaussian distribution. Whereas the $\sigma_x^s = (34 \pm 18)\,\mu\text{m}$ and $\sigma_y^s = (11 \pm 7)\,\mu\text{m}$ sizes are determined under the assumption of a flat distribution, a Gaussian distribution would result in a 39% smaller source. Further, shot-to-shot changes of the measured FWHM influence the uncertainty of the retrieved source size. However, the observation of the shot-to-shot fluctuations for consecutive shots suggest that they represent real changes of the source size due to fluctuating laser, target and plasma conditions.

Understanding the proton focus produced with the quadrupole doublet opens up the way to further, more detailed investigations on thin foils as sources. The LION setup was conceived in a way that different target thicknesses and materials can be employed easily in the same experiment. A vast range of parameters are available for more detailed experiments. Further, the potential of a simultaneous multi-species acceleration and

focusing of e.g. protons and carbons deserves more investigation. The WASP spectrum measurements already indicate the presence of carbon ions in the bunches. If these carbons are energetic enough they can be focused simultaneously with the protons. For non-relativistic protons and C^{6+} the total carbon energy has to be a factor 3 higher than the proton energy and carbon ions close to 36 MeV are possible to create with our laser and target parameters. However, to test this hypothesis, diagnostics need to be implemented that are capable of discriminating ion species of which the simplest example would be CR39 nuclear track detectors.

Due to the chromatic properties of the doublet it is also possible to envision an application as proton spectrometer for the laser-accelerated ion bunch. From the calculation of $\sigma(p)$ (Fig. 4.16) it became clear that in the focal plane there is a strong correlation between transverse position and proton energy spectrum. The further away from the focus the smaller the contributing energies. Therefore the information about the spectrum is contained in the radial lineouts in the focal plane and can under the right conditions be extracted.

Also, application experiments in the radiobiology context could benefit from the newly gained information over the focus on an air irradiation site. The focus shape does not depend on the design energy. With this stable focus position that was demonstrated in Sec. 5.5, reproducible energy and position scans are feasible and can be used to deliver a variety of dose patterns. However, it has been shown that the shot-to-shot fluctuations represent a major challenge for these kind of experiments [118]. One way to tackle this is an improved on-shot dosimetry that can cope with the high particle numbers and doses in the proton focus. The development of these and other dedicated laser-driven ion detectors and methods is the most immediate usage of the focused proton bunches.

In a last step it was demonstrated that even smaller foci are potentially possible using a PMQ quadruplet. Still, the setup needs further investigation, but many tools developed in this work can be adapted to describe the quadruplet setup and facilitate the analysis. With the four magnets and five drift lengths, the quadruplet setup is more challenging for alignment as all parameters need to be optimized to minimize steering and spot size. However, not only the perspective smaller spot size but also the double focus might in the future be interesting for research and dedicated applications.

Appendices

A. Analytic Solution of the Fluence Distribution with No Detuning and Minimum Spot Size

For the case of no detuning $\delta' = 0$ and a minimum spot size $\sigma'_{x0} = \sigma'_{y0} = 0$, the energy dependent bunch sizes Eq. 3.70 in the imaging plane become

$$\sigma'_x(p') = \left|1 - \frac{1}{p'}\right|, \quad \sigma'_y(p') = \left|1 - \frac{1}{p'}\right|. \tag{A.1}$$

In other words in this normalized system, the ellipses have the same extend in both dimensions and the bunch profiles are concentric circles. The simplified fluence is then

$$F(x', y') = \int \frac{N_0}{\pi \sigma'_x(p') \sigma'_y(p')} \, dp' = \frac{N_0}{\pi} \int \frac{p'^2}{(p'-1)^2} \, dp' = \frac{N_0}{\pi} \left[p' + \frac{1}{1-p'} + 2\ln(|p'-1|) \right]. \tag{A.2}$$

Both the logarithmic term and the fraction $\frac{1}{1-p'}$ diverge for $p' \to 1$. This property represents the fact that particles with this momentum would be perfectly focused on a point with zero area, i.e. simply all particles are transported to $(0, 0)$. In a heuristic interpretation one can argue that this behavior is represented by $\frac{1}{1-p'} \to \infty$ and $2\ln(|p'-1|) \to -\infty$ for $p' \to 1$, leaving as main contribution the first term in Eq. A.2, the finite total particle number.

Again it is the next step to find the limits for the indefinite integral. The radius of the circles as a function of momentum is

$$r' = \sqrt{x'^2 + y'^2} = \left|1 - \frac{1}{p'}\right|$$

. One can see, that the pole at $p' = 1$ translates to a divergence of the fluence for $r' = 0$. The integration limits can be found by rearranging this equation and taking into account

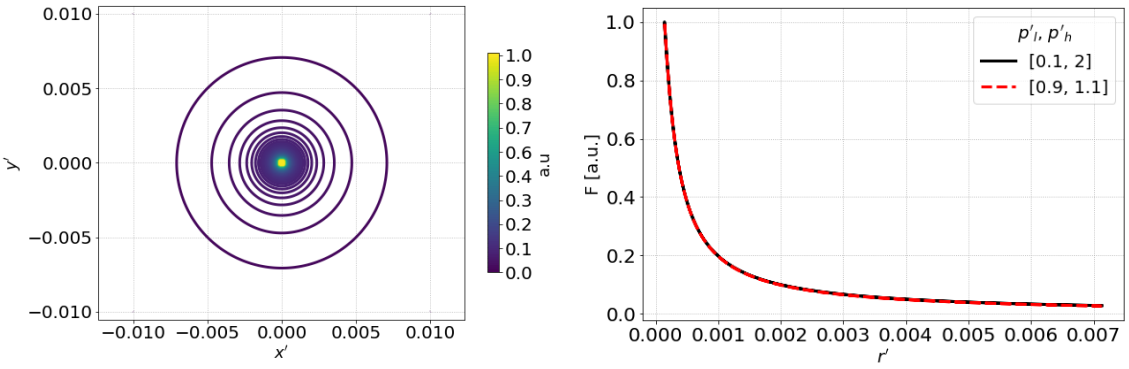

(a) (b)

Figure A.1.: (a) Iso fluence contours for a the analytic fluence distribution calculated with Eq. A.5 and $p'_l = 0.1$ and $p'_h = 2$. (b) Fluence distribution as function of r' for two different spectral widths around the design momentum $p' = 1$.

the absolute value

$$\text{for } p' < 1: \qquad p' \leq \frac{1}{r+1} = p'^{+} \tag{A.3}$$

$$\text{for } p' > 1, r' < 1: \qquad p' \geq \frac{1}{1-r'} = p'^{-} \ . \tag{A.4}$$

For $p' > 1, r' > 1$ there is no contributions from high momenta so one can simply set $p'^{-} = p'_h$. In summary the intervals of integration are $[p'_l, p'^{+}]$ and $[p'^{-}, p'_h]$ and the fluence distribution in the focal plane has the shape

$$F\left(x', y'\right) = \frac{N_0}{\pi}\left(p'_h - p'_l - \frac{p'_h - p'_l}{\left(p'_h - 1\right)\left(1 - p'_l\right)} + \frac{2\left(1 - 2r'^2\right)}{\left(1 + r'\right)\left(1 - r'\right)r'} + 2\ln\left(\frac{p'_h - 1}{1 - p'_l} \cdot \frac{1 - r'}{1 + r'}\right)\right). \tag{A.5}$$

Based on this function the 2D fluence distribution for an ideal source in the positive quadrant can be calculated for $0 < r' < 1$. Fig. A.1 displays one example calculation with $0.0001 \leq r' \leq 0.01$. In Fig. A.1a the result of such calculation in the first quadrant was mirrored to the rest of the quadrants to complete the 2D image. The circular iso fluence contour lines is a consequence of the normalization of the spacial quantities. Fig. A.1b shows the fluence as function of r' for two different spectral widths. By limiting the spectrum to a narrow bandwidth around the design energy $0.9 < p' < 1.1$, one can again confirm that the focal shape is mainly determined by the particles of momenta close to the design energy. As expected, the fluence diverges for $r' \to 0$ as the integration limits

approach $p' = 1$. Therefore, this solution is not suited to determine a with of the fluence distribution.

Publications and Conference Contributions

Peer-Reviewed Publications

1. **T. F. Rösch**, Z. Szabó, D. Haffa, J. Bin, S. Brunner, F. S. Englbrecht, A. A. Friedl, Y. Gao, J. Hartmann, P. Hilz, C. Kreuzer, F. H. Lindner, T. M. Ostermayr, R. Polanek, M. Speicher, E. R. Szabó, D. Taray, T. Tőkés, M. Würl, K. Parodi, K. Hideghéty and J. Schreiber. A feasibility study of zebrafish embryo irradiation with laser-accelerated protons. *Rev. Sci. Instrum.*, 91, 6, 063303, 2020.

2. D. Haffa, R. Yang, J. Bin, S. Lehrack, F.-E. Brack, H. Ding, F. S. Englbrecht, Y. Gao, J. Gebhard, M. Gilljohann, J. Götzfried, J. Hartmann, S. Herr, P. Hilz, S. D. Kraft, C. Kreuzer, F. Kroll, F. H. Lindner, J. Metzkes-Ng, T. M. Ostermayr, E. Ridente, **T. F. Rösch**, G. Schilling, H.-P. Schlenvoigt, M. Speicher, D. Taray, M. Würl, K. Zeil, U. Schramm, S. Karsch, K. Parodi, P. R. Bolton, W. Assmann and J. Schreiber. I-BEAT: Ultrasonic method for online measurement of the energy distribution of a single ion bunch. *Scientific Reports*, 9, 6714, 2019.

3. M. Würl, F. S. Englbrecht, S. Lehrack, C. Gianoli, F. H. Lindner, **T. F. Rösch**, D. Haffa, F. Olivari, M. Petasecca, M. LF. Lerch, A. Pogossov, L. T. Tran, W. Assmann, J. Schrieber, A. B. Rosenfeld and K. Parodi. Time-of-flight spectrometry of ultra-short, polyenergetic proton bunches. *Rev. Sci. Instrum.*, 89, 12, 123302, 2018.

4. F. H. Lindner, J. H. Bin, F. Englbrecht, D. Haffa, P. R. Bolton, Y. Gao, J. Hartmann, P. Hilz, C. Kreuzer, T. M. Ostermayr, **T. F. Rösch**, M. Speicher, K. Parodi, P. G. Thirolf and J. Schreiber. A novel approach to electron data background treatment in an online wide-angle spectrometer for laser-accelerated ion and electron bunches. *Rev. Sci. Instrum.*, 89, 1, 013301, 2018.

5. P. Hilz, T. M. Ostermayr, A. Huebl, V. Bagnoud, B. Borm, M. Bussmann, M. Gallei, J. Gebhard, D. Haffa, J. Hartmann, T. Kluge, F. H. Lindner, P. Neumayr,

C.G. Schaefer, U. Schramm, P. G. Thirolf, **T. F. Rösch**, F. Wagner, B. Zielbauer and J. Schreiber. Isolated proton bunch acceleration by a petawatt laser pulse. *Nat Commun*, 9, 423, 2018.

6. F. H. Lindner, D. Haffa, J. Bin, F. Englbrecht, Y. Gao, J. Gebhard, J. Hartmann, P. Hilz, C. Kreuzer, S. Lehrack, T. M. Ostermayr, **T. F. Rösch**, M. Speicher, M. Würl, K. Parodi, J. Schreiber and P. G. Thirolf. Towards swift ion bunch acceleration by high-power laser pulses at the Centre for Advanced Laser Applications (CALA). *Nucl. Instrum. Methods in Phys. Res. B*, 402, 354–357, 2017.

7. C. Greubel, K. Ilicic, **T. F. Rösch**, J. Reindl, C. Siebenwirth, M. Moser, S. Girst, D. WM. Walsh, T. E. Schmid and G. Dollinger, Günther. Low LET proton microbeam to understand high-LET RBE by shaping spatial dose distribution. *Nucl. Instrum. Methods in Phys. Res. B*, 404, 155–161, 2017.

8. Y. Gao, J. Bin, D. Haffa, C. Kreuzer, J. Hartmann, M. Speicher, F. H. Lindner, T. M. Ostermayr, P. Hilz, Peter **T. F. Rösch**, S. Lehrack, F. Englbrecht, S. Seuferling, M. Gilljohann, H. Ding, W. Ma, K. Parodi and J. Schreiber. An automated, 0.5 Hz nano-foil target positioning system for intense laser plasma experiments. *High Power Laser Science and Engineering*, 5, 2017.

9. T.M. Ostermayr, D. Haffa, P. Hilz, V. Pauw, K. Allinger, K.-U. Bamberg, P. Böhl, P. C. Bömer, P. R. Bolton, F. Deutschmann, T. Ditmire, M. E. Donovan, G. Dyer, E. Gaul, J. Gordon, B. M. Hegelich, D. Kiefer, C. Klier, C. Kreuzer, M. Martinez, M. E. McCary, A. R. Meadows, N. Moschüring, **T. Rösch**, H. Ruhl, M. Spinks, C. Wagner and J. Schreiber. Proton acceleration by irradiation of isolated spheres with an intense laser pulse. *Phys. Rev. E*, 94, 3, 033208, 2016.

10. T. Vallentin, M. Moser, S. Eschbaumer, C. Greubel, T. Haase, P. Reichart, **T. F. Rösch** and G. Dollinger. A microbeam slit system for high beam currents. *Nucl. Instrum. Methods in Phys. Res. B*, 348, 43–47, 2015.

Conference Proceedings

1. J. Hartmann, **T. F. Rösch**, F. Balling, M. Berndl, L. Flaig, S. Gerlach, L. Tischendorf, and J. Schreiber. Commissioning of the laser-driven ion acceleration beamline at the Centre for Advanced Laser Applications. In *Laser Acceleration of*

Electrons, Protons, and Ions VI, vol. 11779, 117790N (International Society for Optics and Photonics, 2021).

2. M. Speicher, D. Haffa, M. A. O. Haug, J. Bin, Y. Gao, J. Hartmann, P. Hilz, C. Kreuzer, F. H. Lindner, T. M. Ostermayr, **T. F. Rösch**, R. Yang and J. Schreiber. Integrated double-plasma-mirror targets for contrast enhancement in laser ion acceleration. *Journal of Physics: Conference Series*, 1079, 012002, 2018.

3. **T. F. Rösch**, P. Hilz, J. Bin, F. Englbrecht, Y. Gao, D. Haffa, J. Hartmann, S. Herr, F. H. Lindner, M. Speicher, M. Würl, K. Parodi and J. Schreiber. Considerations on employing a PMQ-doublet for narrow and broad proton energy distributions. *Current Directions in Biomedical Engineering*, 3, 2, 339–342, 2017.

4. F. Englbrecht, F. Balling, **T. F. Rösch**, M. Würl, F. H. Lindner, K. Parodi, and J. Schreiber. Characterization of online high dynamic range imaging for laser-driven ion beam diagnostics using visible light. *Current Directions in Biomedical Engineering*, 3, 2, 343–346, 2017.

Conference Contributions

- **Poster:** Laser-driven ION (LION) acceleration at the centre for advanced laser applications (CALA). *The European Conference on Lasers and Electro-Optics*, Munich (Germany), 2017.

- **Poster:** Considerations on employing a PMQ-doublet for narrow and broad proton energy distributions. *Jahrestagung der Deutschen Gesellschaft für Medizinische Physik*, Dresden (Germany), 2017.

- **Poster:** A feasibility study of zebrafish embryo irradiation with laser accelerated protons. *Laser-Plasma Accelerator Workshop*, Split (Croatia), 2019.

- **Poster:** A feasibility study of zebrafish embryo irradiation with laser accelerated protons. *Jahrestagung der Deutschen Gesellschaft für Medizinische Physik*, Stuttgart (Germany), 2019.

- **Oral:** Laser-Driven Ion Acceleration at the Centre for Advanced Laser Applications. 41^{st} *International Workshop on High-Energy-Density Physics with Intense Ion and Laser Beams*, virtual, 2021.

- **Oral:** Optimization of a permanent magnet quadrupole doublet for laser-accelerated proton bunches at the Centre for Advanced Laser Applications. *SPIE Optics + Optoelectronics*, virtual, 2021.

Bibliography

[1] Gonsalves, A. J. *et al.* Petawatt laser guiding and electron beam acceleration to 8 gev in a laser-heated capillary discharge waveguide. *Physical Review Letters* **122**, 084801 (2019). URL https://link.aps.org/doi/10.1103/PhysRevLett.122.084801.

[2] Higginson, A. *et al.* Near-100 mev protons via a laser-driven transparency-enhanced hybrid acceleration scheme. *Nature communications* **9**, 1–9 (2018). URL https://doi.org/10.1038/s41467-018-03063-9.

[3] Lindner, F. H. *et al.* En-route to the fission–fusion reaction mechanism: a status update on laser-driven heavy ion acceleration. *Plasma Physics and Controlled Fusion* **61**, 055002 (2019). URL https://doi.org/10.1088/1361-6587/ab068d.

[4] Aymar, G. *et al.* Lhara: The laser-hybrid accelerator for radiobiological applications. *Frontiers in Physics* **8**, 432 (2020). URL https://www.frontiersin.org/article/10.3389/fphy.2020.567738.

[5] Bolton, P., Parodi, K. & Schreiber, J. *Applications of laser-driven particle acceleration* (CRC Press, 2018).

[6] Schreiber, J., Bolton, P. R. & Parodi, K. Invited review article:"hands-on" laser-driven ion acceleration: A primer for laser-driven source development and potential applications. *Review of Scientific Instruments* **87**, 071101 (2016). URL https://aip.scitation.org/doi/abs/10.1063/1.4959198.

[7] Ostermayr, T. M. *et al.* Laser-driven x-ray and proton micro-source and application to simultaneous single-shot bi-modal radiographic imaging. *Nature Communications* **11**, 6174 (2020). URL https://doi.org/10.1038/s41467-020-19838-y.

[8] Evans, L. & Bryant, P. LHC machine. *Journal of Instrumentation* **3**, S08001–S08001 (2008). URL https://doi.org/10.1088/1748-0221/3/08/s08001.

[9] Busold, S. *et al.* Towards highest peak intensities for ultra-short MeV-range ion bunches. *Scientific Reports* **5**, 12459 (2015). URL http://www.nature.com/articles/srep12459.

[10] Brack, F.-E. *et al.* Spectral and spatial shaping of laser-driven proton beams using a pulsed high-field magnet beamline. *Scientific reports* **10**, 1–12 (2020). URL https://doi.org/10.1038/s41598-020-65775-7.

[11] Jahn, D. *et al.* First application studies at the laser-driven light beamline: Improving proton beam homogeneity and imaging of a solid target. *Nuclear Instruments and Methods in Physics Research Section A: Accelerators, Spectrometers, Detectors and Associated Equipment* **909**, 173–176 (2018). URL https://www.sciencedirect.com/science/article/pii/S0168900218301803. 3rd European Advanced Accelerator Concepts workshop (EAAC2017).

[12] Margarone, D. *et al.* Elimaia: A laser-driven ion accelerator for multidisciplinary applications. *Quantum Beam Science* **2**, 8 (2018). URL https://www.mdpi.com/2412-382X/2/2/8.

[13] Romano, F. *et al.* The elimed transport and dosimetry beamline for laser-driven ion beams. *Nuclear Instruments and Methods in Physics Research Section A: Accelerators, Spectrometers, Detectors and Associated Equipment* **829**, 153–158 (2016). URL https://www.sciencedirect.com/science/article/pii/S0168900216000929. 2nd European Advanced Accelerator Concepts Workshop - EAAC 2015.

[14] Pommarel, L. *et al.* Spectral and spatial shaping of a laser-produced ion beam for radiation-biology experiments. *Physical Review Accelerators and Beams* **20**, 032801 (2017). URL https://link.aps.org/doi/10.1103/PhysRevAccelBeams.20.032801.

[15] Masood, U. *et al.* A compact solution for ion beam therapy with laser accelerated protons. *Applied Physics B* **117**, 41–52 (2014). URL http://link.springer.com/10.1007/s00340-014-5796-z.

[16] Patel, P. *et al.* Isochoric Heating of Solid-Density Matter with an Ultrafast Proton Beam. *Physical Review Letters* **91**, 125004 (2003). URL http://link.aps.org/doi/10.1103/PhysRevLett.91.125004.

[17] Kar, S. *et al.* Guided post-acceleration of laser-driven ions by a miniature modular structure. *Nature Communications* **7**, 10792 (2016). URL http://www.nature.com/doifinder/10.1038/ncomms10792.

[18] Kar, S. *et al.* Dynamic control of laser driven proton beams by exploiting self-generated, ultrashort electromagnetic pulses. *Physics of Plasmas* **23**, 055711 (2016). URL http://scitation.aip.org/content/aip/journal/pop/23/5/10.1063/1.4948725.

[19] Toncian, T. *et al.* Ultrafast laser-driven microlens to focus and energy-select mega-electron volt protons. *Science* **312**, 410–413 (2006). URL https://www.science.org/doi/10.1126/science.1124412.

[20] van Tilborg, J. *et al.* Active plasma lensing for relativistic laser-plasma-accelerated electron beams. *Physical Review Letters* **115**, 184802 (2015). URL https://link.aps.org/doi/10.1103/PhysRevLett.115.184802.

[21] Burris-Mog, T. *et al.* Laser accelerated protons captured and transported by a pulse power solenoid. *Physical Review Special Topics - Accelerators and Beams* **14**, 121301 (2011). URL http://link.aps.org/doi/10.1103/PhysRevSTAB.14.121301.

[22] Kumar, V. Understanding the focusing of charged particle beams in a solenoid magnetic field. *American Journal of Physics* **77**, 737–741 (2009). URL https://doi.org/10.1119/1.3129242.

[23] Kroll, F. *The study and development of pulsed high-field magnets for application in laser-plasma physics.* Ph.D. thesis, Helmholtz-Zentrum Dresden-Rossendorf (Germany) (2018). URL https://nbn-resolving.org/urn:nbn:de:bsz:d120-qucosa2-322841.

[24] Christofilos, N. Focusing system for ions and electrons. *US Patent* **2** (1950).

[25] Eichner, T. *et al.* Miniature magnetic devices for laser-based, table-top free-electron lasers. *Physical Review Special Topics - Accelerator and Beams* **10**, 082401 (2007). URL https://link.aps.org/doi/10.1103/PhysRevSTAB.10.082401.

[26] Becker, S. *et al.* Characterization and tuning of ultrahigh gradient permanent magnet quadrupoles. *Physical Review Special Topics - Accelerator and Beams* **12**, 102801 (2009). URL http://link.aps.org/doi/10.1103/PhysRevSTAB.12.102801.

[27] Schollmeier, M. *et al.* Controlled transport and focusing of laser-accelerated protons with miniature magnetic devices. *Physical Review Letters* **101**, 055004 (2008). URL http://link.aps.org/doi/10.1103/PhysRevLett.101.055004.

[28] Schillaci, F. *et al.* Errors and optics study of a permanent magnet quadrupole system. *Journal of Instrumentation* **10**, T05001–T05001 (2015). URL http://stacks.iop.org/1748-0221/10/i=05/a=T05001?key=crossref.d264b26a92ab48d5f6cdac0348c09f2c.

[29] Schillaci, F. *et al.* Characterization of the ELIMED Permanent Magnets Quadrupole system prototype with laser-driven proton beams. *Journal of Instrumentation* **11**, T07005–T07005 (2016). URL http://stacks.iop.org/1748-0221/11/i=07/a=T07005?key=crossref.6d22d3e6a1e239a45321a1eac92099a7.

[30] Rösch, T. F. *et al.* Considerations on employing a PMQ-doublet for narrow and broad proton energy distributions. *Current Directions in Biomedical Engineering* **3**, 339–342 (2017). URL http://www.degruyter.com/view/j/cdbme.2017.3.issue-2/cdbme-2017-0069/cdbme-2017-0069.xml.

[31] Rösch, T. F. *A Permanent Magnet Focusing Structure for Laser-Accelerated Ions.* Master's thesis, Ludwig-Maximilians-Universität München (2015).

[32] Cowan, T. E. *et al.* Ultralow emittance, multi-mev proton beams from a laser virtual-cathode plasma accelerator. *Physical Review Letters* **92**, 204801 (2004). URL http://link.aps.org/doi/10.1103/PhysRevLett.92.204801.

[33] Roth, M. *et al.* Laser accelerated ions and electron transport in ultra-intense laser matter interaction. *Laser and Particle Beams* **23**, 97–100 (2005).

[34] Roth, M. *et al.* The generation of high-quality, intense ion beams by ultra-intense lasers. *Plasma Physics and Controlled Fusion* **44**, B99 (2002). URL http://stacks.iop.org/0741-3335/44/i=12B/a=308.

[35] Nürnberg, F. *et al.* Radiochromic film imaging spectroscopy of laser-accelerated proton beams. *Review of Scientific Instruments* **80**, 033301 (2009). URL https://doi.org/10.1063/1.3086424. https://doi.org/10.1063/1.3086424.

[36] Wu, M. J. *et al.* Emittance measurement along transport beam line for laser driven protons. *Physical Review Accelerators and Beams* **23**, 031302 (2020). URL https://link.aps.org/doi/10.1103/PhysRevAccelBeams.23.031302.

[37] McDonald, K. & Russell, D. Methods of emittance measurement. In *Frontiers of particle beams; observation, diagnosis and correction*, 122–132 (Springer, 1989).

[38] Borghesi, M. *et al.* Multi-MeV Proton Source Investigations in Ultraintense Laser-Foil Interactions. *Physical Review Letters* **92**, 055003 (2004). URL `http://link.aps.org/doi/10.1103/PhysRevLett.92.055003`.

[39] Woodward, P. M. A method of calculating the field over a plane aperture required to produce a given polar diagram. *Journal of the Institution of Electrical Engineers-Part IIIA: Radiolocation* **93**, 1554–1558 (1947).

[40] Lawson, J. D. Lasers and accelerators. *IEEE Transactions on Nuclear Science* **26**, 4217–4219 (1979). URL `https://ieeexplore.ieee.org/document/4330749`.

[41] Palmer, R. B. A laser driven grating linac. *Particle Accelerators* **11**, 81–90 (1980).

[42] Breuer, J. *Dielectric laser acceleration of non-relativistic electrons at a photonic structure*. Ph.D. thesis, Ludwig-Maximilians-Universität München (2013). URL `http://nbn-resolving.de/urn:nbn:de:bvb:19-161479`.

[43] Breuer, J. & Hommelhoff, P. Laser-Based Acceleration of Nonrelativistic Electrons at a Dielectric Structure. *Physical Review Letters* **111**, 134803 (2013). URL `https://link.aps.org/doi/10.1103/PhysRevLett.111.134803`.

[44] Breuer, J., Graf, R., Apolonski, A. & Hommelhoff, P. Dielectric laser acceleration of nonrelativistic electrons at a single fused silica grating structure: Experimental part. *Physical Review Special Topics - Accelerators and Beams* **17**, 021301 (2014). URL `https://link.aps.org/doi/10.1103/PhysRevSTAB.17.021301`.

[45] Morrison, J. T. *et al.* MeV proton acceleration at kHz repetition rate from ultra-intense laser liquid interaction. *New Journal of Physics* **20**, 022001 (2018). URL `https://doi.org/10.1088/1367-2630/aaa8d1`.

[46] Hilz, P. *et al.* Isolated proton bunch acceleration by a petawatt laser pulse. *Nature communications* **9**, 1–9 (2018). URL `https://doi.org/10.1038/s41467-017-02663-1`.

[47] Hegelich, M. *et al.* Mev ion jets from short-pulse-laser interaction with thin foils. *Physical Review Letters* **89**, 085002 (2002). URL `http://link.aps.org/doi/10.1103/PhysRevLett.89.085002`.

[48] McKenna, P. *et al.* Characterization of proton and heavier ion acceleration in ultrahigh-intensity laser interactions with heated target foils. *Physical Review*

E **70**, 036405 (2004). URL https://link.aps.org/doi/10.1103/PhysRevE.70.036405.

[49] Macchi, A., Borghesi, M. & Passoni, M. Ion acceleration by superintense laser-plasma interaction. *Reviews of Modern Physics* **85**, 751–793 (2013). URL https://link.aps.org/doi/10.1103/RevModPhys.85.751.

[50] Daido, H., Nishiuchi, M. & Pirozhkov, A. S. Review of laser-driven ion sources and their applications. *Reports on Progress in Physics* **75**, 056401 (2012). URL http://stacks.iop.org/0034-4885/75/i=5/a=056401.

[51] Strickland, D. & Mourou, G. Compression of amplified chirped optical pulses. *Optics communications* **55**, 447–449 (1985). URL https://www.sciencedirect.com/science/article/pii/0030401885901518.

[52] Mainfray, G. & Manus, G. Multiphoton ionization of atoms. *Reports on Progress in Physics* **54**, 1333–1372 (1991). URL https://doi.org/10.1088/0034-4885/54/10/002.

[53] Keldysh, L. *et al.* Ionization in the field of a strong electromagnetic wave. *Soviet Physics JETP* **20**, 1307–1314 (1965). URL https://inspirehep.net/literature/1793133.

[54] Chin, S. L. *FROM MULTIPHOTON TO TUNNEL IONIZATION*, 249–271 (World Scientific, 2004). URL https://www.worldscientific.com/doi/abs/10.1142/9789812796585_0003.

[55] Delone, N. B. & Krainov, V. P. Tunneling and barrier-suppression ionization of atoms and ions in a laser radiation field. *Physics-Uspekhi* **41**, 469–485 (1998). URL https://doi.org/10.1070/pu1998v041n05abeh000393.

[56] Chen, F. F. *Introduction to plasma physics and controlled fusion*, chap. 1, 3–11 (Springer, 2016), 3 edn.

[57] Jackson, J. D. *Classical electrodynamics* (Wiley, New York, 1999), 3. edn.

[58] Gibbon, P. *Short pulse laser interactions with matter: an introduction* (World Scientific, 2005), 2 edn.

[59] Brunel, F. Not-so-resonant, resonant absorption. *Physical Review Letters* **59**, 52–55 (1987). URL https://link.aps.org/doi/10.1103/PhysRevLett.59.52.

[60] Kruer, W. L. & Estabrook, K. J×B heating by very intense laser light. *Physics of Fluids* **28**, 430–432 (1985). URL https://aip.scitation.org/doi/abs/10.1063/1.865171.

[61] Mora, P. Plasma expansion into a vacuum. *Physical Review Letters* **90**, 185002 (2003). URL https://link.aps.org/doi/10.1103/PhysRevLett.90.185002.

[62] Wilks, S. C., Kruer, W. L., Tabak, M. & Langdon, A. B. Absorption of ultra-intense laser pulses. *Physical Review Letters* **69**, 1383–1386 (1992). URL https://link.aps.org/doi/10.1103/PhysRevLett.69.1383.

[63] Schreiber, J. *et al.* Analytical model for ion acceleration by high-intensity laser pulses. *Physical Review Letters* **97**, 045005 (2006). URL https://link.aps.org/doi/10.1103/PhysRevLett.97.045005.

[64] Wilks, S. C. *et al.* Energetic proton generation in ultra-intense laser–solid interactions. *Physics of Plasmas* **8**, 542–549 (2001). URL https://doi.org/10.1063/1.1333697.

[65] Hatchett, S. P. *et al.* Electron, photon, and ion beams from the relativistic interaction of petawatt laser pulses with solid targets. *Physics of Plasmas* **7**, 2076–2082 (2000). URL https://doi.org/10.1063/1.874030.

[66] Esirkepov, T., Borghesi, M., Bulanov, S. V., Mourou, G. & Tajima, T. Highly efficient relativistic-ion generation in the laser-piston regime. *Physical Review Letters* **92**, 175003 (2004). URL https://link.aps.org/doi/10.1103/PhysRevLett.92.175003.

[67] Henig, A. *et al.* Radiation-pressure acceleration of ion beams driven by circularly polarized laser pulses. *Physical Review Letters* **103**, 245003 (2009). URL https://link.aps.org/doi/10.1103/PhysRevLett.103.245003.

[68] Yin, L., Albright, B. J., Hegelich, B. M. & Fernandez, J. C. Gev laser ion acceleration from ultrathin targets: The laser break-out afterburner. *Laser and Particle Beams* **24**, 291–298 (2006). URL https://doi.org/10.1017/S0263034606060459.

[69] Silva, L. O. *et al.* Proton shock acceleration in laser-plasma interactions. *Physical Review Letters* **92**, 015002 (2004). URL https://link.aps.org/doi/10.1103/PhysRevLett.92.015002.

[70] Krushelnick, K. *et al.* Multi-mev ion production from high-intensity laser interactions with underdense plasmas. *Physical Review Letters* **83**, 737–740 (1999). URL `https://link.aps.org/doi/10.1103/PhysRevLett.83.737`.

[71] Bulanov, S. V., Dylov, D. V., Esirkepov, T. Z., Kamenets, F. F. & Sokolov, D. V. Ion acceleration in a dipole vortex in a laser plasma corona. *Plasma physics reports* **31**, 369–381 (2005). URL `https://doi.org/10.1134/1.1925787`.

[72] Nakamura, T., Bulanov, S. V., Esirkepov, T. Z. & Kando, M. High-energy ions from near-critical density plasmas via magnetic vortex acceleration. *Physical Review Letters* **105**, 135002 (2010). URL `https://link.aps.org/doi/10.1103/PhysRevLett.105.135002`.

[73] Snavely, R. A. *et al.* Intense high-energy proton beams from petawatt-laser irradiation of solids. *Physical Review Letters* **85**, 2945–2948 (2000). URL `https://link.aps.org/doi/10.1103/PhysRevLett.85.2945`.

[74] Allen, M. *et al.* Direct experimental evidence of back-surface ion acceleration from laser-irradiated gold foils. *Physical Review Letters* **93**, 265004 (2004). URL `https://link.aps.org/doi/10.1103/PhysRevLett.93.265004`.

[75] Mackinnon, A. J. *et al.* Effect of plasma scale length on multi-mev proton production by intense laser pulses. *Physical Review Letters* **86**, 1769–1772 (2001). URL `http://link.aps.org/doi/10.1103/PhysRevLett.86.1769`.

[76] Romagnani, L. *et al.* Dynamics of electric fields driving the laser acceleration of multi-mev protons. *Physical Review Letters* **95**, 195001 (2005). URL `http://link.aps.org/doi/10.1103/PhysRevLett.95.195001`.

[77] Fuchs, J. *et al.* Laser-driven proton scaling laws and new paths towards energy increase. *Nature Physics* **2**, 48–54 (2006). URL `http://www.nature.com/doifinder/10.1038/nphys199`.

[78] Kaluza, M. *et al.* Influence of the Laser Prepulse on Proton Acceleration in Thin-Foil Experiments. *Physical Review Letters* **93**, 045003 (2004). URL `http://link.aps.org/doi/10.1103/PhysRevLett.93.045003`.

[79] Poole, P. L. *et al.* Laser-driven ion acceleration via target normal sheath acceleration in the relativistic transparency regime. *New Journal of Physics* **20**, 013019 (2018). URL `https://doi.org/10.1088/1367-2630/aa9d47`.

[80] Schwoerer, H. *et al.* Laser-plasma acceleration of quasi-monoenergetic protons from microstructured targets. *Nature* **439**, 445–448 (2006). URL http://www.nature.com/doifinder/10.1038/nature04492.

[81] Fuchs, J. *et al.* Spatial uniformity of laser-accelerated ultrahigh-current mev electron propagation in metals and insulators. *Physical Review Letters* **91**, 255002 (2003). URL http://link.aps.org/doi/10.1103/PhysRevLett.91.255002.

[82] Bin, J. H. *et al.* On the small divergence of laser-driven ion beams from nanometer thick foils. *Physics of Plasmas* **20**, 073113 (2013). URL https://doi.org/10.1063/1.4816031. https://doi.org/10.1063/1.4816031.

[83] Ostermayr, T. M. *et al.* Proton acceleration by irradiation of isolated spheres with an intense laser pulse. *Physical Review E* **94**, 033208 (2016). URL https://link.aps.org/doi/10.1103/PhysRevE.94.033208.

[84] Carroll, D. C. *et al.* Active manipulation of the spatial energy distribution of laser-accelerated proton beams. *Physical Review E* **76**, 065401 (2007). URL http://link.aps.org/doi/10.1103/PhysRevE.76.065401.

[85] Brambrink, E. *et al.* Transverse characteristics of short-pulse laser-produced ion beams: A study of the acceleration dynamics. *Physical Review Letters* **96**, 154801 (2006). URL https://link.aps.org/doi/10.1103/PhysRevLett.96.154801.

[86] Liu, H. *et al.* Characterization of energetic protons generated in the shenguang-ii up petawatt laser interactions with foil targets. *Laser and Particle Beams* **2021**, 7205383 (2021). URL https://doi.org/10.1155/2021/7205383.

[87] Schreiber, J. *et al.* Source-size measurements and charge distributions of ions accelerated from thin foils irradiated by high-intensity laser pulses. *Applied Physics B* **79**, 1041–1045 (2004). URL http://link.springer.com/10.1007/s00340-004-1665-5.

[88] Sommer, P. *et al.* Laser-ablation-based ion source characterization and manipulation for laser-driven ion acceleration. *Plasma Physics and Controlled Fusion* **60**, 054002 (2018). URL https://doi.org/10.1088/1361-6587/aab21e.

[89] Palaniyappan, S. *et al.* Dynamics of relativistic transparency and optical shuttering in expanding overdense plasmas. *Nature Physics* **8**, 763–769 (2012). URL https://doi.org/10.1038/nphys2390.

[90] Macchi, A., Cattani, F., Liseykina, T. V. & Cornolti, F. Laser acceleration of ion bunches at the front surface of overdense plasmas. *Physical Review Letters* **94**, 165003 (2005). URL https://link.aps.org/doi/10.1103/PhysRevLett.94.165003.

[91] Bin, J. H. *et al.* Dynamics of laser-driven proton acceleration exhibited by measured laser absorptivity and reflectivity. *Scientific Reports* **7**, 43548 (2017). URL http://www.nature.com/articles/srep43548.

[92] Wille, K. *Physik der Teilchenbeschleuniger und Synchrotronstrahlungsquellen: Ein Einführung*, chap. 3 (B.G.Teubner, Stuttgart, 1996), 2. revised and extended edn.

[93] Hinterberger, F. *Physik der Teilchenbeschleuniger und Ionenoptik*, chap. 4 (Springer, Berlin Heidelberg, 2008), 2. edn.

[94] Wiedemann, H. *Particle accelerator physics* (Springer, 2015), fourth edn.

[95] Hartmann, J. *et al.* Commissioning of the laser-driven ion acceleration beamline at the centre for advanced laser applications. In *Laser Acceleration of Electrons, Protons, and Ions VI*, vol. 11779, 117790N (International Society for Optics and Photonics, 2021). URL https://doi.org/10.1117/12.2592407.

[96] Gao, Y. *et al.* An automated, 0.5 hz nano-foil target positioning system for intense laser plasma experiments. *High Power Laser Science and Engineering* **5**, e12 (2017). URL https://doi.org/10.1017/hpl.2017.10.

[97] Tischendorf, L. *Transport of Laser-Accelerated Ions with Permanent Magnet Quadrupole Lenses - Effects of Field- and Alignmenterrors on the Focus Shape.* Master's thesis, Martin-Luther Universität Halle-Wittenberg/Ludwig-Maximilians-Universität München (2020).

[98] Halbach, K. Design of permanent multipole magnets with oriented rare earth cobalt material. *Nuclear Instruments and Methods* **169**, 1 – 10 (1980). URL http://www.sciencedirect.com/science/article/pii/0029554X80900944.

[99] Ziegler, J. F., Ziegler, M. & Biersack, J. Srim - the stopping and range of ions in matter. http://www.srim.org. Accessed: 2021-12-22.

[100] Ziegler, J. F., Ziegler, M. & Biersack, J. Srim – the stopping and range of ions in matter (2010). *Nuclear Instruments and Methods in Physics Research Section B: Beam*

Interactions with Materials and Atoms **268**, 1818–1823 (2010). URL https://www.sciencedirect.com/science/article/pii/S0168583X10001862. 19th International Conference on Ion Beam Analysis.

[101] Battistoni, G. *et al.* The fluka code: description and benchmarking. *AIP Conference Proceedings* **896**, 31–49 (2007). URL https://aip.scitation.org/doi/abs/10.1063/1.2720455.

[102] Ferrari, A. *et al.* Fluka: a multi-particle transport code. Tech. Rep., Citeseer (2005). URL https://doi.org/10.2172/877507.

[103] Cho, M. *et al.* Measurements of x-ray imaging performance of granular phosphors with direct-coupled cmos sensors. *Nuclear Science, IEEE Transactions on* **55**, 1338 – 1343 (2008). URL https://doi.org/10.1109/TNS.2007.913939.

[104] Butson, M. J., Peter, K., Cheung, T. & Metcalfe, P. Radiochromic film for medical radiation dosimetry. *Materials Science and Engineering: R: Reports* **41**, 61–120 (2003). URL https://doi.org/10.1016/S0927-796X(03)00034-2.

[105] Gafchromic ebt-3 specifications. http://www.gafchromic.com/documents/EBT3_Specifications.pdf. Accessed: 2022-02-01.

[106] Walcher, D. *Absolute Calibration of Radiochromic Films.* Bachelor's thesis, Ludwig-Maximilians-Universität München (2021).

[107] Reinhardt, S., Hillbrand, M., Wilkens, J., Assmann, W. & Parodi, K. SU-E-T-52: Evaluation of EBT2 and EBT3 Films for Dosimetry in Laser-Driven Ion Accelerators. *Medical Physics* **40**, 215–215 (2013). URL http://doi.wiley.com/10.1118/1.4814487.

[108] Miyahara, J., Takahashi, K., Amemiya, Y., Kamiya, N. & Satow, Y. A new type of x-ray area detector utilizing laser stimulated luminescence. *Nuclear Instruments and Methods in Physics Research Section A: Accelerators, Spectrometers, Detectors and Associated Equipment* **246**, 572–578 (1986). URL https://doi.org/10.1016/0168-9002%2886%2990156-7.

[109] Reinhardt, S. *Detection of laser-accelerated protons.* Ph.D. thesis, Ludwig-Maximilians-Universität München (2012). URL https://edoc.ub.uni-muenchen.de/15562/1/Reinhardt_Sabine.pdf.

[110] Lindner, F. H. *et al.* A novel approach to electron data background treatment in an online wide-angle spectrometer for laser-accelerated ion and electron bunches. *Review of Scientific Instruments* **89**, 013301 (2018). URL https://doi.org/10.1063/1.5001990.

[111] Bin, J. *et al.* A laser-driven nanosecond proton source for radiobiological studies. *Applied Physics Letters* **101**, 243701 (2012). URL http://scitation.aip.org/content/aip/journal/apl/101/24/10.1063/1.4769372.

[112] Roth, M. *et al.* Laser accelerated heavy particles – tailoring of ion beams on a nano-scale. *Optics Communications* **264**, 519–524 (2006). URL https://www.sciencedirect.com/science/article/pii/S003040180600527X.

[113] Göde, S. *et al.* Relativistic electron streaming instabilities modulate proton beams accelerated in laser-plasma interactions. *Physical Review Letters* **118**, 194801 (2017). URL https://link.aps.org/doi/10.1103/PhysRevLett.118.194801.

[114] Sgattoni, A., Sinigardi, S., Fedeli, L., Pegoraro, F. & Macchi, A. Laser-driven rayleigh-taylor instability: Plasmonic effects and three-dimensional structures. *Physical Review E* **91**, 013106 (2015). URL https://link.aps.org/doi/10.1103/PhysRevE.91.013106.

[115] Palmer, C. A. J. *et al.* Rayleigh-taylor instability of an ultrathin foil accelerated by the radiation pressure of an intense laser. *Physical Review Letters* **108**, 225002 (2012). URL https://link.aps.org/doi/10.1103/PhysRevLett.108.225002.

[116] Pegoraro, F. & Bulanov, S. V. Photon bubbles and ion acceleration in a plasma dominated by the radiation pressure of an electromagnetic pulse. *Physical Review Letters* **99**, 065002 (2007). URL https://link.aps.org/doi/10.1103/PhysRevLett.99.065002.

[117] Floettmann, K. Some basic features of the beam emittance. *Physical Review Special Topics - Accelerator and Beams* **6**, 034202 (2003). URL https://link.aps.org/doi/10.1103/PhysRevSTAB.6.034202.

[118] Rösch, T. F. *et al.* A feasibility study of zebrafish embryo irradiation with laser-accelerated protons. *Review of Scientific Instruments* **91**, 063303 (2020). URL https://doi.org/10.1063/5.0008512.

Acknowledgments

Zum Abschluss dieser Arbeit ist es mir wichtig einigen Menschen zu danken, die maßgeblich zu deren Gelingen beigetragen haben und mich während der letzten Jahre auf unterschiedlichste Weise sehr unterstützt haben.

Der erste Dank gebührt **Jörg Schreiber**. Ich konnte mich immer auf seinen Rückhalt verlassen und bin sehr dankbar für die wöchentlichen Meetings mit hilfreichen Diskussionen und unzähligen motivierenden Worte die mich insbesondere durch das letzte Jahr getragen haben. Ich danke ihm auch sehr für das große in mich gesetzte Vertrauen und für die große Förderung, indem mir die Teilnahmen an Experimenten, Workshops, Konferenzen und besonders der CERN Accelerator School ermöglicht wurden. Und nicht zuletzt vielen Dank für das Aufbauen und Erhalten der besten Arbeitsgruppe die man sich wünschen kann. Die vielen gemeinsamen Aktivitäten waren Grundstein für einen starken sozialen Zusammenhalt ohne den für viele Herausforderungen beim Aufbau von CALA die Ausdauer gefehlt hätte.

Ich möchte mich ausgesprochen bei der Studienstiftung des deutschen Volkes bedanken, dass sie mich einen Teil der Promotionszeit gefördert hat. Außerdem bedanke ich mich bei **Ulrich Schramm**, dass er sich bereit erklärt hat, Zweitgutachter dieser Arbeit zu sein sowie bei **Bernhard Mayer** und **Armin Scrinzi**, die sich als Prüfer zur Verfügung gestellt haben.

Aus der AG Schreiber möchte ich mich zunächst bei denen bedanken, die Experimente in LION überhaupt erst möglich gemacht haben, **Jens Hartmann**, **Leonard (Lenny) Doyle** und **Daniel Haffa**. Auf ihren Schultern lastete die Hauptarbeit während des Aufbaus von CALA LION. Ich danke ihnen und auch den "Neuen" im CALA LION Team **Felix Balling**, **Sonja Gerlach** und **Alexander Praßelsperger** sehr für die tatkräftige Unterstützung und Hilfe bei zahlreichen spannenden, anstrengenden, frustrierenden und witzigen Strahlzeiten. Wir hatten viel Spaß!

Ein außerordenltich großer Dank geht auch an alle weiteren aktuellen und früheren Mitglieder der AG Schreiber. Allen voran an meinen jahrelanger Büronachbar **Johannes Gebhard**, der sich manche Klage anhören musste, aber auch an **Martin Speicher**, der immer ein interessiertes Ohr für Fragen und Ideen hatte und auf dessen Hilfe ich mich bei Konstruktionsaufgaben immer verlassen konnte. The "old" ones **Jianhui Bin**, **Tobias**

Ostermayer, **Christian Kreuzer** and **Ying Gao**, I thank for the countless hours shared during LEX beamtimes and all I could learn from you about both experiments and laser plasma physics. **Peter Hilz** danke ich dafür, dass er mich dem Thema Quadrupole nähergebracht hat und stets eine kreative Idee zur Diskussion parat hatte. A warm and special thank you goes to **Paul Bolton** for being an inspiring source of wisdom and fun in our group for many years.

Ich möchte mich auch bei allen Studentinnen und Studenten bedanken mit denen ich die Freude hatte gemeinsam an dem Thema Quadrupole zu arbeiten und durch die ich immer auch etwas neues dazugelernt habe, **Luisa Tischendorf, Toan Ngoc Nguyen, Youssef Mabrouk, Derya Taray** und **Alexis Laugerette**. Gleiches gilt auch für **Jannik Esslinger, Adrian Dorfschmidt** und **Lotta Flaig**, mit denen ich auf anderen Themengebieten arbeiten durfte. David Walcher danke ich dafür, dass ich seine Daten in meine Arbeit aufnehmen durfte.

Finally, I want to thank all others that crossed my path in this group that I could not mention individually in this place. I am deeply greatful for all the shared work, discussions and fun. I will treasure these moments forever. It was a wonderful time and we had really a lot of fun.

Wichtige Diskussionspartner in allen Fragen in CALA war auch immer die HF Gruppe um **Peter Thirolf**. Ich möchte ihm und seiner Gruppe danken für die schöne und bereichernde Zusammenarbeit, namentlich **Erin Grace Fitzpatrick**, **Laura Geulig** und insbesondere **Florian Lindner**, auch für die langen Jahre des gemeinsamen Wegs am Lehrstuhl.

Ein großer Dank geht an **Stefan Karsch** und seine gesamte ETTF Arbeitsgruppe für die gemeinsame Arbeit in CALA und am ATLAS. Besonders möchte ich **Gregor Schilling** und **Moritz Foerster** für die jederzeit verfügbare Hilfe bei Problembewältigungen danke, aber auch dafür, dass ich viel von ihnen lernen durfte. Außderdem bedanke ich mich bei **Max Gilljohann, Andreas Döpp, Katinka von Grafenstein, Florian Haberstroh, Enes Travac** und **Nils Weiße** für die angenehme und unkomplizierte Zusammenarbeit und spannenden Diskussionen.

Kein Experiment in CALA wäre möglich ohne das Team von Menschen, die den täglichen Betrieb sicherstellen und mich in allen technischen Belangen unterstützt haben. Ich danke **Hans-Friedrich Wirth** und **Florian Saran** dafür, dass sie immer ein Auge darauf haben, dass wir alles haben, was wir für unsere Labore brauchen. Ich möchte mich auch sehr bei **Jerzy Szerypo** für das Herstellen der Targetfolien bedanken, die so wichtig für alle Experimente dieser Arbeit waren. Ein ganz besonders großer Dank

geht an **Nik Gjotev** und **Oliver Gosau**, die sich in allen technischen Belangen bestens auskennen und für jedes Problem eine Lösung wissen. Nicht zuletzt auch ein großer Dank auch an **Rolf Oehm und sein Team** in der mechanischen Werkstatt unseres Hauses. Trotz widriger Umstände und viel Arbeit findet man dort immer Rat und Hilfe und sie versuchen alles Menschenmögliche um einem so schnell es geht die Anliegen zu erfüllen.

Für die Unterstützung während der Charakterisierung der Quadrupole am Tandem van de Graaff Beschleuniger des Maier-Leibnitz-Laboratoriums möchte ich mich bei **Ludwig Beck, Michael Pelzer** und **Michael Wiesheu** bedanken.

Des weiteren möchte ich mich bei **Katia Parodi** für die Unterstützung und Zusammenarbeit auf Lehrstuhlebene bedanken. Danke auch an **Andrea Leinthaler**, **Felix Rauscher** und **Romy Knab** für die ganze administrative Arbeit die den Lehrstuhl am Laufen und Leben hält. Ich danke auch einigen besonderen Mitgliedern des LS Parodi, angefangen mit **Franz Englbrecht** und **Matthias Würl**, mit denen ich bei zahlreichen Experimenten eine bereichernde Zusammenarbeit erleben durfte. Ihnen und **Juliana Martins**, **Sebastian Lehrack**, **Silvia Liprandi** und **Tim Fitzpatrick** danke ich auch für viele Stunden freundschaftlichen Austauschs und gemeinsamen Gestalten des Lehrstuhllebens. Außerdem möchte ich mich auch bei **Jona Bortfeld** und **Neeraj Kurichiyanil** bedanken, die immer höchst kompetente Diskussionspartner waren, wenn es um das Thema Quadrupole ging.

Zu guter Letzt geht ein herausragendes Dankeschön an meine Eltern, meinen Bruder und meine Freunde (insbesondere Manuel Kraft und Philipp Gregor für das Gegenlesen der Arbeit), die mich in den vergangenen Jahren stets motiviert haben und viel Verständnis und Geduld für die Sorgen und Ängste eines Doktoranden aufgebracht haben. Danke, dass Ihr da seid.